Gold nanocluster modulation of organelles and cellular stress responses in malignant and non-malignant human astrocytes

Evan Rizzel Gran

Department of Pharmacology & Therapeutics
Faculty of Medicine
McGill University
Montreal, QC

December 2020

A thesis submitted to McGill University
in partial fulfillment of the requirements of
the degree of Master of Science (MSc).

Dedicated to my loving family for always believing in my potential
and helping me accomplish more than I could ever imagine

Table of contents

Acknowledgements

Heartfelt thank you for Dr. Dusica Maysinger. I am very grateful to be mentored by such an insightful and motivating individual. I have learned and matured so much over the years, and I cannot thank her enough for her impact on my scientific and personal growth. She has led by example, showing passion and unbound curiosity for scientific research. Immense gratitude for welcoming me into the Nanofamily and introducing me to intelligent, inspiring, and kindhearted scientists, that I am proud to have met.

I would like to extend my gratitude to my thesis advisor, Dr. Anne McKinney, and my committee members, Dr. Ashok Kakkar and Dr. Simon Rousseau, for lending their expertise.

Special thanks to the ever-growing Nanofamily, especially Issan Zhang, Jingwen Meng, Jussânia Gnoatto, Shiraj Diwadi, Qiaochu Zhang, and Alex Moquin. I am thankful for their support, encouragement, and guidance throughout my study at the lab. I am grateful for having the opportunity to collaborate with Dr. Ursula Stochaj and her students from the Physiology Department, and Dr. Kakkar and his students from the Chemistry Department. I would also like to thank Dr. Jack Antel and Manon Blain from the Neuroimmunology lab at the Montreal Neurological Institute.

Thank you to the Pharmacology & Therapeutics administration for their patience and assistance: Tina Tremblay, Anna Cuccovia, and Nadee Buddhiwickrama.

I also wish to thank the Give & Grow Foundation for my scholarship award.

These studies were supported by the Canadian Institute for Health Research, Natural Sciences and Engineering Research, and the Department of Pharmacology and Therapeutics at McGill University.

Abstract

Gold nanoclusters (AuNCs) are emerging tools for biomedical applications, as they are a unique type of gold nanostructure characterized at the atomic level. Whereas gold nanoparticles typically range between 5 to 100 nm, AuNCs are composed of only a few to a hundred gold atoms, measuring less than 5 nm. Their physicochemical properties depend on the accessibility of gold atoms and the composition of surface ligands. AuNCs can mimic redox-regulating enzymes and could provide alternative or complementary diagnostic and therapeutic approaches in oncology. As modulators of reactive oxygen species in biological systems, they show potential as treatment for diseases associated with oxidative stress, such as cancer. Tumors in the central nervous system are among the most intractable cancers. The most common yet deadliest form of brain cancer, glioblastoma multiforme, shows altered redox status, in comparison to healthy astrocytes. AuNCs may provide a new therapeutic approach to GBM treatment as modulators of reactive oxygen species in glioblastoma cells and astrocytes in the tumor microenvironment.

In the present studies, organellar reorganization and molecular mechanisms underlying gold nanocluster exposure in human glioblastoma cells and primary astrocytes were investigated. We showed that GBM adaptation to gold nanocluster treatment includes TFEB-driven lysosomal biogenesis and enhanced lysosomal degradative capacity. In human primary astrocytes, gold nanoclusters impacted mitochondrial abundance and morphology, and subtly affected lipid droplet number and distribution. Levels of lipid peroxidation were also modulated by AuNCs in human primary astrocytes under mild oxidative stress. Larger-sized AuNCs consistently exhibited cytoprotective properties, stimulating nuclear translocation and activation of key redox-responsive transcription factors. However, damage caused by severe oxidative stress could not be counteracted by AuNCs.

Collectively, these findings contribute to the current knowledge of the effects of gold nanoclusters of varying sizes (Au_{10}, Au_{15}, Au_{18}, Au_{25}) and surface ligands (glutathione, polyethylene glycol, N-acetyl cysteine) in human cells, and provide valuable translational data for their use in neuroprotection and neuroinflammation.

Résumé

Les nanoagrégats d'or sont des outils biomédicaux émergents, en raison de la précision de leurs préparations au niveau atomique. Alors que la taille des nanoparticules d'or varie généralement entre 5 et 100 nm, les nanoagrégats d'or sont composées seulement d'une dizaine à quelques centaines d'atomes d'or et mesurent moins de 5 nm. Leurs propriétés physico-chimiques dépendent de l'accessibilité des atomes d'or et de leur fonctionnalisation. Les nanoagrégats d'or peuvent imiter les enzymes naturelles catalysant les réactions d'oxydoréduction. En tant que modulateurs des espèces réactives de l'oxygène dans les systèmes biologiques, ils présentent une alternative prometteuse pour le traitement de maladies associées au stress oxydatif, comme le cancer. Les tumeurs du système nerveux central sont parmi les cancers les plus difficiles à traiter. Le glioblastome multiforme, le cancer du cerveau le plus fréquent mais aussi le plus mortel, présente un statut oxydatif modifié par rapport aux astrocytes sains. Les nanoagrégats d'or peuvent démontrer des effets thérapeutiques en tant que modulateurs d'espèces réactives de l'oxygène dans les cellules de glioblastome et les astrocytes du micro-environnement tumoral.

Dans cette étude, la réorganisation au niveau des organites et les mécanismes moléculaires sous-jacents à l'exposition aux nanoagrégats d'or ont été étudiés dans les cellules de glioblastome et les astrocytes primaires humains. Nous avons démontré que l'adaptation du glioblastome au traitement de nanoagrégats d'or comprend la biogenèse des lysosomes actionnée par le facteur de transcription EB (TFEB), et une capacité de dégradation lysosomale améliorée. Dans les astrocytes primaires humains, les nanoagrégats d'or ont impacté l'abondance et la morphologie des mitochondries, en plus de subtilement affecter le nombre et la distribution des gouttelettes lipidiques. Les niveaux de peroxydation des lipides ont également été modulés par les nanoagrégats d'or dans les astrocytes primaires humains soumis à un stress oxydatif modéré. Les nanoagrégats d'or de plus grande taille présentent des propriétés cytoprotectrices, stimulant la translocation nucléaire et l'activation de facteurs de transcription sensibles à l'oxydoréduction. Cependant, les dommages causés par un stress oxydatif sévère n'ont pu être contrés par les nanoagrégats d'or.

Collectivement, ces résultats contribuent aux connaissances actuelles sur les effets des nanoagrégats d'or de différentes tailles (Au_{10}, Au_{15}, Au_{18}, Au_{25}) et fonctionnalisation (glutathion, polyéthylène glycol, N-acétylcystéine) dans les cellules humaines, et fournissent des données translationnelles pour leur application en neuroprotection et neuroinflammation.

List of figures and tables

Chapter 1. Literature review

Chapter 2. Gold nanoclusters elicit homeostatic perturbations in glioblastoma cells and adaptive changes of lysosomes

List of abbreviations

4-HNE	4-hydroxynonenal
ARE	Antioxidant Response Element
AU	Arbitrary units
AUC	Area under the curve
BEV	Bevacizumab
BBB	Blood brain barrier
CNS	Central nervous system
CQ	Chloroquine
CT	Computerized tomography
CLEAR	Coordinated Lysosomal Expression and Regulation
CMC	Critical micelle concentration
Cyt, C	Cytoplasm
DFT	Density functional theory
DMEM	Dulbecco's modified Eagle Medium
EBSS	Earle's Balanced Salt Solution
ESI	Electrospray ionization
EPR	Enhanced permeability and retention
EGFR	Epidermal growth factor receptor
FBS	Fetal bovine serum
F-actin	Filamentous actin
G3BP1	G3BP Stress Granule Assembly Factor 1
GBM	Glioblastoma multiforme
GSH, SG	Glutathione
AuNC	Gold nanocluster
AuNP	Gold nanoparticle
HSP	Heat shock protein
HMGB1	High mobility group box 1
IL	Interleukin
Keap-1	Kelch-like erythroid cell-derived protein with CNC homology-associated protein 1
BSO	L-buthionine sulfoximine
LDs	Lipid droplets
LPS	Lipopolysaccharide
LAMP-1	Lysosome-associated membrane protein 1
LAMP-2	Lysosome-associated membrane protein 2

mTORC1	Mechanistic target of rapamycin complex 1
MenD	Menadione
MITF	Microphthalmia-associated transcription factor
NAC	N-Acetyl cysteine
Nrf2	Nuclear factor erythroid 2-related factor 2
Nuc, N	Nucleus
MGMT	O^6-methylguanine methyltransferase
OA	Oleic acid
PFA	Paraformaldehyde
P/S	Penicillin-Streptomycin
PBS	Phosphate-buffered saline
PLIN	Perilipin
PGLA	Poly(lactic-co-glycolic acid)
PLC	Polycaprolactone
PDL	Poly-D-lysine
PEG	Polyethylene glycol
PLA	Polylactic acid
Akt	Protein kinase B
ROS	Reactive oxygen species
RAGE	Receptor for advanced glycation end-products
STAT3	Signal transducer and activator of transcription 3
SD	Standard deviation
SEM	Standard error of the mean
TMZ	Temozolomide
TLR	Toll-like receptor
TFE3	Transcription factor E3
TFEB	Transcription factor EB
TFEC	Transcription factor EC
TGF-β	Transforming growth factor β
TNF-α	Tumor necrosis factor- α
VEGF	Vascular endothelial growth factor

Contribution of authors

This thesis is written in a manuscript-based format in accordance with the Guidelines for Thesis Preparation from the Graduate and Postdoctoral studies office of McGill University. This thesis includes two manuscripts, and the contribution of each author is described below.

Chapter2: Gold nanoclusters elicit homeostatic perturbations in glioblastoma cells and adaptive changes of lysosomes

Theranostics. 2020, 10(4):1633-1648

Dusica Maysinger[1], Evan Rizzel Gran[1], Franck Bertorelle, Hussein Fakhouri, Rodolphe Antoine, Esha Sharika Kaul, Dana Samhadaneh, Ursula Stochaj

All biological experiments were performed by Evan Rizzel Gran, Esha Sharika Kaul, Dana Samhadaneh and Ursula Stochaj.

Evan Rizzel Gran performed metabolic activity assays, live-cell fluorescence imaging (LysoTracker Red, LysoSensor Green, SNARF-1, Magic Red), immunostaining assays (LAMP-2, TFEB, Proteostat). Dana Samhadaneh and Ursula Stochaj performed immunostaining assays (STAT3, LAMP-1, α-tubulin, Nrf2, HuR, G3BP-1) and ROS detection assays. Esha Sharika Kaul performed cell viability assays and immunostaining assay (Nrf2).

Franck Bertorelle, Hussein Fakhouri and Rodolphe Antoine performed the synthesis and characterization of gold nanoclusters.

The manuscript was prepared by Dusica Maysinger, Ursula Stochaj and Evan Rizzel Gran, and edited by Rodolphe Antoine.

Dusica Maysinger and Evan Rizzel Gran shared first authorship.

Chapter 3. Gold nanoclusters alter organellar state and translocation of transcription factors in human primary astrocytes

Submitted in Nanoscale (September 2020)

Evan Rizzel Gran, Franck Bertorelle, Hussein Fakhouri, Rodolphe Antoine, Martina Perić, Zeljka Sanader, Vlasta Bonačić-Koutecký, Manon Blain, Jack Antel and Dusica Maysinger

All biological experiments were performed by Evan Rizzel Gran.

Evan Rizzel Gran performed cell culture, cell viability assays, lipid peroxidation and immunostaining assays (Nrf2, HSP70, HMGB1, 4-HNE), lipid staining assays (BODIPY), ROS detection assays (CellROX Deep Red), and live-cell fluorescence imaging (MitoTracker Deep Red).

Franck Bertorelle, Hussein Fakhouri and Rodolphe Antoine performed the synthesis and characterization of gold nanoclusters.

Martina Perić, Zeljka Sanader and Vlasta Bonačić-Koutecký performed computational analyses.

Manon Blain and Jack Antel provided primary human astrocytes for biological experiments.

The manuscript was prepared by Dusica Maysinger and Evan Rizzel Gran, and edited by Rodolpe Antoine and Vlasta Bonačić-Koutecký.

Chapter 1. Literature review

1.1. Glioblastoma multiforme

Glioblastoma multiforme (GBM) is a high-grade astrocytoma and is considered the most malignant form of brain tumors(Hanif et al., 2017). High-grade tumors consist of tumor cells which proliferate more aggressively and are more likely to invade and/or metastasize, compared to tumor cells of low-grade tumors. The prognosis for GBM patients is extremely poor, given the 5-year survival rate of less than 10%. Based on clinical characteristics, GBM can be subdivided into primary and secondary GBM. Primary GBM presents *de novo*, unlike secondary GBM, which arises from lower-grade astrocytoma (Hanif et al., 2017; Nakada et al., 2011; Rajaratnam et al., 2020). GBM frequently arises in cerebral hemispheres, while rarely occurring in the cerebellum, brainstem, and spinal cord. Pathogenesis of GBM is complex, due to the heterogeneity of the tumor resulting from various genetic lesions. GBM are pharmacologically intractable cancers, known for their aggressiveness and resilience. They confer several processes for adaptation. GBM malignancy is modified by its tumor microenvironment, which can be exploited for targeted therapeutic interventions against GBM.

1.1.1. Organellar bases of adaptation

Mechanisms of malignancy in GBM cells are linked to organellar reorganization. Lysosomes, lipid droplets and mitochondria all cooperate to regulate several cellular functions (Bosch et al., 2020; Deus et al., 2020; Gao and Goodman, 2015; Henne, 2019). Organelle dynamics have a key role in cell death and survival in glioblastoma cells. There are emerging therapeutic strategies modulating these organelles, their relationships, and interactions in GBM.

Lysosomes are important organelles for energy metabolism, degradation, and recycling of cellular components (Xu and Ren, 2015) (**Figure 1**). Lysosomes also serve as a platform for cellular signaling. These membrane-bound vesicles contain hydrolytic enzymes, including lipases, nucleases, and specialized proteases called cathepsins. Cathepsins consist of serine proteases (cathepsins A and G), aspartic proteases (cathepsins D and E) and several cysteine proteases (cathepsins B, C, F, H, K, L O, S, V, X, W) (Patel et al., 2018). Maintenance of lysosomal acidity (pH 4.5-5) is crucial in the optimal activity of cathepsins (Ballabio, 2016). Endosomes containing extracellular material or autophagosomes engulfing intracellular components fuse with lysosomes for degradation. This process provides nutrients and energy for the cell. Higher levels of lysosomal markers, and enhanced lysosomal volume, degradative capacity, and biogenesis were found in GBM (Halcrow et

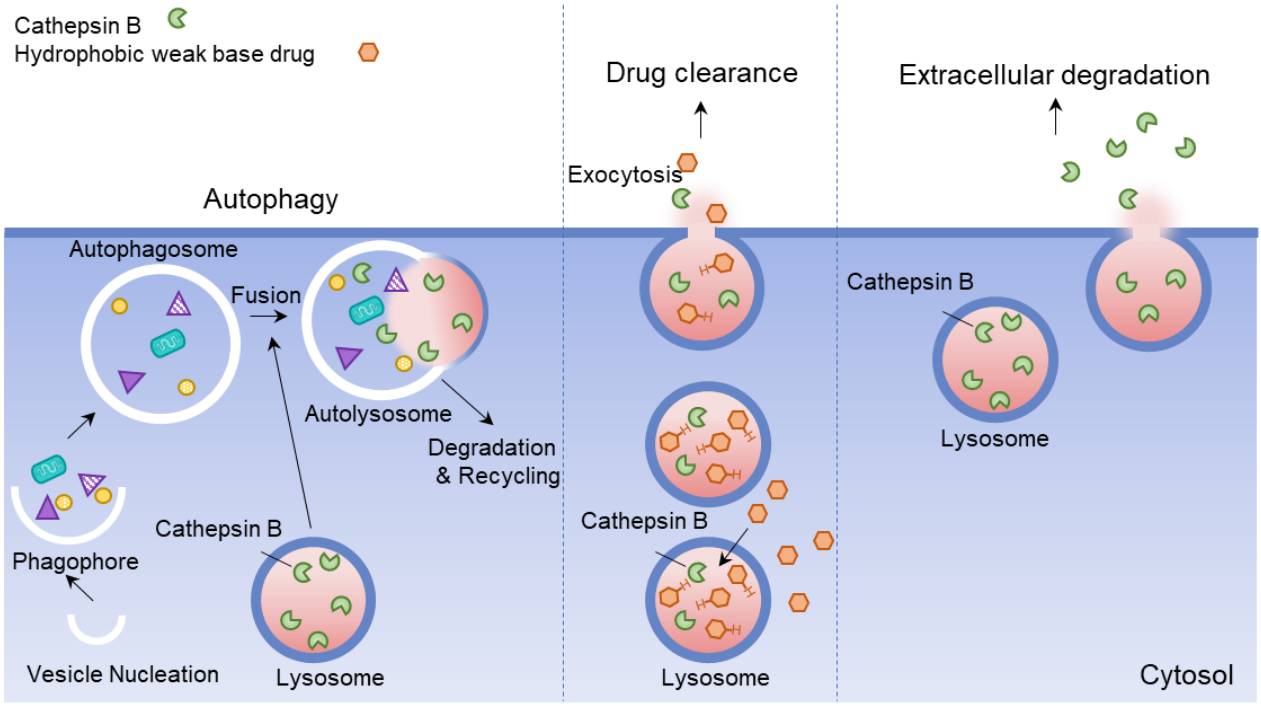

Figure 1. Functions of lysosomes in cancer. Lysosomes contain hydrolytic enzymes that degrade endogenous proteins, lipids, organelles, or exogenous cargo. Aside from their role in autophagy, lysosomes can mediate resistance by sequestering hydrophobic weak base drugs, leading to drug degradation or extracellular release from the cell. Lysosomes are also involved in remodelling of extracellular matrix to facilitate tumor growth and invasion.

al., 2019). Lysosomes are involved in regulating extracellular and cytosolic environments of GBM tumors. Lysosomal exocytosis mediates cancer progression where the release of cathepsins will degrade the extracellular matrix and facilitate tumor invasion and growth (Halcrow et al., 2019). Another major concern is that lysosomes can accumulate weak base anti-cancer drugs and nanostructures before they can reach their targets. This entrapment can lead to the degradation of therapeutics or their expulsion from the cell (Zhitomirsky and Assaraf, 2017). Enhanced lysosomal function can also provide nutrients and energy for the highly proliferative GBM cells. Lysosomes and lipid droplets (LDs) contribute to GBM adaptation and resistance to chemotherapeutics by providing energy to GBM cells.

Lipid droplets (LDs) are reservoirs of neutral lipids in cells (**Figure 2**). They are the hub for lipid metabolism and homeostasis (Islam et al., 2019). LDs are highly dynamic organelles, where their size, location and composition are tightly regulated. They sequester toxic lipid species and protect lipids from oxidation. Aside from lipid storage, LDs maintain proteostasis by associating with proteins and enabling their maturation and transient storage.

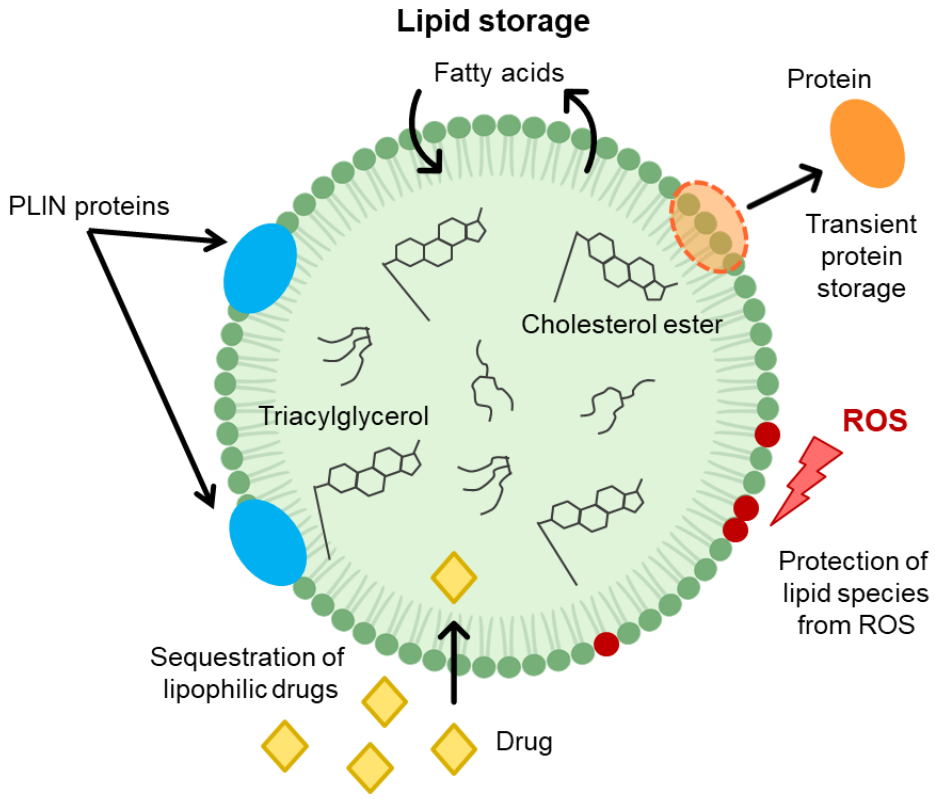

Figure 2. Functions of lipid droplets. Lipid droplets (LDs) are storage organelles for neutral lipids (e.g. triacylglycerol, cholesterol ester) and their biogenesis can protect cells from lipotoxicity and lipid peroxidation. There are various proteins which are associated to LD surface, including perilipin (PLIN). Lipid droplets can sequester hydrophobic therapeutic agents and confer resistance in cancer cells. Schematic made with ©*BioRender* (biorender.com). Adapted from "Lipid droplet–membrane contact sites–from protein binding to function" by Thiam, A. R., & Dugail, I. (2019). Journal of cell science, 132(12). Permission conveyed through Copyright Clearance Center, Inc.

GBM cells contain far more LDs than healthy neural cells (Taïb et al., 2019; Wu et al., 2020). They are critical energy sources for GBM upon energy challenges. Survival of many cancers depend on glycolysis as a source of energy (i.e., Warburg effect). GBM rely highly on fatty acid metabolism (Strickland and Stoll, 2017). Lipotoxicity in GBM cells is prevented by the enhanced LD biogenesis. Similar to lysosomes, LDs can enhance GBM resistance by sequestrating anticancer therapeutics (Cruz et al., 2020). Aside from interacting with lysosomes, LDs interact with mitochondria (Gao and Goodman, 2015).

Mitochondria are the center for cellular energy metabolism, biochemical pathways and redox signaling. Unlike lysosomes and LDs, mitochondria are not made *de novo*, but are generated from the division of pre-existing mitochondria. They contain mitochondrial genome separate from the nuclear genome (Friedman and Nunnari, 2014). Mitochondria

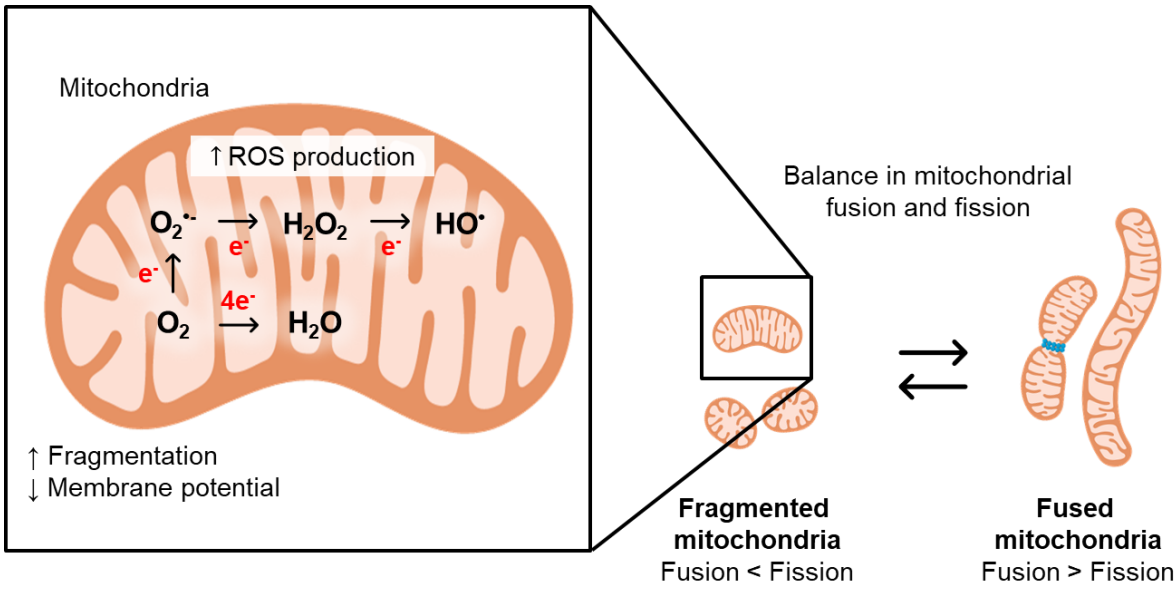

Figure 3. Mitochondria as major sources of reactive oxygen species. Regulation of mitochondrial dynamics and rate of fusion are important in cellular adaptation to changing conditions. Dysregulated mitochondrial dynamics can lead to the accumulation of reactive oxygen species, and as a result, mitochondrial fragmentation and loss in membrane potential. Schematic made with ©BioRender (biorender.com).

morphologies range from small globules to elongated tubules, depending on cell types, energy demand and stress conditions. Changes in morphology can suggest disruption in mitochondrial dynamics and function (Li et al., 2020) (**Figure 3**). Regulation of fusion and fission of mitochondria have important consequences on mitochondria functional output and ability of cells to adapt to different conditions (Westermann, 2010). Morphological and functional abnormalities in mitochondria have been identified in GBM tumors. GBM possess mutations in mitochondrial DNA, such that these mutations force reprogramming of mitochondrial dynamics and bioenergetic states. As they are implicated in cell survival and the execution of cell death pathways, mitochondria have become a promising target for GBM treatment (Li et al., 2020).

1.1.2. Molecular bases of adaptation

Resilience of GBM to therapy makes this brain tumor currently fatal. They not only have altered metabolism and reorganised organelles, but also have molecular adaptive redox-responsive proteins that contribute to resistance in GBM.

Transcription factor EB (TFEB) is a master regulator of genes of the Coordinated Lysosomal Expression and Regulation (CLEAR) gene network. TFEB activity thereby stimulates lysosomal biogenesis and autophagy. TFEB is a member of the MiT/TFE family, consisting of three other members: microphthalmia-associated transcription factor (MITF), transcription factor E3 (TFE3) and transcription factor EC (TFEC) (Perera et al., 2019). TFEB also participates in the regulation of several signaling pathways in cellular anabolism. The physiological role of TFEB activation is to maintain cellular homeostasis. TFEB activation can lead to degradation of damaged lipids, RNA, proteins, and dysfunctional organelles (Napolitano and Ballabio, 2016). Mitophagy can be stimulated by TFEB activation to reduce mitochondrial dysfunction, mitochondrial swelling, and fragmentation. TFEB activation is tightly regulated by post-translational modifications, which affects its protein interactions and cellular localization (**Figure 4**). TFEB is inactivated via phosphorylation on positions Ser142 and Ser 211 by mechanistic target of rapamycin complex 1 (mTORC1) on the surface of lysosomes (Martina et al., 2012). Phosphorylated Ser211 allows binding of chaperone 14-3-3 to TFEB, preventing its translocation into the

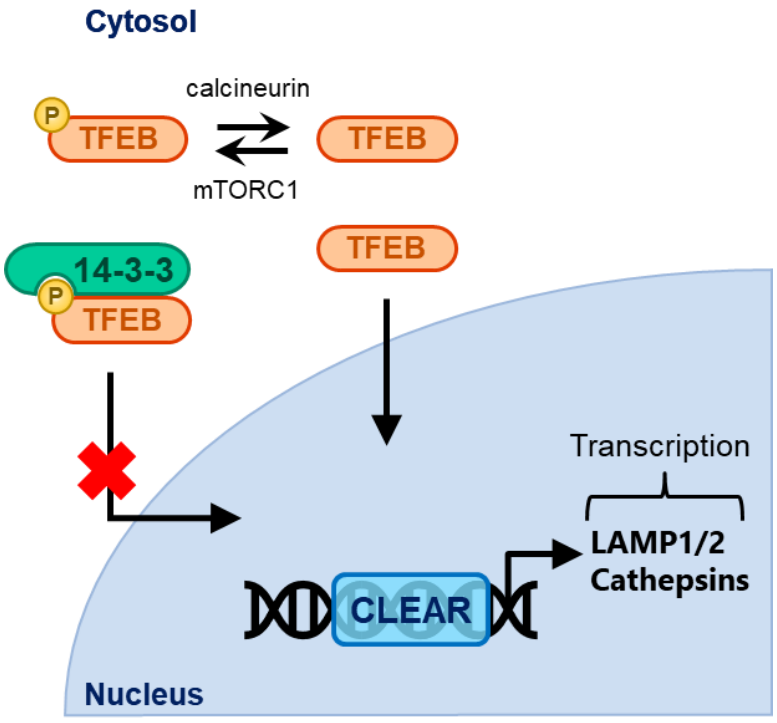

Figure 4. Regulation of TFEB activity and translocation. Phosphorylated TFEB is inactivated and retained in the cytosol. Dephosphorylation of TFEB by calcineurin drives its nuclear translocation, where TFEB bind to CLEAR genes for transcriptional activation (e.g. Lysosomal associated membrane protein 1/2 (LAMP1/2), cathepsins).

nucleus (Roczniak-Ferguson et al., 2012). In nutrient-deprived conditions or cellular stress, the phosphatase calcineurin is activated and mediates dephosphorylation of TFEB (Medina et al., 2015). Dephosphorylated TFEB rapidly translocates into the nucleus, thereby activating the expression of its target genes. Dysregulated lysosomal function is characteristic in GBM. Several studies report that TFEB can promote clearance of drugs and nanostructures, by enhancing autophagy and lysosomal function (Zhao et al., 2020). Enhanced autophagic flux is linked to greater insensitivity to radiation in GBM, where silencing of TFEB sensitized GBM cells to chemotherapy and radiation (Mitrakas et al., 2018).

As autophagic flux is enhanced in stressful conditions, cells can also engage the antioxidant defense system by activating nuclear factor erythroid 2-related factor 2 (Nrf2) (**Figure 5**). Nrf2 is the key regulator of over a hundred cytoprotective and detoxifying genes

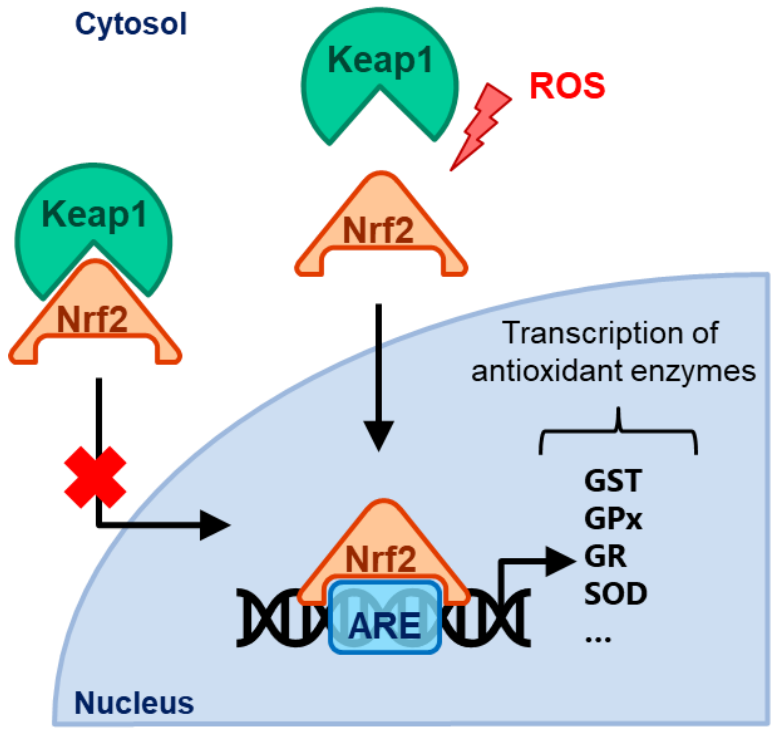

Figure 5. Overview of Nrf2-Keap1 system. Under physiological conditions, Nrf2 is complexed with Keap1 in the cytosol, preventing its nuclear translocation. The Nrf2-Keap1 complex is then targeted for proteasomal degradation. Upon oxidation, Keap1 dissociates from Nrf2 and, as a result, Nrf2 enters the nucleus. Inside the nucleus, Nrf2 binds antioxidant response element (ARE) sequences to activate transcription of antioxidant proteins (e.g. glutathione-*S*-transferase (GST), glutathione peroxidase (GPx), glutathione reductase (GR), superoxide dismutase (SOD)).

(Nakajima et al., 2011). Nrf2 is normally kept in the cytosol by Kelch-like erythroid cell-

derived protein with CNC homology-associated protein 1 (Keap1). Nrf2 bound to Keap1 is destined for proteasomal degradation (Kansanen et al., 2013). Keap1 has a total of 27 cysteine residues in humans, making its structure sensitive to oxidation (Kansanen et al., 2009). Oxidation of C151, C273 and C288 alters Keap1 conformation such that its affinity to Nrf2 is decreased. Upon oxidative or electrophilic stress, there is increased accumulation of nuclear Nrf2. Keap1 is oxidized and Nrf2 is released, leading to its translocation into the nucleus. Nrf2 will activate expression of target genes, including glutathione peroxidase, glutathione reductase, heme oxygenase, NAD(P)H quinone dehydrogenase and much more. Nrf2 and glutathione are key mediators of resistance against oxidative stress, which is a concern in GBM tumors (Kansanen et al., 2013; Zhu et al., 2014).

Other mediators of GBM resistance are proteins from the heat shock protein (HSP) families. HSP are categorized into families based on their sizes: small HSPs, HSP60, HSP70, HSP90 and HSP100. They are chaperones for protein or polypeptides in the cytosol, endoplasmic reticulum (ER), and mitochondria (Huang et al., 2008). Their expression is induced in response to physical and chemical stresses, oxidative stress, and proteolytic aggression. HSP27 is a member of the small HSPs and mainly resides in the cytosol, but can be found in the nucleus and ER (Vidyasagar et al., 2012). In contrast, HSP60 is typically found in mitochondria (Cappello et al., 2008). HSP70 and HSP90 families represent the most ubiquitous HSPs that can be found in the cytosol, nucleus, ER and mitochondria (Beere, 2004). HSP100 chaperones are not found in animals or humans (Zolkiewski et al., 2012). HSPs role is to relieve cellular stress by maintaining proteostasis. They can promote degradation or refolding, and inhibit aggregation of misfolded proteins (Beere, 2004). HSPs can also stabilize proteins involved in cell survival and proliferation, such as protein kinase B (AKT), Raf-1, tumor protein p53, and epidermal growth factor receptor (EGFR) (Ahsan et al., 2012; Sato et al., 2000; Schulte et al., 1995). In malignant cells, this can be exploited to promote their survival. HSP70 can inhibit formation of apoptosomes and the release of pro-apoptotic factor cytochrome c (Pandey et al., 2000). Elevated HSP70 in tumors are reported as a biomarker for poor prognosis in GBM patients (Lämmer et al., 2019).

Intracellular Functions	**Extracellular Functions**
DNA repair	Angiogenesis

DNA stability	Chemotaxis
Replication	Immunity
Transcription	Inflammation
	Tissue remodeling

Table 1. Functions of HMGB1 inside and outside the cell. Intracellularly, HMGB1 is involved in DNA replication and gene transcription. HMGB1 sustains DNA stability and participates in DNA repair (Lange and Vasquez, 2009; Tang et al., 2011). Once released from the cell, HMGB1 can regulate angiogenesis, inflammation, immunity, chemotaxis, and tissue remodeling (Andersson et al., 2018).

Poor prognosis of GBM patients is also associated with high levels of high mobility group box 1 (HMGB1) (Seidu et al., 2017). HMGB1 is a nuclear protein which diverse biological functions (**Table 1**). Post-translational modifications dictate the localization of HMGB1, as well as its functions. HMGB1 primarily resides in the nucleus, where it acts as a DNA chaperone and facilitates DNA binding of other transcription factors (Andersson et al., 2018). HMGB1 also plays a role in DNA repair and replication (Lange and Vasquez, 2009). Upon hyperacetylation, HMGB1 is driven outside the nucleus and into the cytosol, where it can be eventually released into the extracellular space by active secretion or by leaking through damaged plasma membranes (Hong et al., 2019). HMGB1 can interact with several proteins (e.g. lipopolysaccharide (LPS), interleukin-1 (IL-1)) and activate receptor for advanced glycation end-products (RAGE) and toll-like receptors (TLR) (Paudel et al., 2018). HMGB1 is sensitive to oxidants, where oxidation of three cysteine residues can dictate its biological functions: Cys23, Cys45, Cys106. In a quiescent state, these three key cysteine residues remain fully reduced thiols (Andersson et al., 2018). Mild oxidation results in a disulfide bond between Cys23 and Cys45, where HMGB1 takes on a potent pro-inflammatory activity with a strong affinity to toll-like receptor 4 (TLR4). As such, HMGB1 is a delayed and potent mediator of inflammation (**Figure 7**). Fully oxidized HMGB1 is irreversible, and in this state, HMGB1 has no known immune function (Andersson et al., 2018). HMGB1 is also important for vascular remodeling in the tumor microenvironment, as it exhibits pro-angiogenic properties. Studies reveal that release of HMGB1 into the extracellular space leads to dendrite loss and neurotoxicity that is dependent on glial cells

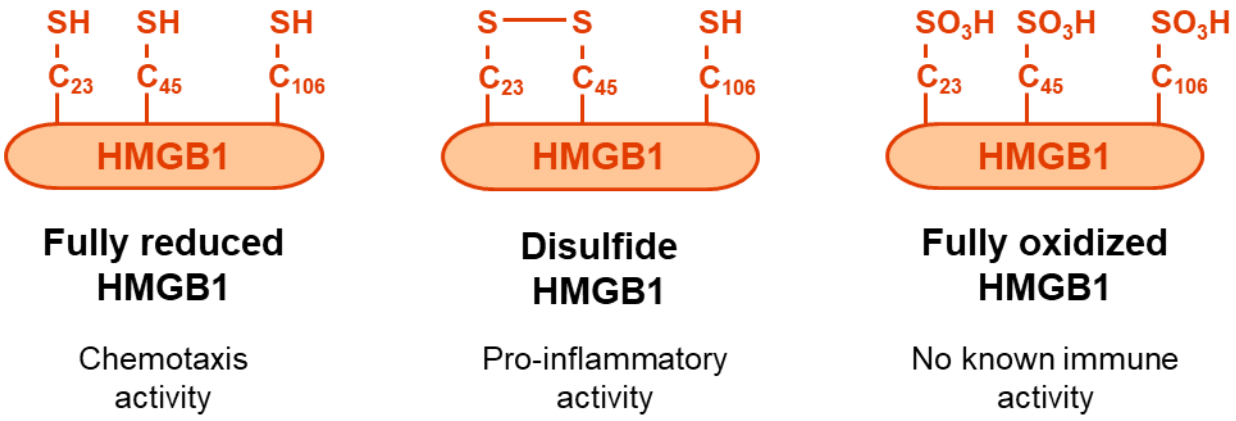

Figure 6. Redox modulation of HMGB1 functions. HMGB1 can be passively released from dead cells or secreted by cells under stress. Upon mild oxidation, HMGB1 mediate cytokine-inducing activity. Further oxidation of cysteine residues form sulfonyl HMGB1, which have no cytokine or chemotaxis activity. Adapted from "A Janus Tale of Two Active High Mobility Group Box 1 (HMGB1) Redox States" by Tang, D., Billiar, T.R. & Lotze, M.T. Mol Med 18, 1360–1362 (2012). Permissions under a Creative Commons Attribution-NonCommercial-NoDerivatives 4.0 International License.

(Rosciszewski et al., 2019). HMGB1 release from dying cells induces reactivity of astrocytes and microglia, where RAGE and TLR pathways are engaged. In contrast, in the absence of glial cells, HMGB1 minimally affects neuronal survival or dendrite morphology and number (Rosciszewski et al., 2019). These studies warrant assessment of HMGB1 cellular distribution upon GBM treatment with pharmacological agents and nanostructures.

These four proteins are important molecular bases of adaptation and survival in GBM. It will be important to examine how these factors are affected in response to treatments in glioblastoma cells and cells of the tumor microenvironment.

1.1.3. Microenvironment

GBM tumor microenvironment includes complex and heterogenous cellular networks consisting of non-cancerous cells, such as reactive astrocytes, microglia, infiltrating and resident immune cells, endothelial cells, vascular cells and much more (Schiffer et al., 2019) (**Figure 8**). These cells support GBM tumor survival, growth, and invasion. Astrocytes are paramount players in the progression of GBM as they can provide chemo- and immune-protection for GBM cells (Kim et al., 2011).

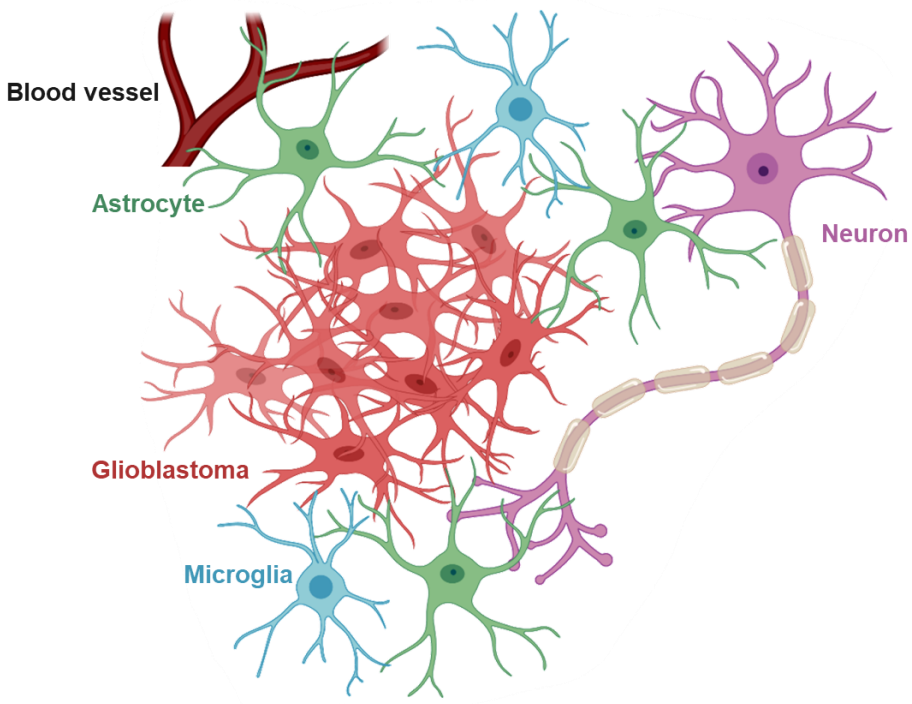

Figure 7. Non-cancerous cells in GBM tumor microenvironment. The tumor microenvironment is made of complex cellular networks of resident and infiltrating host cells. Schematic made with ©BioRender (biorender.com).

1.1.3.1. Astrocyte-glioblastoma crosstalk

Astrocytes are specialized cells that play a supportive role in the central nervous system. Although neurons typically take the spotlight as the fundamental units of the nervous system, astrocytes have an undeniable importance in maintaining neural homeostasis, synaptic activity, metabolism and regulation of blood circulation in the central nervous system (CNS) (Sofroniew and Vinters, 2010). A single astrocyte can branch over multiple cortical layers and be involved in up to 2 million synapses at a time (Fields et al., 2013). They play a pivotal role in protecting neurons and secreting endogenous antioxidants for the detoxification of ROS. In response to any form of CNS insult, astrocytes become reactive and work to limit damage. However, these glial cells can become overwhelmed, and can contribute to neuronal injury and neurotoxicity by releasing pro-inflammatory molecules and ROS. In these conditions, astrocytes shift from their protective role to a detrimental one. Involvement of astrocytes to GBM tumor and survival has been established (Henrik Heiland et al., 2019). Cell-to-cell contact mediates communication between GBM and astrocyte (Matias et al., 2018). Astrocytes release

notable levels of factors into the tumor microenvironment (e.g. transforming growth factor β (TGF-β), tumor necrosis factor-α (TNF- α), interleukin-6 (IL-6)) leading to enhanced GBM invasion and proliferation (Brandao et al., 2019; Matias et al., 2018). As such, tumor-associated astrocytes exhibit a pro-tumorigenic role in GBM environment and must not be overlooked in the treatment of GBM.

1.1.4. Treatment

Standard treatment for GBM is multimodal, comprising of surgical resection, radiotherapy, and concurrent chemotherapy. There are several limits to chemotherapy for GBM, the main limitation being penetration of the blood brain barrier (BBB). Molecules of lipophilic nature that are less than 400 Da in size are more likely to cross the BBB (Harder et al., 2018). There are currently three FDA-approved chemotherapeutic agents for adult patients with GBM: temozolomide, bevacizumab and carmustine (**Table 1**).

Temozolomide (TMZ) is the traditional chemotherapy for newly diagnosed patients, which is given concurrently to radiotherapy. TMZ is an alkylating agent which methylates purine bases on either DNA or RNA (Lee, 2016). If DNA repair mechanisms fail to remove alkylated sites, errors can arise during subsequent DNA replication, potentially leading to cell cycle arrest, and ultimately apoptosis. As rapidly dividing cells, cancer cells are more susceptible to DNA-alkylating agents such as TMZ. Unfortunately, over half of GBM patients do not respond to TMZ. This resistance is mainly explained by the overexpression of O^6-methylguanine methyltransferase (MGMT), an enzyme which can reverse the alkylating effects of TMZ (Lee, 2016). Alternative chemotherapeutic is therefore required for these patients.

Bevacizumab (BEV) is given to recurrent GBM cases, and has a different mechanism of action than TMZ (Cohen et al., 2009; Liu et al., 2019; Lyon and Huang, 2018). BEV is a monoclonal antibody targeting vascular endothelial growth factor (VEGF). As an anti-angiogenic agent, BEV interferes with GBM tumor growth by neutralizing VEGF biological activity, restricting neovascularization of the tumor microenvironment. Interfering with this process has been shown to stunt tumor growth. It is to be noted that GBM tumors can become resistant, more aggressive and invasive after BEV treatment (Miranda-Gonçalves et al., 2017; Piao et al., 2013).

Carmustine is an alternative for either newly diagnosed or recurrent GBM cases (Chowdhary et al., 2015). Similar to TMZ, carmustine is a DNA and RNA alkylating agent. Carmustine can also bind and inhibit enzymes by carbamoylation, including DNA repair enzymes, and glutathione reductase. Carmustine treatment is less advised, as it can cause severe toxicity to the bone marrow, liver and kidney (Rajaratnam et al., 2020).

Drug	Administration	Target(s)	Effect(s)
Temozolomide (TMZ, $C_6H_6N_6O_2$)	Intravenous infusion: 75 mg/m^2/day for 6 weeks, followed by 6 cycles of 150-200mg/m^2/day for 5 consecutive days of a 28-day cycle (Wick et al., 2009)	Purine bases of DNA or RNA	Formation of O^6-methylguanine DNA and RNA adducts (Fernandes et al., 2017)
Bevacizumab (BEV)	Intravenous infusion: 10 mg/kg/2 weeks	All isoforms of human VEGF[3]	Steric blocking of VEGF binding to VEGFR-1 and VEGFR-2 (Ajlan et al., 2017)
Carmustine ($C_5H_9Cl_2N_3O_2$)	Intravenous infusion: 150-200 mg/m^2 every 6 weeks (Rahman et al., 2014)	DNA, RNA, proteins	Formation of methylated DNA and RNA adducts or crosslinks, and carbamoylation of proteins (Chowdhary et al., 2015)

Table 2. Current FDA-approved drugs for glioblastoma treatment.

1.1.5. Recurrence

Despite undergoing surgical resection of the tumor, radiation and chemotherapy, most patients experience recurrence of the malignancy. Recurrence is typically reported within 6 to 8 months of conventional treatment and is nearly inevitable (Easaw et al., 2011). Genetic profiling reveal over a quarter of patients' post-treatment have tumors that do not match their primary molecular diagnostic (Hudson et al., 2018). Often, these recurring tumors acquire resistance with heightened immune suppression and invasiveness. Given the resilience and aggressiveness of GBM, more effective therapeutic approaches are in need.

1.1.6. Clinical trials & therapeutic prospects

Continued efforts to find alternative treatments are currently underway. Many clinical trials feature combination therapies, as monotherapy has been shown to be less effective against the heterogeneous nature of GBM tumors. There are over 200 clinical trials that are to be completed between 2020-2028 (Rajaratnam et al., 2020). These include anti-

angiogenics, immunotherapy, oncolytic viral therapy, tyrosine kinase inhibitors, and much more.

To overcome the limitations of GBM treatment, increasing number of prospective treatments against GBM are nano-based strategies (Awasthi et al., 2018; Shi et al., 2017). More than 40% of new chemical entities are inadequately soluble in water and more than half of phase III clinical trials fail due to poor efficacy and body distribution (Fogel, 2018; Savjani et al., 2012). Nano-formulated strategies can circumvent these issues by providing several benefits, such as (1) improved pharmacokinetics (e.g., stability, solubility, bioavailability, circulation half-life), (2) spatial and/or temporal control of drug release, (3) co-delivery of drugs, (4) enhanced penetration to the BBB, (5) bio-imaging properties, and (6) radio-sensitizing effects. Nanoparticle-based imaging can also be exploited for selecting patients eligible for nanotherapeutics or theranostics. The extent of accumulation of "tracer" nanoparticles helps predict the accumulation of "therapeutic" nanoparticles, and by extension, the patient's response to the nano-based therapy (Tietjen and Saltzman, 2015). In light of clinical translation and commercialization of nanotherapies, a detailed understanding of biological responses to the nanostructures is required.

1.2. Nano-based therapeutics

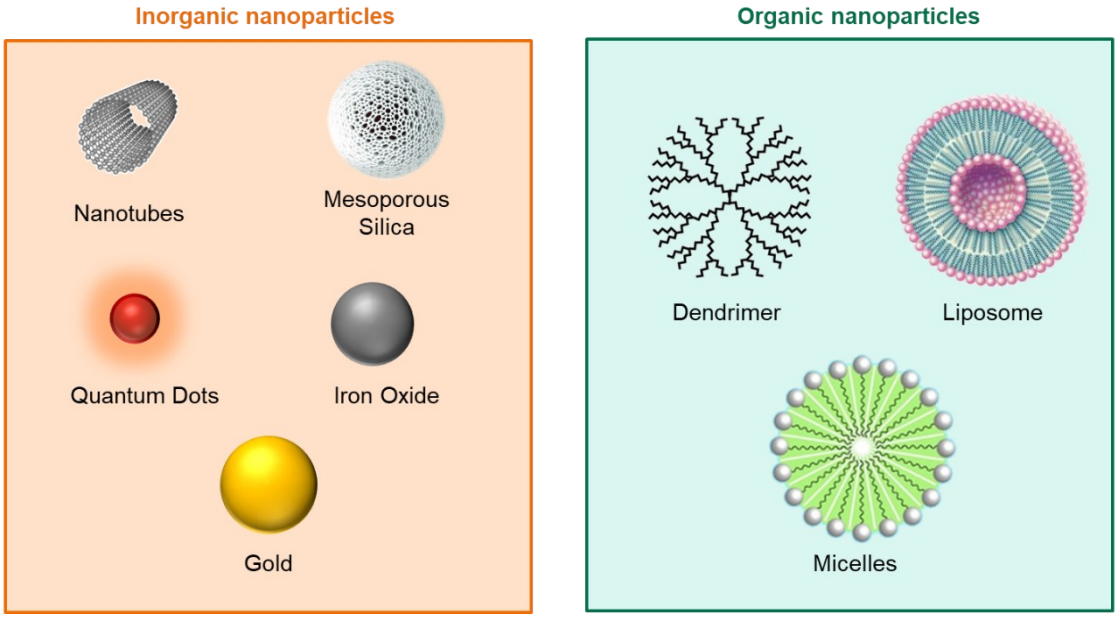

Figure 8. Examples of organic and inorganic nanostructures utilized in oncology.

1.2.1. Key properties of nanostructures

Size, shape, orientation, and surface modifications of nanostructures can influence their effects in biological systems. Their biocompatibility, cellular uptake, circulation time, renal clearance, immunogenicity, and toxicity are some of the properties that can be affected by such parameters. It is therefore important to understand the relation between physicochemical properties of nanostructures and biological interactions.

1.2.1.1. Size, shape & orientation

Several studies show size, shape and orientation affect the basal uptake of nanostructures (Herd et al., 2013). Rate of uptake is also dependent of nanostructure morphology. There are several different pathways for internalization of nanostructures: phagocytosis, macro-pinocytosis, caveolin-dependent endocytosis, clathrin-dependent endocytosis, receptor-mediated endocytosis, non-specific uptake and translocation (Zhang et al., 2015). Uptake of nanostructures is not necessarily mediated by a single pathway. Smaller nanostructures are more easily internalize by cells, than the larger ones (Wu et al., 2019). Uptake pattern ultimately initializes different responses of the cell and downstream cellular pathways (Zhang et al., 2015).

Size and shape also affect renal clearance efficiency of nanostructures. For example, short-rod shaped nanostructures primarily accumulate in the liver, whereas clearance of long-rod shaped nanostructures is obstructed in the spleen (Huang et al., 2011). This can therefore affect systemic circulation of nanostructures. Kidneys have effective size cutoff at 6 to 8 nm (Du et al., 2017). To minimize kidney retention, many nano-based imaging contrast agents were synthesized to be smaller than this cutoff. However, it has been shown that, although larger nanostructures can be obstructed by the glomerular filtration barrier, too small of a nanostructure (≤1 nm) can be slowed down by the glomerular glycocalyx (Du et al., 2017).

1.2.1.2. Charge

Charge can influence the uptake of nanostructures, as well as their cytotoxicity. Generally, positively charged nanostructures show a more efficient uptake and less cytotoxicity, than negatively charged nanostructures of similar sizes (Fröhlich, 2012). Negatively charged nanostructures bind less efficiently to cell surfaces due to the repulsion between the negatively charged cellular membrane (Chithrani et al., 2006). Positively charged nanostructures also have a greater rate of endocytosis compared to

negatively charged nanostructures (Escudero-Francos et al., 2017). It is to be noted that positively charged nanostructures are also more apt in disrupting plasma membrane, mitochondria, and endo-lysosomal compartments (Fröhlich, 2012).

1.2.1.3. Surface composition

Surface composition is just as important as size and shape at determining the fate and effects of nanostructures in biological systems (Lundqvist et al., 2008). Surface composition can also influence the size, shape, and charge of a nanostructure. Nanostructures can be linked to different molecules of interest, such as diagnostic, therapeutic, theranostic or bio- molecules. Functionalization can also enhance biocompatibility, biodistribution and clearance. For example, common surface modifications of nanostructures to enhance their biocompatibility and/or systemic circulation include polymers (e.g. PEG, PGLA, PLA), biomolecules (e.g. peptides, proteins), and carbohydrates (e.g. starch, dextran) (Thiruppathi et al., 2017). It is important to note that surface composition can exert cell-type dependent effects (Du et al., 2017; Lasagna-Reeves et al., 2010; Sohaebuddin et al., 2010).

1.2.2. Gold nanostructures

Unlike many inorganic nanostructures, gold nanostructures show efficient clearance from tissues, including the brain, after repeated administration in mice. Results from Yang et al. suggest that gold nanostructures can be cleared faster than nanostructures of similar size, shape and concentration, but with different elemental composition (e.g. Ag) (Yang et al., 2017). Different composition of the nanoparticle core could influence the dynamic protein interaction and/or binding, thereby affecting the accumulation of nanostructures in different organs (Hirn et al., 2011; Yang et al., 2017). Renal clearable gold nanoparticles have also been demonstrated in monkeys, where their size, shape and surface composition play an important role (Xu et al., 2018; Yu et al., 2019).

1.2.2.1. Gold nanoparticles

Gold nanoparticles (AuNPs) typically range between 10 to 500 nm. They have shapes, most commonly into spheres, shells, flowers, and rods. As stable, robust and of the least toxic inorganic nanostructures, AuNPs can be used for GBM diagnosis and therapy (e.g. a diagnostic tool for computerized tomography (CT), and nanocarrier for drugs) (Dreaden et al., 2012; Jin et al., 2010; Norouzi, 2020). *In vitro* and *in vivo* studies

show the ability of AuNPs to sensitize tumor cells to radiotherapy (Borran et al., 2018; Hainfeld et al., 2008). The radio-sensitizing effects of AuNPs were also associated with greater survival times in mouse models of GBM (Joh et al., 2013). There are already a few gold nano-based therapies currently approved by the FDA, as well as an increasing number of clinical trials on gold-based nanotechnology for both therapy and diagnostic purposes. Amongst these clinical trials, there is a Phase I clinical trial evaluating the safety of spherical gold nanoparticles coated with nucleic acids (NU-0129) in GBM patients (Kumthekar et al., 2019).

Recent advances in synthetic chemistry have allowed the synthesis of gold nanozymes, a new class of gold nanostructures much smaller than 5 nm, exhibiting enzyme-like activity. Given their distinguished ultra-small sizes, this subset of gold nanostructures showcases unique physical and chemical properties. These nanostructures are termed gold nanoclusters.

1.2.2.2. Gold nanoclusters

Gold nanoclusters (AuNCs) are nanostructures composed of a few to a hundred gold atoms in their core, measuring typically around 1-3 nm (Kang et al., 2018). Similar to gold nanoparticles, they are utilized for *in vivo* imaging, gene delivery, and photodynamic therapy (Vankayala et al., 2015). Additionally, they exert catalytic activity, and are therefore named "gold nanozymes". Due to their inorganic nature, these nanozymes are more stable and resistant to degradation compared to natural enzymes (Zhang et al., 2020). Several studies report anti- and pro-oxidant effects of gold nanoclusters, similar to the activity of peroxidases and catalases (Zhang et al., 2020) (**Figure 10**). These properties are dependent on their size and surface modifications.

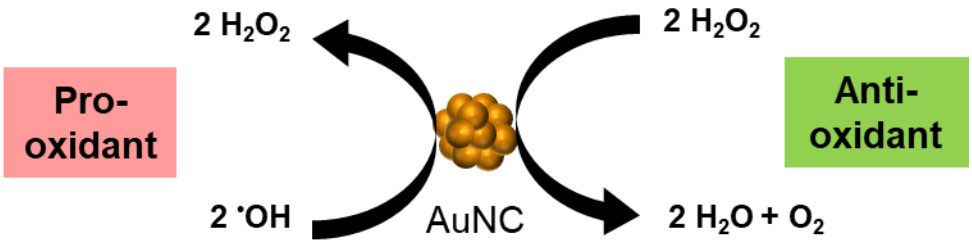

Figure 9. Pro- and anti-oxidant properties of gold nanoclusters.

As modulators of reactive oxygen species in biological systems, they could be useful nanotherapeutics, diagnostics or theranostics in oncology.

1.3. Rationale and Objectives

Gold nanoclusters (AuNCs) are a unique type of gold nanostructure well-defined at the atomic level. Their physicochemical properties are dependent on the accessibility of their gold surface and the composition of their surface ligand. AuNCs can mimic redox-regulating enzymes. The most common yet deadliest form of brain cancer, glioblastoma multiforme (GBM), shows altered redox status in comparison to healthy astrocytes. AuNCs may provide a new therapeutic approach to GBM treatment as they are modulators of reactive oxygen species in GBM cells.

The objective of this thesis is to show if and how AuNC properties (size and surface composition) can be utilized for elimination of GBM through modulation of astrocytes in GBM microenvironment. The modulatory effects of AuNCs were assessed at the organellar level (lysosomes, mitochondria, lipid droplets) and associated redox-responsive transcription factors. These findings will show which of the AuNC properties play a critical role in modulating the status of human malignant and non-malignant astrocytes.

Connecting text

Most nanomaterials, including AuNCs, are internalized by the endo-lysosomal system in various cell types. Lysosomes are acidic organelles responsible for breaking down not only cellular components, but also internalized drugs and nanostructures.

In **Chapter 2**, we describe the effects of AuNCs with a 15-gold atom core (Au_{15}) with either glutathione or polyethylene glycol (PEG) on lysosomal homeostasis in human glioblastoma cells. These effects were detected by changes in lysosomal biogenesis, distribution, acidity, and enzymatic activity, and associated molecular pathways.

Studies here show homeostatic perturbations in GBM cells treated with AuNCs. Results show that lysosomes are involved in the adaptation of human glioblastoma cells to AuNC-induced cytotoxicity.

Chapter 2. Gold nanoclusters elicit homeostatic perturbations in glioblastoma cells and adaptive changes of lysosomes

Maysinger, D.,[1] Gran, E. R. [1], Bertorelle, F., Fakhouri, H., Antoine, R., Kaul, E. S., Samhadaneh, D.M. and Stochaj, U. (2020) Gold nanoclusters elicit homeostatic perturbations in glioblastoma cells and adaptive changes of lysosomes. *Theranostics*, *10*(4), p.1633-1648.

[1] Both authors contributed equally.

2.1. Abstract

Unique physicochemical features place gold nanoclusters at the forefront of nanotechnology for biological and biomedical applications. To date, information on the interactions of gold nanoclusters with biological macromolecules is limited and restricts their use in living cells. Our multidisciplinary study begins to fill the current knowledge gap by focusing on lysosomes and associated biological pathways in U251N human glioblastoma cells. We concentrated on lysosomes, because they are the intracellular destination for many nanoparticles, regulate cellular homeostasis and control cell survival. Quantitative data presented here show that gold nanoclusters (with 15 and 25 gold atoms), surface-modified with glutathione or PEG, did not diminish cell viability at concentrations ≤1 μM. However, even at sublethal concentrations, gold nanoclusters modulated the abundance, positioning, pH, and enzymatic activities of lysosomes. Gold nanoclusters also affected other aspects of cellular homeostasis. Specifically, they stimulated the transient nuclear accumulation of TFEB and Nrf2, transcription factors that promote lysosome biogenesis and stress responses. Moreover, gold nanoclusters also altered the formation of protein aggregates in the cytoplasm. The cellular responses elicited by gold nanoclusters were largely reversible within a 24-hour period. Taken together, this study explores the subcellular and molecular effects induced by gold nanoclusters and shows their effectiveness to regulate lysosome biology. Our results indicate that gold nanoclusters cause homeostatic perturbations without marked cell loss. Notably, cells adapt to the challenge inflicted by gold nanoclusters. These new insights provide a framework for the further development of gold nanocluster-based applications in biological sciences.

Keywords: nanomaterials, cell organelle, organellar pH, lysosome positioning, proteostasis, cellular stress response

2.2. Introduction

The unique physical and chemical properties of gold nanoclusters (AuNCs) make them attractive nanostructures for diverse applications. In addition to imaging, various functionalized AuNCs have been used as biosensors, diagnostic tools or nanocarriers for drugs (Jin et al., 2016; Nandi et al., 2018; Su et al., 2019; Vankayala et al., 2015). Some AuNCs have catalytic properties that are potentially useful for biomedical investigations (Zheng et al., 2017).

AuNCs described so far contain between 11 and more than 270 gold atoms (reviewed in Kang et al., 2018). AuNCs with 25 gold atoms stand out, because they are stable, easy to prepare, and methods for their functionalization are well established. A variety of functionalization approaches to modify AuNC surfaces have been used to enhance their dispersibility, solubility, and minimize or prevent aggregation (reviewed in (Crawford et al., 2019; Kang and Zhu, 2019). AuNC modifications play an essential role for *in vivo* experiments, because gold atoms without adequate ligand protection can act as nanozymes and change the intracellular redox status (Ao et al., 2017; Liu et al., 2016).

A common functionalization strategy is ligand exchange under conditions that are appropriate for the selected ligand and AuNC (Su et al., 2019; Zeng et al., 2015). These protocols have been applied to produce thiol-stabilized AuNCs that frequently contain glutathione (GSH). Such AuNCs have been used for bioimaging in cells and *in vivo* (Vankayala et al., 2015). To date, in-depth studies on AuNCs were mostly performed *in vitro* using cell-free model systems.

Following cellular uptake, most nanomaterials will locate to lysosomes (Kodiha et al., 2015; Wang et al., 2013). These membrane-delimited organelles maintain cellular homeostasis through the degradation of damaged organelles, misfolded proteins, and internalized exogenous particles (Lawrence and Zoncu, 2019; Oyarzún et al., 2019; Xu and Ren, 2015). Lysosomes also sense the cellular nutrient status, respond to stress and exocytose macromolecular material (Lawrence and Zoncu, 2019; Perera and Zoncu, 2016; Raben and Puertollano, 2016; Samie and Xu, 2014).

Lysosomal activities are controlled on multiple levels. The activities of lysosomal enzymes, including various proteases, depend on the low pH of the organelle. Furthermore, lysosome biogenesis is regulated by transcription factors EB (TFEB) and E3 (TFE3) (Raben

and Puertollano, 2016; Settembre and Ballabio, 2014). TFEB and TFE3, upon translocation into the nucleus, promote the expression of genes that stimulate lysosome biogenesis. Aside from lysosome abundance, their positioning within the cell is also critical, because lysosomal pH and enzymatic activities are determined by the organelle location (Bonifacino and Neefjes, 2017; Cabukusta and Neefjes, 2018). Specifically, lysosomes adjacent to the nucleus are characterized by a more acidic pH, whereas organelles closer to the cell periphery are less acidic. As lysosomes control a multitude of cellular processes, their dysfunction has been associated with cancer, neurological or metabolic disorders (Oyarzún et al., 2019; Samie and Xu, 2014).

Nanomaterials can alter different aspects of cell physiology, and they may elicit stress responses (Kodiha et al., 2016; Samhadaneh et al., 2019; Umair et al., 2016). Such stress-induced changes are exemplified by the nuclear translocation of the transcription factor Nrf2 (nuclear factor erythroid 2-related factor 2, NFE2L2) (Schmidlin et al., 2019; Traboulsi et al., 2017) and the formation of cytoplasmic stress granules (Anderson et al., 2015; Mahboubi and Stochaj, 2017; Protter and Parker, 2016). While Nrf2 helps to restore redox homeostasis through the expression of antioxidant-related genes (Cloer et al., 2019), stress granule formation promotes cell survival under harmful growth conditions (Anderson et al., 2015; Mahboubi and Stochaj, 2017; Protter and Parker, 2016).

In previous studies, AuNCs were reported to have low toxicity in glioblastoma cells (Cifuentes-Rius et al., 2017). However, the impact of AuNCs on cell processes remain largely unknown (Su et al., 2019), and sub-lethal effects or adaptive responses have not been defined.

For the work described here, we selected AuNCs with 15 or 25 gold atoms functionalized with glutathione (GSH) or polyethylene glycol (PEG) to evaluate their impact on organelles and other subcellular compartments in glioblastoma cells. Our focus was on lysosomes and cellular stress responses, because they provide a measurable readout for nanoparticle-induced effects on cell physiology. Collectively, the presented studies suggest that in glioblastoma cells AuNCs prompt the adaption of lysosomal properties and stress-responsive pathways. The characterization of these processes at the cellular and molecular level is crucial for the further development of AuNC-based theranostics.

2.3. Results and Discussion

2.3.1. Synthesis and characterization of gold nanoclusters

Glutathione-protected AuNCs were synthesised via a controlled reduction of gold (see Methods section). The monodispersity of gold cluster sizes ($Au_{15}SG_{13}$ and $Au_{25}SG_{18}$) was verified by ESI-mass spectrometry. The PEGylated AuNCs were prepared by covalent peptide coupling of PEG_{5000}-NH_2 to the surface carboxylic acid groups of GSH (**Figure 1A**). **Figure 1B** shows the UV-vis absorption spectra in solution of the synthesized AuNCs. The main features of spectra remain unchanged by post-covalent peptide coupling of PEG_{5000}-NH_2. However, the fluorescence intensity is strongly enhanced for PEGylated AuNCs as compared to unmodified AuSG nanoclusters, in particular for Au_{15}NCs. This enhancement may be caused by the reduced solvent accessibility as well as "rigidification" of the ligand shell upon addition of PEG on the surface of AuNCs (Bertorelle et al., 2018; Pyo et al., 2015). The average hydrodynamic diameter of the resulting AuSG nanoclusters and PEGylated AuSG nanoclusters was measured by time-resolved fluorescence anisotropy techniques, which are accurate sizing techniques for fluorescent NCs (Kang and Zhu, 2019; Soleilhac et al., 2017a, 2017b, 2018). An increase of ~3 nm in the size of PEGylated $Au_{15}SG_{13}$ (Au_{15}PEG) was observed and can be contributed to the extended hydration layer thickness due to the polymer chain of PEG (**Table S1**).

2.3.2. Effect of gold nanoclusters on glioblastoma cell viability

The physiological responses of living human glioblastoma cells to the AuNCs illustrated in **Figure 1** are currently unknown. To address this point, we examined how these AuNCs affect U251N glioblastoma cell viability, lysosomal properties and functions relevant to homeostatic and cytoskeletal biomarkers. We first assessed the viability of glioblastoma cells exposed to AuNCs. Quantitative data for concentration-dependent effects on cell viability were obtained by two complementary methods: by cell number counts (**Figure 2**) and measurements of metabolic activity (**Figure S1**).

For all AuNCs tested, cell numbers declined significantly at a final concentration of 100 μM (p<0.001). At 10 μM, only $Au_{15}SG_{13}$ diminished cell numbers; this effect was moderate but significant (reduction by ~25%). No significant changes were observed when AuNCs were present at 1 μM or lower concentrations (**Figure 2**). The impact of AuNCs was examined independently by the measurement of metabolic activity (MTT assay; **Figure S1**).

Together, both methods indicated that increasing AuNC concentrations reduced U251N cell number and metabolic activity. However, at or below 1 µM no or only minor changes were observed (**Figure 2, S1**).

In vivo AuNCs are excreted to a large extent via renal clearance (Du et al., 2017; Yu et al., 2019). Therefore, we assessed AuNC toxicity in HEK293 cells which are derived from the human renal epithelium (**Figure S1**). At ≤1 µM, $Au_{15}SG_{13}$ had only moderate impact; metabolic activities remained ≥76% of the vehicle control. Moreover, $Au_{25}SG_{18}$ had no significant effect on the metabolic activity at any concentration tested.

Taken together, results in **Figure 2** and **S1** are consistent with unrelated studies by us that examined the impact of AuNCs on non-transformed neural cells (Ji et al., 2019). In dissociated and 3D organotypic cultures, $Au_{15}SG_{13}$ or $Au_{25}SG_{18}$ were not deleterious to neurons at final concentrations <10µM.

2.3.3. Gold nanoclusters modulate the abundance of acidic compartments in glioblastoma cells

Many internalized nanoparticles accumulate in lysosomes, where they may alter organellar properties. A set of experiments was carried out to evaluate specific aspects of lysosome biology using different tools (**Figure 3**). The abundance of lysosomes was monitored with the membrane protein LAMP-2, a marker for lysosomes and late endosomes (Eskelinen et al., 2003). LysoTracker® Red DND-99 (in the following called Lysotracker Red) is an established fluorescent probe to identify and quantify acidic vesicles (Pierzyńska-Mach et al., 2014). We also assessed the subcellular lysosome location, because lysosomes close to the nucleus are characterized by a lower pH and enhanced activities of lysosomal enzymes (Bonifacino and Neefjes, 2017; Cabukusta and Neefjes, 2018; Johnson et al., 2016). LysoSensor™ DND-189 (here called Lysosensor Green) was used to examine the pH of acidic organelles (Lin et al., 2001). We confirmed that Lysotracker Red and Lysosensor Green are appropriate tools for our study; their fluorescence emission at pH 7.2 or pH 4.5 was not markedly altered by AuNCs (**Figure S2, S3**).

The abundance of LAMP-2 positive vesicles was not significantly changed after 4 hours (**Figure 3A**), but moderately reduced at 24 hours, both for $Au_{15}SG_{13}$ (91% of vehicle control) and Au_{15}PEG (72% of vehicle control). These results are consistent with the model that U251N cells can adapt to AuNCs without cell loss (**Figure 2**). Since LAMP-2 is located

predominantly in lysosomal membranes, the data suggest an overall reduction in lysosomal size and/or number.

LAMP-2 immunostaining does not inform on the functional state of lysosomes. This information was obtained with fluorescent probes for lysosomes and cathepsin B assessment (**Figure 3B-D** and below). At 4 hours, the intensity of Lysotracker Red diminished significantly when compared to vehicle controls (100%), declining to 40% for $Au_{15}SG_{13}$ and 51% for $Au_{15}PEG$. This decrease was transient only; after 24 hours Lysotracker Red fluorescence intensities were similar in cells treated with vehicle (100%), $Au_{15}SG_{13}$ (102%) or $Au_{15}PEG$ (88%).

The subcellular lysosome distribution is highly dynamic and linked to organellar pH (Johnson et al., 2016; Lawrence and Zoncu, 2019). Specifically, lysosomes located close to the nucleus are more acidic than their counterparts at the cell periphery. For both $Au_{15}SG_{13}$ and $Au_{15}PEG$ the perinuclear/peripheral ratio increased for Lysotracker Red at 4 hours (**Figure 3C**). Such a shift could be due to a rise in perinuclear fluorescence, loss in peripheral fluorescence, or a combination of both.

Remarkably, the distribution of Lysotracker Red-stained compartments was restored to vehicle controls after 24 hours. These data indicate that $Au_{15}SG_{13}$ and $Au_{15}PEG$ impaired the subcellular location of acidic vesicles only in the short term. Taken together, LAMP-2 staining, Lysotracker Red fluorescence intensity and distribution suggest adaptation of U251N cells within a 24-hour period of AuNC exposure.

The relocation of lysosomes towards the nucleus facilitates their acidification and enhances lysosome activities (Johnson et al., 2016). To better define the AuNC-dependent effects on lysosome distribution, we performed single-cell analyses and sorted results into bins (**Figure S4**). This comprehensive evaluation revealed that (i) lysosomal positioning is dynamic in U251N cells. Between 4 and 24 hours the perinuclear/peripheral ratio increased for all samples, including the vehicle control. (ii) After 24 hours, the distribution of lysosomes was similar for vehicle and AuNC-treated samples. However, treatment with 1 μM $Au_{15}SG_{13}$ or 1 μM $Au_{15}PEG$ increased the variability, with perinuclear/peripheral ratios >>4 for some of the cells. This extent of perinuclear accumulation was not observed for lysosomes in vehicle controls. Collectively, single-cell analyses indicate that AuNCs

generate cell populations that are more heterogeneous with respect to the characteristics of acidic vesicles.

Lysosensor Green has the highest pH sensitivity at its pK_a of 5.2. Lysosensor Green fluorescence emission is enhanced when the organellar pH approaches this value or the abundance of acidic compartments rises. Incubation with 1 µM $Au_{15}SG_{13}$ or 1 µM $Au_{15}PEG$ increased significantly the fluorescence intensities/area at 4 hours. Notably, these differences between vehicle controls and AuNC-treated cells persisted for 24 hours. This can be interpreted as an acidification of intracellular vesicles, increase in the number of acidic vesicles, or a combination of both.

Taken together, the different methods described in **Figure 3** and **S4** support the model that AuNCs altered the properties of intracellular acidic vesicles, in particular lysosomes. At 1 µM concentration, these changes were non-toxic and at least partially reversible.

Unlike other AuNCs examined in the current study, at 10 µM $Au_{15}SG_{13}$ reduced U251N cell numbers (**Figure 2**). To determine whether this was accompanied by augmented changes in lysosomal properties, Lysotracker Red fluorescence intensity, lysosome distribution, Lysosensor Green signals, and cathepsin B activity (see below) were assessed (**Figure S5**). Overall trends for 10 µM and 1 µM $Au_{15}SG_{13}$ were similar, but some of the effects were more pronounced with higher $Au_{15}SG_{13}$ concentrations. Our results suggest that lysosomal properties can be fine-tuned by selecting appropriate concentrations of $Au_{15}SG_{13}$.

The changes of lysosomal distribution described in **Figure 3** may suggest AuNC-dependent alterations in cellular pH homeostasis, in particular after a 4-hour incubation period. We addressed this point by monitoring possible effects on the cytoplasmic pH, using SNARF®-1 for ratiometric fluorescence measurements. Both 1 µM $Au_{15}SG_{13}$ and 1 µM $Au_{15}PEG$ caused a minor acidification of the cytoplasmic pH, but this amounted to less than 0.1 units (**Figure 4A**).

One of the mechanisms to stabilize the cytosolic pH relies on STAT3, a nuclear transcription factor that also associates with the cytoplasmic side of lysosomes (Liu et al., 2018). STAT3 interacts and stimulates v-ATPase activity. This interaction promotes lysosomal acidification and, at the same time, preserves a slightly basic cytosolic pH. In HeLa cells, approximately 5% of STAT3 co-purifies with lysosomes (Liu et al., 2018).

Figure 3D shows that Lysosensor Green signals increased after treatment with 1 µM $Au_{15}SG_{13}$ or 1 µM Au_{15}PEG for 4 and 24 hours. This may indicate an enhanced acidification of lysosomes. STAT3 is a possible candidate protein to reduce the luminal pH of lysosomes. Therefore, we investigated whether STAT3 co-localized with lysosomes, using LAMP-1 as a marker for the lysosomal membrane. In **Figure 4**, U251N cells were incubated with vehicle, 1 µM AuNCs or 20 µM chloroquine and fixed. Fixed cells were permeabilized with saponin to maintain the association of STAT3 with lysosomes. (Note that saponin does not efficiently permeabilize the nuclear envelope. Therefore, STAT3 was not detected in the nucleus.) Consistent with the Lysotracker Red distribution (**Figure 3B**) most of LAMP-1 was present in the vicinity of the nucleus (**Figure 4B**). By contrast, STAT3 distributed throughout the cytosol in a punctate fashion. This suggests the association of STAT3 with vesicles, which could be mediated through its interactions with various membrane proteins (e.g., EGFR) (Chatr-Aryamontri et al., 2015). However, co-localization with LAMP-1, which appears yellow in the overlay images, was rare under all conditions examined. Collectively, our results suggest that AuNCs did not induce marked changes to the stable association of STAT3 with lysosomes in U251N cells. This does not rule out a transient or weak interaction of STAT3 with lysosomal v-ATPase, which may have escaped detection.

2.3.4. $Au_{15}SG_{13}$ increases the formation of F-actin, with minor changes in tubulin abundance and nuclear size

The intracellular distribution of lysosomes is regulated by the actin cytoskeleton and microtubules; both filamentous systems control different aspects of lysosomal movement (Ba et al., 2018; Bonifacino and Neefjes, 2017; Cabukusta and Neefjes, 2018). In particular, the interaction with filamentous actin (F-actin) modulates constrained diffusion, whereas microtubules and associated motors promote the directed movement of lysosomes (Ba et al., 2018).

As described above, 10 µM $Au_{15}SG_{13}$ significantly altered cell numbers, metabolic activities (**Figure 2, S1**), and lysosomal characteristics (**Figure S5**). We selected this condition initially to examine cytoskeletal properties. After 24 hours, 10 µM $Au_{15}SG_{13}$ increased significantly the abundance of F-actin (**Figure 5**). Moreover, the formation of cortical F-actin at the cell periphery and of stress fibers was often enhanced. Adjacent to the nucleus cytoplasmic F-actin concentrations were elevated to 132% of the

vehicle control (not shown), but this was not significant. At the same time, the abundance of α-tubulin increased slightly upon $Au_{15}SG_{13}$ treatment. However, no marked changes in microtubule organization were detected.

The actin cytoskeleton regulates cell volume and size (F et al., 1996; Mohapatra et al., 2016), and components of the cytoskeleton regulate nuclear size (Cantwell and Nurse, 2019). While the size of U251N cells was not affected by 10 μM $Au_{15}SG_{13}$ after 24 hours (**Figure 5**), nuclei showed a minute increase in size.

Given the pronounced impact of 10 μM $Au_{15}SG_{13}$ on F-actin formation, we further examined U251N cells after incubation with 1 μM $Au_{15}SG_{13}$ or 1 μM Au_{15}PEG. A 24-hour treatment with 1 μM AuNCs increased the F-actin content, cell and nuclear size, but the changes were small (**Figure S6**). Collectively, these results indicate that AuNCs reorganize the cytoskeleton in a concentration-dependent manner. We propose that the AuNC-induced effects on the cytoskeleton modulate the dynamic subcellular distribution of lysosomes and thereby the activities of lysosomal enzymes, such as cathepsin B (see below).

2.3.5. $Au_{15}SG_{13}$ and Au_{15}PEG induce transient TFEB nuclear accumulation and increase cathepsin B activity

Results depicted in **Figure 3** show an AuNC-dependent rise in acidic cellular compartments and a transient repositioning of lysosomes. These findings are consistent with an increase in lysosomal biogenesis (Ba et al., 2018), which was examined in **Figure 6**. Transcription factor EB (TFEB) regulates the expression of genes essential for lysosomal biogenesis and enzymatic activities, including the protease cathepsin B (Bonifacino and Neefjes, 2017; Palmieri et al., 2011; Raben and Puertollano, 2016). TFEB also controls the positioning of lysosomes, stimulates their perinuclear accumulation, and enhances lysosomal exocytosis (Perera and Zoncu, 2016; Samie and Xu, 2014; Willett et al., 2017).

Under normal growth conditions, TFEB resides predominantly in the cytosol. To upregulate lysosome biogenesis, TFEB concentrates in nuclei where it promotes the expression of multiple target genes (Palmieri et al., 2011). As compared to vehicle-treated samples, $Au_{15}SG_{13}$ and Au_{15}PEG rapidly increased TFEB nuclear abundance (**Figure 6A**), albeit with somewhat different time courses. AuNC-induced nuclear accumulation of TFEB was reversible; it did not persist over a 24-hour period, when U251N cells were treated with 10 μM $Au_{15}SG_{13}$ (**Figure S7**). By contrast, Torin-1, a compound that concentrates TFEB in

nuclei (Vega-Rubin-de-Celis et al., 2017), led to sustained TFEB nuclear accumulation (**Figure S7**).

The AuNC-dependent rise in acidic vesicles (**Figure 3B-D**) and the transient nuclear accumulation of TFEB (**Figure 7A**) could lead to the upregulation of lysosomal biogenesis and lysosomal enzyme activities. To test this model, we measured the activity of cathepsin B, a protease located in lysosomes. Incubation of U251N cells with 1 μM $Au_{15}SG_{13}$ or 1 μM Au_{15}PEG increased significantly cathepsin B activity both at 4 and 24 hours. The AuNC-induced changes in cathepsin B activity (**Figure 6B**) correlated with enhanced Lysosensor Green fluorescence (**Figure 3D**). Moreover, the short-term rise in nuclear TFEB abundance is consistent with the increased perinuclear positioning of lysosomes after a 4-hour treatment with AuNCs (**Figure 3C**) (Willett et al., 2017).

Interestingly, despite the rise in TFEB abundance in the nucleus the signals for LAMP-2 were diminished (**Figure 3A**). One possible explanation for this phenomenon is lysosomal exocytosis, which reduces the intracellular concentrations of lysosomes; lysosomal exocytosis increases with the rise of TFEB abundance (see following section, (Perera and Zoncu, 2016; Samie and Xu, 2014). Taken together, our results support the idea that AuNCs modulate cellular homeostasis, in part by stimulating processes that rely on lysosomal enzyme activities.

2.3.6. $Au_{15}SG_{13}$ and Au_{15}PEG transiently relocate the transcription factor Nrf2 to nuclei

TFEB nuclear accumulation can be accompanied by the activation of Nuclear factor (erythroid-derived 2)-like 2 (Nrf2) (Kim et al., 2016). The transcription factor Nrf2 is key to cellular homeostasis, as it regulates the expression of genes involved in the oxidative stress response. Under normal growth conditions, Nrf2 resides in the cytosol. However, the transcription factor translocates to the nucleus when the abundance of reactive oxygen species (ROS) increases (Schmidlin et al., 2019).

Time-course experiments assessed the impact of AuNCs on Nrf2 location (**Figure 7**). Hydrogen peroxide (H_2O_2) provided a positive control; the oxidant activates Nrf2-dependent responses (Covas et al., 2013). $Au_{15}SG_{13}$ and Au_{15}PEG elevated Nrf2 levels in the nucleus, especially in nucleoli. This nuclear relocation was time-dependent, and Nrf2 abundance in the nucleus was significantly increased at 30 and 60 minutes (**Figure 7**).

As described for TFEB (**Figure 6A**), AuNC-dependent nuclear accumulation of Nrf2 was only transient. After 24 hours incubation with 10 μM $Au_{15}SG_{13}$ Nrf2 abundance in nuclei was slightly reduced (**Figure S8**), but remained high when cells were exposed to 300 μM H_2O_2. Results for Nrf2 subcellular location further support the model that $Au_{15}SG_{13}$ and Au_{15}PEG induce cellular stress, but cells recovered and adapted during a 24-hour incubation period. The changes in Nrf2 subcellular localization are consistent with the idea that AuNCs transiently elevated cellular ROS levels. While some AuNCs induce oxidative stress (Dong et al., 2015), the mechanisms through which ROS increase in Au_{15}PEG-treated cells are currently not known.

2.3.7. $Au_{15}SG_{13}$ nanoclusters reduce intracellular protein aggregates

Lysosomes are required to maintain protein homeostasis; they are essential to prevent the build-up of aggregated proteins (Xu and Ren, 2015). The Proteostat assay examined how AuNCs impinge on protein aggregation in the cytoplasm (**Figure 8**). After 24-hour treatment, protein aggregates were reduced by 1 μM $Au_{15}SG_{13}$ (78% of vehicle control), but increased with 1 μM Au_{15}PEG (**Figure 8A**).

To further characterize the impact of 1 μM AuNCs on protein aggregate formation, we challenged U251N cells with chloroquine, a compound that disrupts lysosomal functions (Mulcahy Levy et al., 2017). Notably, in the presence of 20 μM chloroquine, protein aggregates were diminished with $Au_{15}SG_{13}$, and significantly enhanced by Au_{15}PEG (**Figure 8B**).

These experiments revealed a striking difference between $Au_{15}SG_{13}$ and Au_{15}PEG, as it relates to proteostasis. $Au_{15}SG_{13}$ protected cells from the accumulation of protein aggregates, whereas Au_{15}PEG increased aggregate formation. It should be noted that the surface modifications, physicochemical properties, shapes, and hydrodynamic sizes differ profoundly for $Au_{15}SG_{13}$ and Au_{15}PEG (**Table S1**). All of these parameters determine the nanoparticle interactions with cells and intracellular organelles (Kodiha et al., 2015). For example, PEGylation modulates the composition of the nanoparticle corona (Partikel et al., 2019) and can enhance intracellular nanoparticle movement (Suh et al., 2007).

At present, the cellular mechanisms controlling the impact of $Au_{15}SG_{13}$ and Au_{15}PEG on protein aggregation have not been identified. Since $Au_{15}SG_{13}$ and Au_{15}PEG did not have opposing effects on lysosomal properties, we propose that AuNCs impact other pathways

that also regulate proteostasis. Possible candidates are alternative routes of protein degradation, changes in protein synthesis, oxidative stress, and protein folding (Klaips et al., 2018; Reichmann et al., 2018). Future experiments will have to address these questions.

Gold nanoparticles can increase cellular ROS concentrations and stimulate the formation of protein aggregates (Lopez-Chaves et al., 2018; Samhadaneh et al., 2019). Given that the incubation with 1 μM AuNCs for 24 hours diminished ($Au_{15}SG_{13}$) or increased (Au_{15}PEG) protein aggregation (**Figure 8A**), we examined whether this could be explained by differences in ROS abundance. Indeed, when evaluated with two independent assays, we observed a slight ROS reduction for $Au_{15}SG_{13}$, but an increase for Au_{15}PEG (**Figure S9**). This is consistent with the interpretation that AuNCs modulate protein aggregation at least in part through changes in cellular ROS concentrations.

2.3.8. Effects of AuNCs on stress granule formation

The experiments described above support the idea that AuNCs can produce cellular stress which impinges on lysosomes, stress-activated transcription factors, and potentially protein aggregation. This prompted us to investigate additional branches of the integrated stress response. Nrf2 and protein aggregate formation are tightly linked to oxidative stress, and the increase in oxidative stress is frequently associated with the formation of cytoplasmic stress granules (Reichmann et al., 2018; Schmidlin et al., 2019). One of the pathways to clear stress granules involves autophagy, a process that depends on lysosomal function (Alberti et al., 2017).

As described above, $Au_{15}SG_{13}$ altered lysosomal properties and diminished protein aggregation, both under normal conditions and in the presence of chloroquine. To define further the effects of $Au_{15}SG_{13}$ on oxidative stress responses, we examined whether $Au_{15}SG_{13}$ stimulates the assembly of cytoplasmic stress granules. Using HuR and importin-α1 as marker proteins, stress granule formation was not observed for different treatment times (**Figure S10**). The same results were obtained when U251N cells were exposed to $Au_{25}SG_{18}$.

Since $Au_{15}SG_{13}$ reduced protein aggregate formation induced by chloroquine (**Figure 8B**), we investigated whether these AuNCs also modulate the response to oxidative stress (**Figure S11**). To this end, sodium arsenite induced canonical stress granules in U251N cells

pretreated with vehicle, $Au_{15}SG_{13}$ or $Au_{25}SG_{18}$ (Sodium arsenite rather than H_2O_2 was used, because H_2O_2 may fail to induce canonical stress granules (Mahboubi and Stochaj, 2017)).

Quantitative single-cell analyses revealed that 10 µM $Au_{15}SG_{13}$ and 10 µM $Au_{25}SG_{18}$ reduced slightly the abundance of importin-α1 in unstressed cells and in arsenite-induced stress granules. This effect was more pronounced for $Au_{25}SG_{18}$ than $Au_{15}SG_{13}$. Similarly, AuNCs marginally reduced the abundance of G3BP1, a stress granule nucleating protein (Mahboubi and Stochaj, 2017), in nuclei and stress granules. Examination of individual stress granules did not uncover AuNC-dependent changes in granule size distribution (**Figure S1C**). Taken together, $Au_{15}SG_{13}$ and $Au_{25}SG_{18}$ did not provoke the formation of cytoplasmic stress granules. Moreover, both AuNCs had only minor impact on stress granule properties.

2.4. Conclusions

AuNCs are promising nanostructures for biomedical applications and have been used to image glioblastoma and other tumors in rodents (Cifuentes-Rius et al., 2017; Guével et al., 2018; Hu et al., 2014). Although AuNCs were reported to have low toxicity, in-depth studies to identify sub-lethal effects on cell physiology are sparse. We now show that AuNCs can modulate lysosomal parameters, specific aspects of the integrated stress response, and protein aggregation. Notably, these changes not only occur in the absence of overt cell killing, but they are also -to a large extent- reversible. Some AuNCs are rapidly cleared by renal excretion (Du et al., 2017) and could potentially damage the kidney. In human renal tubule cells, metabolic activities were somewhat reduced with $Au_{15}SG_{13,}$ but $Au_{25}SG_{18}$ caused no changes. Collectively, these findings indicate that the biological impact of AuNCs is determined by the number of gold atoms, size of the nanocluster, and properties of the surface modification. The results further emphasize possible cell type specific differences that are relevant to *in vivo* applications.

Our experiments focused on lysosomes and stress responses, because they are essential for overall cellular homeostasis and cell fate. Lysosomes are particularly relevant to tumor biology, as they are required to remove damaged proteins and organelles through autophagy. Autophagy in glioblastoma and other tumor cells can enhance tumor formation, whereas the inhibition of autophagy may trigger cancer cell death (reviewed in (Cordani and Somoza,

2019; Lahiri et al., 2019). Accordingly, lysosomes have been targeted successfully to induce cancer cell death and overcome treatment resistance (Cordani and Somoza, 2019).

The current study is unique, as it conducts in-depth analyses of the cellular responses induced by AuNCs. In particular, we provide -for the first time- detailed information on how AuNCs modulate the properties of lysosomes. We uncovered homeostatic perturbations caused by AuNCs in glioblastoma cells and biological processes that are linked to lysosome performance. The internalization and the ensuing involvement of lysosomes represent the most plausible scenario for AuNCs. However, it should be noted that due to their ultra-small size the direct imaging of the single particles in cells has not been possible.

The simplified model in **Figure 9** depicts the cellular components that we identified as possible AuNC targets. These new insights provide a framework for further AuNC-based applications in nanooncology. This includes the safe use for the imaging of glioblastoma and other tumors. Our study also identified lysosomal homeostasis and proteostasis as potential targets for future AuNC-dependent cancer treatment.

2.5. Methods

Materials. Primary antibodies against the following antigens were purchased from the sources specified and used at the dilutions indicated: TFEB (Sigma-Aldrich, SAB4503154; diluted 1:500), LAMP1 (Abcam, ab24170; 1:1000). LAMP2 (Abcam, ab13524; 1:500), Nrf2 (Abcam, ab31163; 1:200), G3BP1 (BD Biosciences; 1:2000), HuR (Santa Cruz Biotechnology, sc-5261; 1:2000), importin-α1 (Santa Cruz Biotechnology, sc-6917; 1:500), α-tubulin (Santa Cruz Biotechnology, sc-5286; 1:500), STAT3 (Cell Signaling Technology, #9139; 1:1250). Secondary antibodies: AlexaFluor®647 anti-rabbit IgG (Life Technologies, A21244; 1:500) and AlexaFluor®647 anti-rat IgG (Life Technologies, A21247; 1:500), AlexaFluor®647 anti-mouse (Jackson ImmunoResearch, 715-605-150; 1:400), Cy3™-anti-rabbit (Jackson ImmunoResearch, 711-165-152; 1:250).

Synthesis of AuNCs. $Au_{15}SG_{13}$ was synthesized as reported (Russier-Antoine et al., 2014). $Au_{25}SG_{18}$ was synthesized as follows: 234 mg glutathione (GSH) was dissolved in 35ml methanol, 2 ml tributylamine and 2 ml triethylamine. Then 100mg $HAuCl_4 \bullet 3H_2O$ dissolved in 10ml of water was added. The solution was stirred 3 hours at 45°C and then solution cooled to room temperature. 50mg tetramethylammonium borohydride were added with vigorous stirring. After 1 hour, additional 25mg borohydride were added. The solution was stirred for 3

hours and then left overnight without agitation before purification. Precipitation of AuNCs was induced by adding 1ml of 10% NH_4OH and diethyl ether. Unwanted products were removed through cycles of dissolution/precipitation/ centrifugation. The final precipitate was dissolved in a minimum of H_2O/NH_4OH and then precipitated with MeOH. After centrifugation, the powder was dissolved in 10 ml water. Then 2ml of glacial acetic acid was added, the solution was left undisturbed for 1 hour and then centrifuged (5 min at 10 000 rpm). The supernatant was collected and precipitated with MeOH. An additional cycle of dissolution/precipitation with H_2O/NH_4OH and acetic acid was performed, and the powder dried under vacuum over P_2O_5.

PEGylation of AuNCs. PEG_{5000}-NH_2 was grafted to the carboxylic acid of GSH by peptide coupling. Briefly, 25 mg AuNCs, 600 mg PEG_{5000}-NH_2 and 100 mg EDC•HCl (*N*-ethyl-*N*′-(3-(dimethylamino)propyl)carbodiimide hydrochloride) were dissolved in 5 ml water. The pH was adjusted to 7 with 1M NaOH, and the solution was stirred 24h at room temperature. Excess reagents were removed by dialysis, using a membrane with 10kDa cut-off (Sartorius).

Cell culture. Human U251N GBM cells (American Type Culture Collection; Rockville, MD, USA) were cultured in Dulbecco's Modified Eagle Medium (DMEM; Life Technologies Inc. Burlington, ON, Canada) with the presence of 5% (v/v) fetal bovine serum (FBS; Gibco; Penrose, Auckland, New Zealand), supplemented with 1% penicillin-streptomycin (Pen/Strep, Gibco), unless indicated otherwise. Cells were incubated at 37°C with 5% CO_2 and 95% relative humidity. For treatments with AuNCs or pharmacological agents control samples were incubated in the presence of the vehicle. “Vehicle” refers to the buffer or solvent used to disperse AuNCs or dissolve compounds. The volume of vehicle in the control was identical to the volume of dispersed AuNCs or dissolved agent. The incubation with vehicle, dispersed AuNCs or dissolved agents was always performed in growth medium.

Evaluation of cell numbers and cell metabolic activity. Cells were seeded in 96-well cell plates (Costar, Corning, New York, USA) at a density of 5,000 cells/well in serum-supplemented medium (DMEM, 5% FBS, 1% Pen/Strep). After 24 hours, cells were treated for 72 hours with $Au_{15}SG_{13}$, Au_{15}PEG, $Au_{25}SG_{18}$ and Au_{25}PEG at different final concentrations (1 nM, 100 nM, 1 µM, 10 µM, 100 µM). Following 72-hour treatments, cells were fixed in 4% paraformaldehyde (PFA; BDH, Toronto, ON, Canada) for 10 minutes at room temperature. PFA was aspirated, and cells were stained with 10 µM Hoechst 33342 (Invitrogen, H1399, OR,

USA) for 10 minutes at room temperature. Cells were washed with phosphate-buffered saline (PBS) and imaged with a Leica DMI 4000B fluorescence microscope (Leica microsystems, Heidelberg, Germany). Micrographs were analyzed with ImageJ (Schindelin et al., 2012).

Metabolic activities of U251N or HEK293 cells were measured with 3-(4,5-dimethylthiazol-2-yl)-2,5-diphenyltetrazolium bromide (MTT). Cells treated with vehicle or AuNCs were incubated for 1 hour at 37°C with 0.5 mg/mL MTT (M2128, Sigma-Aldrich), diluted in DMEM. Following incubation, medium was aspirated and replaced with dimethyl sulfoxide to solubilize the formazan product. Colorimetric measurements at 595 nm were performed with a Biochrom EZ Read 2000 Microplate Reader (Biochrom, Cambridge, United Kingdom).

Fluorescence microscopy and immunocytochemistry. U251N cells were seeded at a density of 5,000 cells per 12 mm diameter coverslip. After 24 hours in 120 µL serum-supplemented DMEM (5% FBS, 1% Pen/Strep), medium was replaced with DMEM and cells were treated as indicated. Following treatment, medium was aspirated, and cells were incubated with 10 µM Hoechst 33342 for nuclear staining and a second fluorescent dye to detect lysosomes, and cathepsin B activity. Following incubation with dyes, cells were washed twice with Earle's Balanced Salt Solution (EBSS) and imaged with a Leica fluorescence microscope. Micrographs were analyzed with ImageJ. Alternatively, images were acquired with a Zeiss LSM780 confocal microscope, and images were evaluated with MetaXpress® analysis software (Molecular Devices, San Jose, CA, USA) as published by us (Mahboubi et al., 2013; Moujaber et al., 2019). For immunocytochemistry, treated cells were fixed in 4% paraformaldehyde at room temperature and permeabilized with 0.1% Triton X-100 (Sigma-Aldrich) in PBS for 10 minutes. Cells were blocked for 1 hour in 10% goat serum (Gibco). Incubation with primary antibodies was overnight at 4°C for 24 hours. Cells were washed three times for 5 minutes with PBS and incubated with secondary antibodies for 1 hour at room temperature. Nuclei were detected with 10 µM Hoechst 33342 and F-actin with 1:50 Alexa Fluor® 488 Phalloidin (Invitrogen). Coverslips were mounted in Aqua-PolyMount (PolySciences, Warrington, PA, USA) or Vectashield® (Vector Laboratories, Burlingame, CA, USA).

The detection of STAT3 was essentially as described (Liu et al., 2018); all steps were carried out at room temperature. In brief, upon incubation with vehicle, AuNCs or chloroquine,

cells were rinsed twice with PBS and fixed for 15 min in 4% paraformaldehyde. Fixed cells were permeabilized 5 minutes with 0.1% saponin (Sigma-Aldrich) in PBS containing 2 mg/ml BSA and 1 mM NaN_3. Samples were blocked 1 hour in PBS/5% FBS/1 mM NaN_3 (blocking buffer). All subsequent steps were carried out in blocking buffer.

Staining of lysosomes with LysoTracker DND-99. Following treatment, growth medium was aspirated, and cells were incubated with 10 µm Hoechst 33342 and labeled with 50 nM LysoTracker® Red DND-99 (Invitrogen, Eugene, Oregon, USA) for 20 minutes at 37°C.

Evaluation of acidic organelles. LysoSensor™ DND-189 (Invitrogen) has a pK_a of 5.2; the compound is fluorescent when located in acidic vesicles, such as lysosomes. Following treatment, growth medium was aspirated, and cells were incubated with 10 µm Hoechst 33342 and labeled with 1 µM LysoSensor™ DND-189 for 20 minutes at 37°C.

Analysis of lysosome subcellular distribution. Nuclear boundaries were determined with Hoechst 33342. The perinuclear area was demarcated with ImageJ. It is the region within a 5 µm distance from the nuclear margin; the cellular region outside of this zone is defined as the peripheral area (Willett et al., 2017). Lysosome distribution was determined as the LysoTracker® DND-99 fluorescence in the perinuclear/LysoTracker® DND-99 fluorescence in the peripheral area.

Measurement of cytosolic pH in living cells. The cytosolic pH was determined with SNARF®-1 (5-(and-6)-Carboxy SNARF™-1, acetoxymethyl ester, acetate; C1272, ThermoFisher), which is suitable for ratiometric pH measurements. SNARF®-1 was excited at 488 nm and emissions were recorded at 580 nm and 640 nm, essentially as described (Lucien et al., 2014). For calibration, U251N cells were seeded in 96-well plates, containing 10,000 cells/well. After overnight growth, samples were incubated with 5 µM SNARF®-1 in serum-free/phenol-free DMEM (45 min, 37°C). Calibration was performed for different pH values (pH 5.5, 6.0, 6.5, 7.0, 7.1, 7.2, 7.3, 7.4, 7.5) in the presence of 10 µM nigericin (Sigma) (Lucien et al., 2014). Fluorescence intensities were measured with a SPARK10M microplate reader (excitation: 485 nm, bandwidth 20 nm; emission E_1: 635 nm, bandwidth 35 nm; and emission E_2: 580 nm, bandwidth 20 nm). The ratio E_1/E_2 for fluorescence emission was plotted as a function of pH, and non-linear regression was used for curve-fitting. The cytosolic pH values of U251N cells were extrapolated from the calibration curve.

Measurement of cathepsin B activity. Dequenching of the fluorogenic substrate MR-$(RR)_2$ (Magic Red, ImmunoChemistry Technologies; Bloomington, MN, USA) determined the activity of the lysosomal protease cathepsin B. Following treatment, growth medium was aspirated, and cells were incubated with 10 µm Hoechst 33342 and Magic Red (1:260) for 30 minutes at 37°C.

Proteostat assay. The assay followed the manufacturer's protocol with minor modifications. Specifically, cells were incubated with the Proteostat® reagent (1:8000; ENZ51035; Enzo Life Sciences; Farmingdale, NY, USA) for 2 hours at room temperature. Nuclei were detected with 10 µM Hoechst 33342, and F-actin with 1:50 Alexa Fluor® 488 Phalloidin (Invitrogen).

*Measurement of cellular ROS with CellROX® Green and CM-H_2DCFDA.*U251N cells were incubated with 1 µM $Au_{15}SG_{13}$ or Au_{15}PEG for 24 hours in serum-free DMEM at 37°C; 2.5 µM CellROX® Green (ThermoFisher) was added during the last 30 minutes of the incubation period. Microscopic images were acquired, and pixel intensities were quantified per nuclear area as described by us (Kodiha M, Bednarz K, Maysinger D, Stochaj U., 2017).

ROS were also detected with CM-H_2DCFDA (ThermoFisher). U251N cells were incubated with 1 µM CM-H_2DCFDA in serum-free/phenol-free DMEM for 30 min at 37°C, washed once with PBS and treated with 1 µM $Au_{15}SG_{13}$ or Au_{15}PEG for 24 hours in serum-free/phenol-free DMEM. Cells were washed once with PBS and imaged live with a Leica microscope at 63X objective.

Measurements of cell size and stress granule parameters. Oxidative stress was induced by incubating U251N cells for 2 hours with growth medium containing 0.5 mM sodium arsenite. Control cells received water instead of sodium arsenite. Cell size measurements and the detection of cytoplasmic stress granules followed our published protocols (Mahboubi et al., 2013; Moujaber et al., 2019). The measurements were performed for 112 to149 cells and 1448 to 2422 stress granules for each condition.

Statistical analysis. Data are shown as average ± standard error of the mean (SEM). Student's t-test or One-Way ANOVA with Bonferroni correction was used to identify significant differences. A p value <0.05 was considered statistically significant. Significant changes are indicated in the figures as follows: *p<0.05, **p<0.01, ***p<0.001.

2.6. Acknowledgements

We thank Dr. A. Moquin (McGill University) for analyzing the direct effects of AuNCs on LysoTracker and LysoSensor dyes. This study was supported by grants from Natural Sciences and Engineering Research Council of Canada (DM and US) and the European Regional Development Fund (AR).

2.7. References

Alberti, S., Mateju, D., Mediani, L., and Carra, S. (2017). Granulostasis: Protein Quality Control of RNP Granules. Front. Mol. Neurosci. *10*.

Anderson, P., Kedersha, N., and Ivanov, P. (2015). Stress granules, P-bodies and cancer. Biochim Biophys Acta *1849*, 861–870.

Ao, H., Feng, H., Zhao, M., Zhao, M., Chen, J., and Qian, Z. (2017). Redox-Triggered Bonding-Induced Emission of Thiol-Functionalized Gold Nanoclusters for Luminescence Turn-On Detection of Molecular Oxygen. ACS Sens *2*, 1692–1699.

Ba, Q., Raghavan, G., Kiselyov, K., and Yang, G. (2018). Whole-Cell Scale Dynamic Organization of Lysosomes Revealed by Spatial Statistical Analysis. Cell Rep *23*, 3591–3606.

Bertorelle, F., Moulin, C., Soleilhac, A., Comby-Zerbino, C., Dugourd, P., Russier-Antoine, I., Brevet, P.-F., and Antoine, R. (2018). Bulky Counterions: Enhancing the Two-Photon Excited Fluorescence of Gold Nanoclusters. Chemphyschem *19*, 165–168.

Bonifacino, J.S., and Neefjes, J. (2017). Moving and positioning the endolysosomal system. Curr. Opin. Cell Biol. *47*, 1–8.

Cabukusta, B., and Neefjes, J. (2018). Mechanisms of lysosomal positioning and movement. Traffic *19*, 761–769.

Cantwell, H., and Nurse, P. (2019). A systematic genetic screen identifies essential factors involved in nuclear size control. PLOS Genetics *15*, e1007929.

Chatr-Aryamontri, A., Breitkreutz, B.-J., Oughtred, R., Boucher, L., Heinicke, S., Chen, D., Stark, C., Breitkreutz, A., Kolas, N., O'Donnell, L., et al. (2015). The BioGRID interaction database: 2015 update. Nucleic Acids Res. *43*, D470-478.

Cifuentes-Rius, A., Ivask, A., Das, S., Penya-Auladell, N., Fabregas, L., Fletcher, N.L., Houston, Z.H., Thurecht, K.J., and Voelcker, N.H. (2017). Gold Nanocluster-Mediated Cellular Death under Electromagnetic Radiation. ACS Appl. Mater. Interfaces *9*, 41159–41167.

Cloer, E.W., Goldfarb, D., Schrank, T.P., Weissman, B.E., and Major, M.B. (2019). NRF2 Activation in Cancer: From DNA to Protein. Cancer Res. *79*, 889–898.

Cordani, M., and Somoza, Á. (2019). Targeting autophagy using metallic nanoparticles: a promising strategy for cancer treatment. Cell. Mol. Life Sci. *76*, 1215–1242.

Covas, G., Marinho, H.S., Cyrne, L., and Antunes, F. (2013). Activation of Nrf2 by H2O2: de novo synthesis versus nuclear translocation. Meth. Enzymol. *528*, 157–171.

Crawford, S.E., Hartmann, M.J., and Millstone, J.E. (2019). Surface Chemistry-Mediated Near-Infrared Emission of Small Coinage Metal Nanoparticles. Acc. Chem. Res. *52*, 695–703.

Dong, L., Li, M., Zhang, S., Li, J., Shen, G., Tu, Y., Zhu, J., and Tao, J. (2015). Cytotoxicity of BSA-Stabilized Gold Nanoclusters: In Vitro and In Vivo Study. Small *11*, 2571–2581.

Du, B., Jiang, X., Das, A., Zhou, Q., Yu, M., Jin, R., and Zheng, J. (2017). Glomerular barrier behaves as an atomically precise bandpass filter in a sub-nanometre regime. Nat Nanotechnol *12*, 1096–1102.

Eskelinen, E.-L., Tanaka, Y., and Saftig, P. (2003). At the acidic edge: emerging functions for lysosomal membrane proteins. Trends Cell Biol. *13*, 137–145.

F, R., B, K., B, P., S, B., F, S., Cj, W., M, S., R, A., and Aa, N. (1996). The role of the cortical cytoskeleton: F-actin crosslinking proteins protect against osmotic stress, ensure cell size, cell shape and motility, and contribute to phagocytosis and development. J Cell Sci *109 (Pt 11)*, 2679–2691.

Guével, X.L., Henry, M., Motto-Ros, V., Longo, E., Montañez, M.I., Pelascini, F., Rochefoucauld, O. de L., Zeitoun, P., Coll, J.-L., Josserand, V., et al. (2018). Elemental and optical imaging evaluation of zwitterionic gold nanoclusters in glioblastoma mouse models. Nanoscale *10*, 18657–18664.

Hu, H., Huang, P., Weiss, O.J., Yan, X., Yue, X., Zhang, M.G., Tang, Y., Nie, L., Ma, Y., Niu, G., et al. (2014). PET and NIR optical imaging using self-illuminating (64)Cu-doped chelator-free gold nanoclusters. Biomaterials *35*, 9868–9876.

Ji, J., Moquin, A., Bertorelle, F., Ky Chang, P., Antoine, R., Luo, J., McKinney, R.A., and Maysinger, D. (2019). Organotypic and primary neural cultures as models to assess effects of different gold nanostructures on glia and neurons. Nanotoxicology *13*, 285–304.

Jin, R., Zeng, C., Zhou, M., and Chen, Y. (2016). Atomically Precise Colloidal Metal Nanoclusters and Nanoparticles: Fundamentals and Opportunities. Chem. Rev. *116*, 10346–10413.

Johnson, D.E., Ostrowski, P., Jaumouillé, V., and Grinstein, S. (2016). The position of lysosomes within the cell determines their luminal pH. J Cell Biol *212*, 677–692.

Kang, X., and Zhu, M. (2019). Tailoring the photoluminescence of atomically precise nanoclusters. Chem. Soc. Rev. *48*, 2422–2457.

Kang, X., Chong, H., and Zhu, M. (2018). Au25(SR)18: the captain of the great nanocluster ship. Nanoscale *10*, 10758–10834.

Kim, S., Choi, K.J., Cho, S.-J., Yun, S.-M., Jeon, J.-P., Koh, Y.H., Song, J., Johnson, G.V.W., and Jo, C. (2016). Fisetin stimulates autophagic degradation of phosphorylated tau via the activation of TFEB and Nrf2 transcription factors. Sci Rep *6*.

Klaips, C.L., Jayaraj, G.G., and Hartl, F.U. (2018). Pathways of cellular proteostasis in aging and disease. J Cell Biol *217*, 51–63.

Kodiha, M., Wang, Y.M., Hutter, E., Maysinger, D., and Stochaj, U. (2015). Off to the organelles - killing cancer cells with targeted gold nanoparticles. Theranostics *5*, 357–370.

Kodiha, M., Mahboubi, H., Maysinger, D., and Stochaj, U. (2016). Gold Nanoparticles Impinge on Nucleoli and the Stress Response in MCF7 Breast Cancer Cells. Nanobiomedicine (Rij) *3*.

Kodiha M, Bednarz K, Maysinger D, Stochaj U. (2017). Microscopy and Quantitative Imaging: Novel Applications in Health Research. In Microscopy: Advances in Scientific Research and Education: Formatex Research Center, Mendez-Vilas A, ed. (Formatex Research Center), pp. 244–252.

Lahiri, V., Hawkins, W.D., and Klionsky, D.J. (2019). Watch what you (self-) eat: Autophagic mechanisms that modulate metabolism. Cell Metab *29*, 803–826.

Lawrence, R.E., and Zoncu, R. (2019). The lysosome as a cellular centre for signalling, metabolism and quality control. Nature Cell Biology *21*, 133–142.

Lin, H.J., Herman, P., Kang, J.S., and Lakowicz, J.R. (2001). Fluorescence lifetime characterization of novel low-pH probes. Anal. Biochem. *294*, 118–125.

Liu, B., Palmfeldt, J., Lin, L., Colaço, A., Clemmensen, K.K.B., Huang, J., Xu, F., Liu, X., Maeda, K., Luo, Y., et al. (2018). STAT3 associates with vacuolar H+-ATPase and regulates cytosolic and lysosomal pH. Cell Res *28*, 996–1012.

Liu, C.-P., Wu, T.-H., Lin, Y.-L., Liu, C.-Y., Wang, S., and Lin, S.-Y. (2016). Tailoring Enzyme-Like Activities of Gold Nanoclusters by Polymeric Tertiary Amines for Protecting Neurons Against Oxidative Stress. Small *12*, 4127–4135.

Lopez-Chaves, C., Soto-Alvaredo, J., Montes-Bayon, M., Bettmer, J., Llopis, J., and Sanchez-Gonzalez, C. (2018). Gold nanoparticles: Distribution, bioaccumulation and toxicity. In vitro and in vivo studies. Nanomedicine *14*, 1–12.

Lucien, F., Harper, K., Pelletier, P.-P., Volkov, L., and Dubois, C.M. (2014). Simultaneous pH measurement in endocytic and cytosolic compartments in living cells using confocal microscopy. J Vis Exp.

Mahboubi, H., and Stochaj, U. (2017). Cytoplasmic stress granules: Dynamic modulators of cell signaling and disease. Biochimica et Biophysica Acta (BBA) - Molecular Basis of Disease *1863*, 884–895.

Mahboubi, H., Kodiha, M., and Stochaj, U. (2013). Automated detection and quantification of granular cell compartments. Microsc. Microanal. *19*, 617–628.

Mohapatra, L., Goode, B.L., Jelenkovic, P., Phillips, R., and Kondev, J. (2016). Design Principles of Length Control of Cytoskeletal Structures. Annual Review of Biophysics *45*, 85–116.

Moujaber, O., Fishbein, F., Omran, N., Liang, Y., Colmegna, I., Presley, J.F., and Stochaj, U. (2019). Cellular senescence is associated with reorganization of the microtubule cytoskeleton. Cell. Mol. Life Sci. *76*, 1169–1183.

Mulcahy Levy, J.M., Towers, C.G., and Thorburn, A. (2017). Targeting Autophagy in Cancer. Nat Rev Cancer *17*, 528–542.

Nandi, S., Ghosh, S., and Bhattacharyya, K. (2018). Live Cell Microscopy: A Physical Chemistry Approach. J Phys Chem B *122*, 3023–3036.

Oyarzún, J.E., Lagos, J., Vázquez, M.C., Valls, C., De la Fuente, C., Yuseff, M.I., Alvarez, A.R., and Zanlungo, S. (2019). Lysosome motility and distribution: Relevance in health and disease. Biochimica et Biophysica Acta (BBA) - Molecular Basis of Disease *1865*, 1076–1087.

Palmieri, M., Impey, S., Kang, H., di Ronza, A., Pelz, C., Sardiello, M., and Ballabio, A. (2011). Characterization of the CLEAR network reveals an integrated control of cellular clearance pathways. Hum Mol Genet *20*, 3852–3866.

Partikel, K., Korte, R., Stein, N.C., Mulac, D., Herrmann, F.C., Humpf, H.-U., and Langer, K. (2019). Effect of nanoparticle size and PEGylation on the protein corona of PLGA nanoparticles. Eur J Pharm Biopharm *141*, 70–80.

Perera, R.M., and Zoncu, R. (2016). The Lysosome as a Regulatory Hub. Annu. Rev. Cell Dev. Biol. *32*, 223–253.

Pierzyńska-Mach, A., Janowski, P.A., and Dobrucki, J.W. (2014). Evaluation of acridine orange, LysoTracker Red, and quinacrine as fluorescent probes for long-term tracking of acidic vesicles. Cytometry A *85*, 729–737.

Protter, D.S.W., and Parker, R. (2016). Principles and Properties of Stress granules. Trends Cell Biol *26*, 668–679.

Pyo, K., Thanthirige, V.D., Kwak, K., Pandurangan, P., Ramakrishna, G., and Lee, D. (2015). Ultrabright Luminescence from Gold Nanoclusters: Rigidifying the Au(I)–Thiolate Shell. J. Am. Chem. Soc. *137*, 8244–8250.

Raben, N., and Puertollano, R. (2016). TFEB and TFE3: Linking Lysosomes to Cellular Adaptation to Stress. Annu. Rev. Cell Dev. Biol. *32*, 255–278.

Reichmann, D., Voth, W., and Jakob, U. (2018). Maintaining a Healthy Proteome during Oxidative Stress. Mol Cell *69*, 203–213.

Russier-Antoine, I., Bertorelle, F., Vojkovic, M., Rayane, D., Salmon, E., Jonin, C., Dugourd, P., Antoine, R., and Brevet, P.-F. (2014). Non-linear optical properties of gold quantum clusters. The smaller the better. Nanoscale *6*, 13572–13578.

Samhadaneh, D.M., Alqarni, K.A., Smart, A., Kuang, M., Moujaber, O., Maysinger, D., and Stochaj, U. (2019). Gold nanourchins induce cellular stress, impair proteostasis and damage RNA. Nanomedicine: Nanotechnology, Biology and Medicine *22*, 102083.

Samie, M.A., and Xu, H. (2014). Lysosomal exocytosis and lipid storage disorders. J. Lipid Res. *55*, 995–1009.

Schindelin, J., Arganda-Carreras, I., Frise, E., Kaynig, V., Longair, M., Pietzsch, T., Preibisch, S., Rueden, C., Saalfeld, S., Schmid, B., et al. (2012). Fiji: an open-source platform for biological-image analysis. Nat. Methods *9*, 676–682.

Schmidlin, C.J., Dodson, M.B., Madhavan, L., and Zhang, D.D. (2019). Redox regulation by NRF2 in aging and disease. Free Radic. Biol. Med. *134*, 702–707.

Settembre, C., and Ballabio, A. (2014). Lysosome: regulator of lipid degradation pathways. Trends Cell Biol *24*, 743–750.

Soleilhac, A., Bertorelle, F., Dugourd, P., Girod, M., and Antoine, R. (2017a). Monitoring methanol-induced protein unfolding by fluorescence anisotropy measurements of covalently labelled rhodamine probe. Eur. Phys. J. D *71*, 142.

Soleilhac, A., Bertorelle, F., Comby-Zerbino, C., Chirot, F., Calin, N., Dugourd, P., and Antoine, R. (2017b). Size Characterization of Glutathione-Protected Gold Nanoclusters in the Solid, Liquid and Gas Phases. J. Phys. Chem. C *121*, 27733–27740.

Soleilhac, A., Bertorelle, F., and Antoine, R. (2018). Sizing protein-templated gold nanoclusters by time resolved fluorescence anisotropy decay measurements. Spectrochim Acta A Mol Biomol Spectrosc *193*, 283–288.

Su, Y., Xue, T., Liu, Y., Qi, J., Jin, R., and Lin, Z. (2019). Luminescent metal nanoclusters for biomedical applications. Nano Res. *12*, 1251–1265.

Suh, J., Choy, K.-L., Lai, S.K., Suk, J.S., Tang, B.C., Prabhu, S., and Hanes, J. (2007). PEGylation of nanoparticles improves their cytoplasmic transport. Int J Nanomedicine *2*, 735–741.

Traboulsi, H., Guerrina, N., Iu, M., Maysinger, D., Ariya, P., and Baglole, C.J. (2017). Inhaled Pollutants: The Molecular Scene behind Respiratory and Systemic Diseases Associated with Ultrafine Particulate Matter. Int J Mol Sci *18*.

Umair, M., Javed, I., Rehman, M., Madni, A., Javeed, A., Ghafoor, A., and Ashraf, M. (2016). Nanotoxicity of Inert Materials: The Case of Gold, Silver and Iron. J Pharm Sci *19*, 161–180.

Vankayala, R., Kuo, C.-L., Nuthalapati, K., Chiang, C.-S., and Hwang, K.C. (2015). Cancer Therapy: Nucleus-Targeting Gold Nanoclusters for Simultaneous In Vivo Fluorescence Imaging, Gene Delivery, and NIR-Light Activated Photodynamic Therapy (Adv. Funct. Mater. 37/2015). Advanced Functional Materials *25*, 5933–5933.

Vega-Rubin-de-Celis, S., Peña-Llopis, S., Konda, M., and Brugarolas, J. (2017). Multistep regulation of TFEB by MTORC1. Autophagy *13*, 464–472.

Wang, J., Zhang, G., Li, Q., Jiang, H., Liu, C., Amatore, C., and Wang, X. (2013). In vivo self-bio-imaging of tumors through in situ biosynthesized fluorescent gold nanoclusters. Sci Rep *3*, 1157.

Willett, R., Martina, J.A., Zewe, J.P., Wills, R., Hammond, G.R.V., and Puertollano, R. (2017). TFEB regulates lysosomal positioning by modulating TMEM55B expression and JIP4 recruitment to lysosomes. Nature Communications *8*, 1580.

Xu, H., and Ren, D. (2015). Lysosomal Physiology. Annu Rev Physiol *77*, 57–80.

Yu, M., Xu, J., and Zheng, J. (2019). Renal Clearable Luminescent Gold Nanoparticles: From the Bench to the Clinic. Angew Chem Int Ed Engl *58*, 4112–4128.

Zeng, C., Chen, Y., Das, A., and Jin, R. (2015). Transformation Chemistry of Gold Nanoclusters: From One Stable Size to Another. J. Phys. Chem. Lett. *6*, 2976–2986.

Zheng, Y., Lai, L., Liu, W., Jiang, H., and Wang, X. (2017). Recent advances in biomedical applications of fluorescent gold nanoclusters. Adv Colloid Interface Sci *242*, 1–16.

2.8. Figures

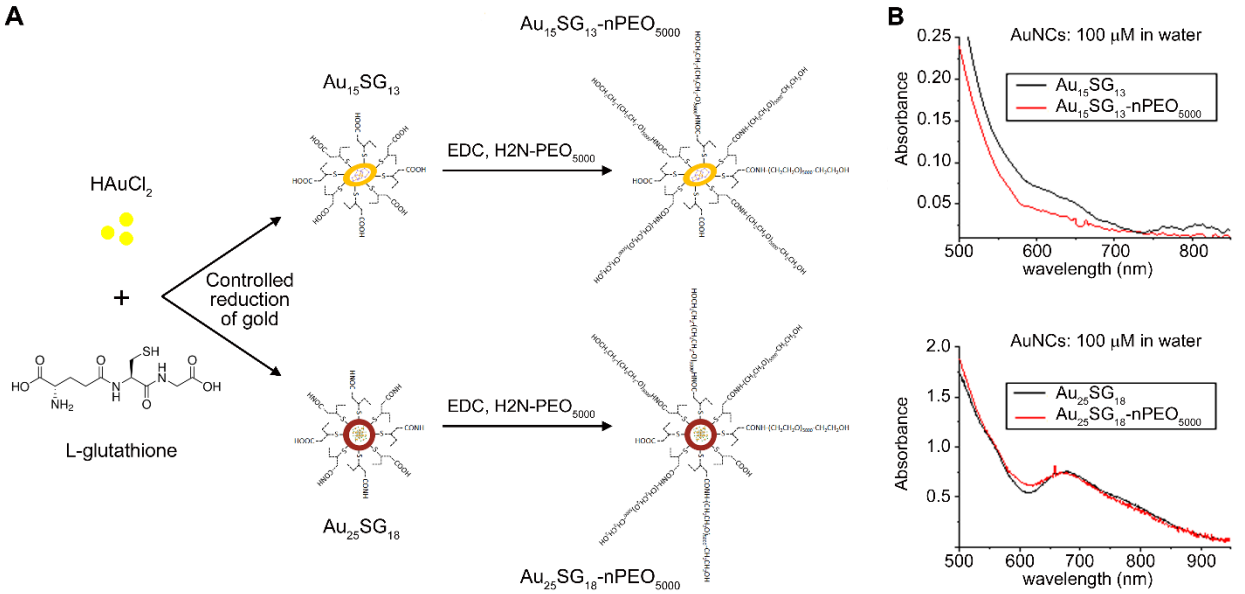

Figure 1. Synthesis and UV-vis absorption spectra of AuNCs. (A) Schematic representation of AuNC synthesis. AuNCs surfaces were modified with glutathione (SG) and PEG. Following the controlled reduction of gold with L-glutathione, AuNCs were PEGylated using the peptide coupling method described in the Methods section. (B) Absorbance spectra of Au_{15} and Au_{25} nanoclusters. Absorbance spectra for the different AuNCs indicated were obtained at a final concentration of 100 µM in water.

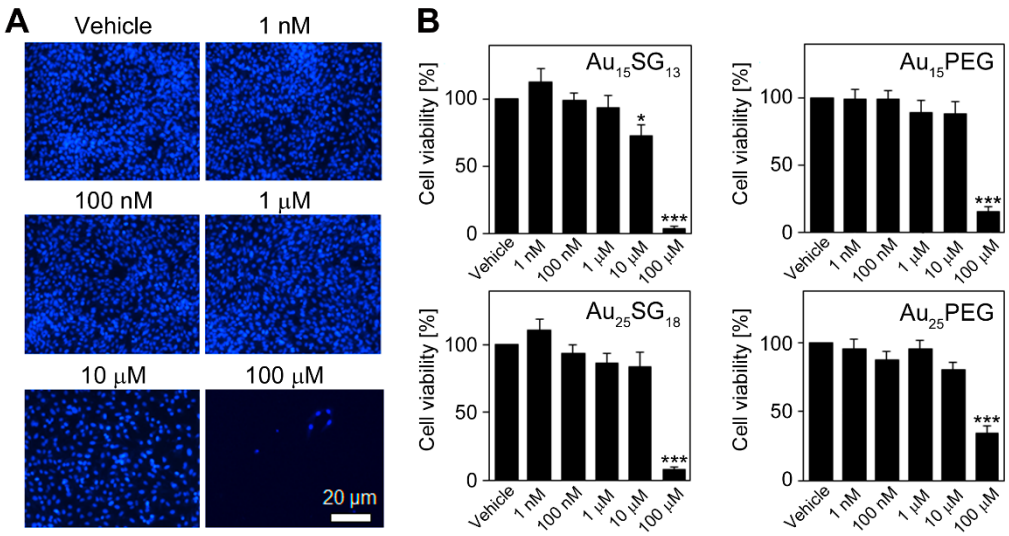

Figure 2. Impact of AuNCs on cell numbers. (A) U251N cells were treated with $Au_{15}SG_{13}$ for 72 hours with the concentrations indicated. Cells were identified with Hoechst 33342 staining of the nuclei as described in the Methods section. (B) Upon incubation with different AuNCs, cell numbers were quantified, and results were normalized to vehicle controls. Graphs depict the average ± SEM for three independent experiments. Significant differences between the vehicle control and AuNC-treated cells are marked. *, $p<0.05$; ***, $p<0.001$.

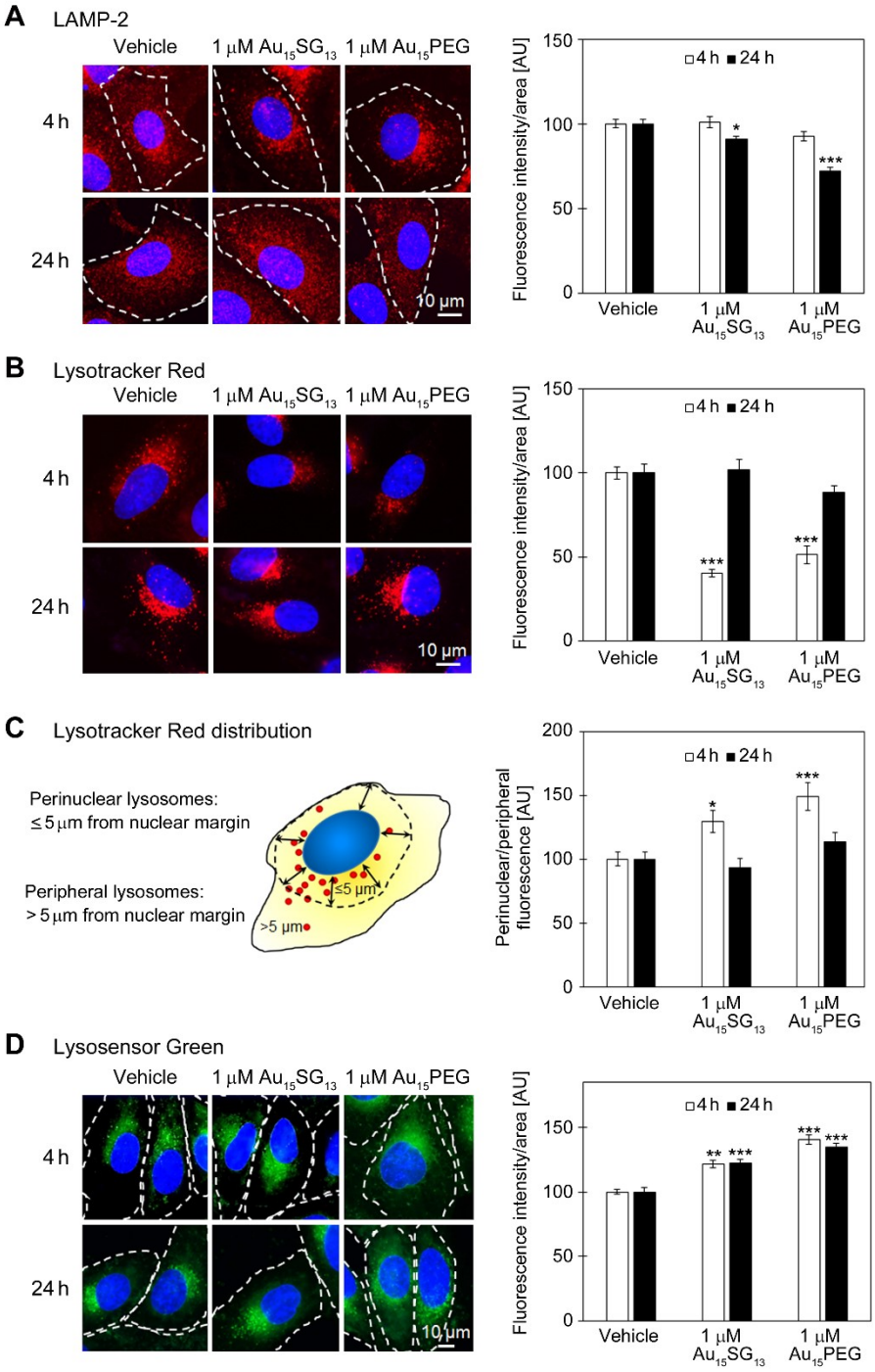

Figure 3. Evaluation of lysosomes in U251N cells. All graphs depict results normalized to the vehicle control; data are shown as average ± SEM; *p<0.05, **p<0.01, ***p<0.001; AU, arbitrary units. (A) Detection of LAMP-2. Cells were treated with 1 μM $Au_{15}SG_{13}$ or 1 μM $Au_{15}PEG$ for 4 or 24 hours. LAMP-2 was located by immunocytochemistry (red); nuclei were demarcated with Hoechst 33342 (blue). Fluorescence intensities/area were quantified for at least 97 cells per condition. (B) Lysosome staining with Lysotracker Red. Cells were incubated with vehicle, 1 μM $Au_{15}SG_{13}$ or 1 μM $Au_{15}PEG$ for 4 or 24 hours. The bars depict the average fluorescence intensity/area ± SEM; 52 to 134 cells were assessed per condition. (C) The distribution of

Lysotracker Red signals was determined for the 4- and 24-hour treatment shown in part B. The fluorescence intensities were quantified for a 5-μm area adjacent to the nuclear margin (perinuclear) and for peripheral cell regions. The ratio of perinuclear/peripheral signals was calculated for 44 to 58 cells for each condition. Results are depicted as average ± SEM. (D) Staining of U251N cells with Lysosensor Green. U251N cells treated with 1 μM $Au_{15}SG_{13}$ or 1 μM Au_{15}PEG for 4 or 24 hours were incubated with Lysosensor Green and imaged as described in the Methods section. Graphs depict average fluorescence intensities per area ± SEM; measurements were performed for a minimum of 81 cells per condition and at least two independent experiments.

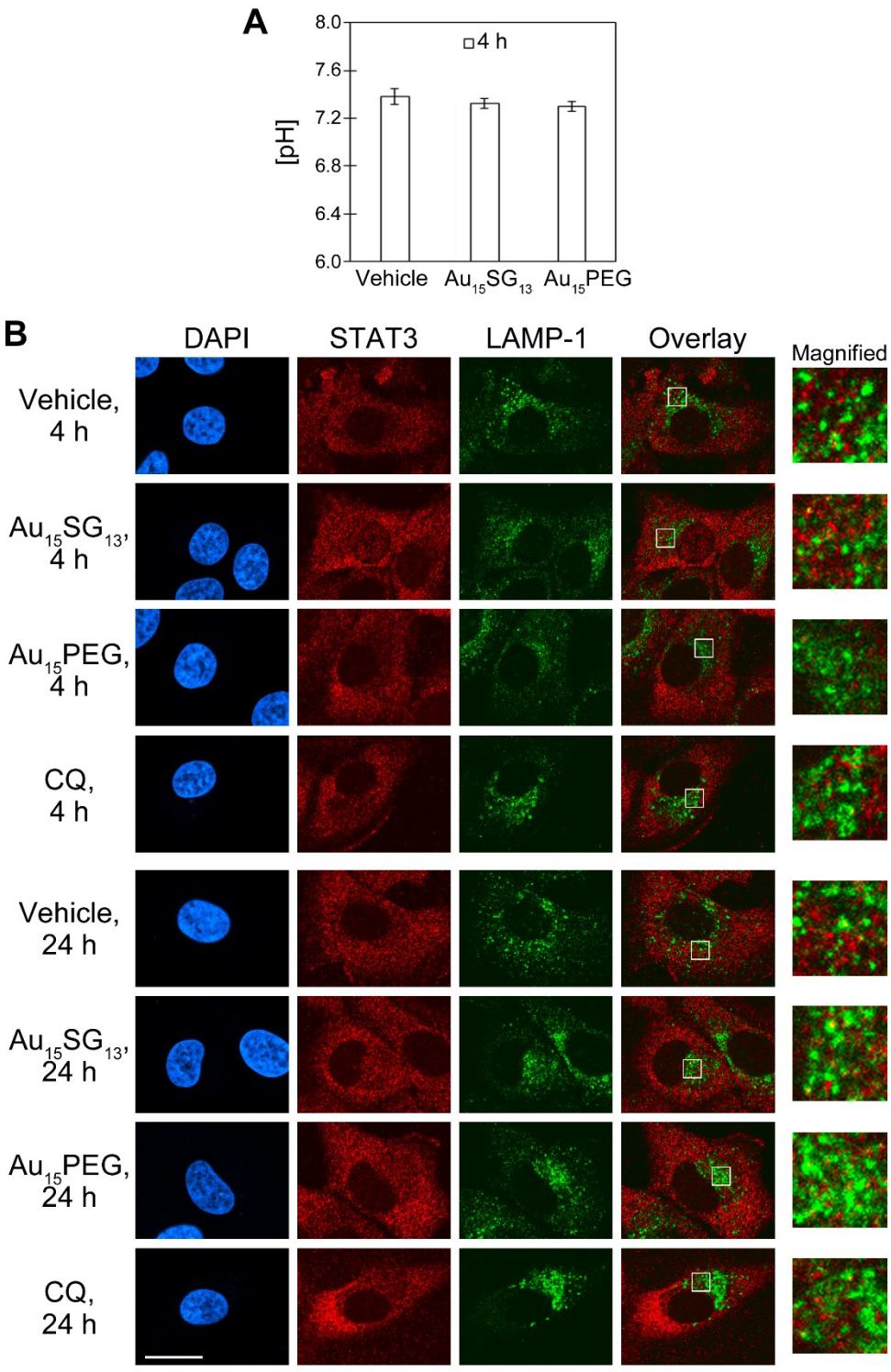

Figure 4. (A) Ratiometric measurement of cytoplasmic pH. U251N cells were treated for 4 hours with 1 μM $Au_{15}SG_{13}$ or 1 μM $Au_{15}PEG$ in serum-free medium. Following treatment, cells were incubated with 5 μM SNARF®-1 in serum-free DMEM for 45 min at 37°C. The pH values were determined by ratiometric fluorescence measurements and extrapolation from the calibration curve. The graph shows averages ± SEM for one experiment with triplicate samples. (B)

Subcellular distribution of STAT3 and LAMP-1. U251N cells were incubated with vehicle, 1 μM $Au_{15}SG_{13}$, 1 μM $Au_{15}PEG$ or 20 μM chloroquine (CQ) in serum-free medium for 4 hours or 24 hours as indicated. Cells were fixed and processed for immunocytochemistry as described in the Methods section. Scale bar is 20 μm. Selected regions of the overlay image were magnified 5-fold. Yellow color in the overlay images indicates co-localization of STAT3 and LAMP-1.

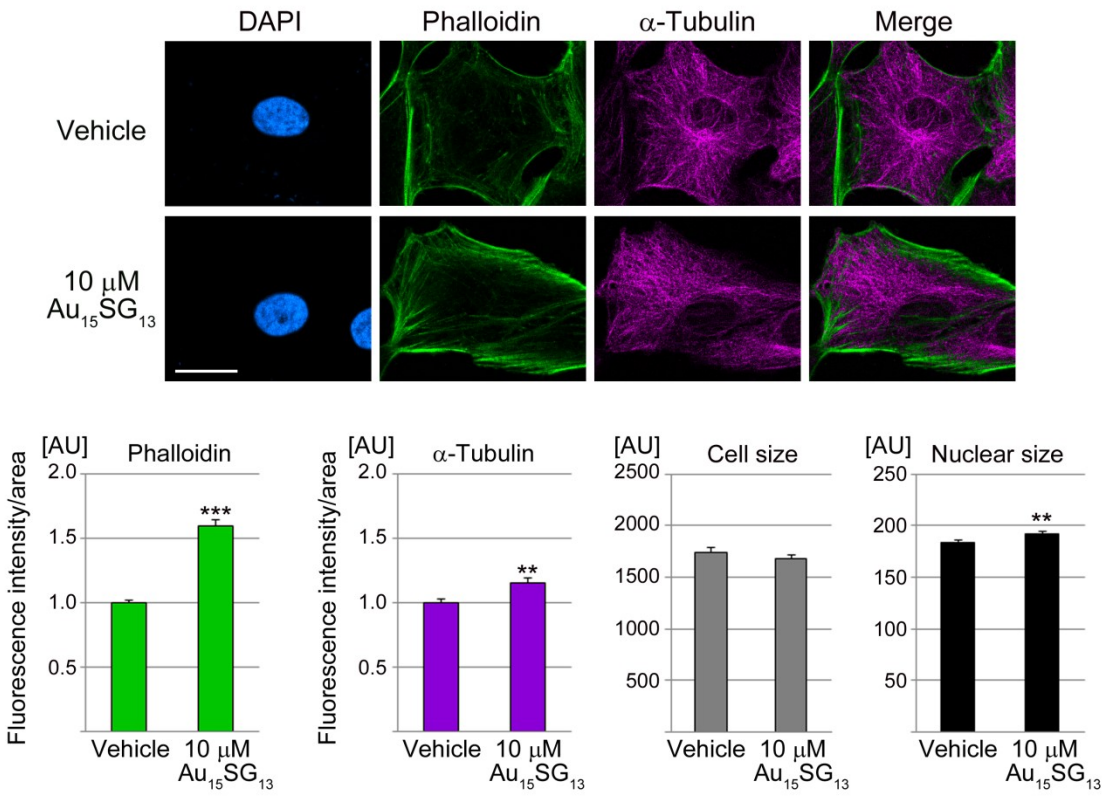

Figure 5. $Au_{15}SG_{13}$ increases the concentration of filamentous actin. U251N cells were incubated with 10 μM $Au_{15}SG_{13}$ for 24 hours, fixed and processed for immunohistochemistry to detect α-tubulin. F-actin was stained with Alexa Fluor® 488 phalloidin (Phalloidin); nuclei were demarcated with DAPI. Scale bar is 20 μm. Fluorescence intensities for phalloidin and α-tubulin were quantified for vehicle (105 cells) and $Au_{15}SG_{13}$ treated samples (126 cells). Graphs depict average + SEM for one representative experiment. Size was measured for 210 (vehicle) and 231 ($Au_{15}SG_{13}$) cells. Nuclear size was determined for 371 (vehicle) and 385 ($Au_{15}SG_{13}$) cells. AU, arbitrary units. Statistical evaluation was performed with Student's t-test; **, $p<0.01$; ***, $p<0.001$.

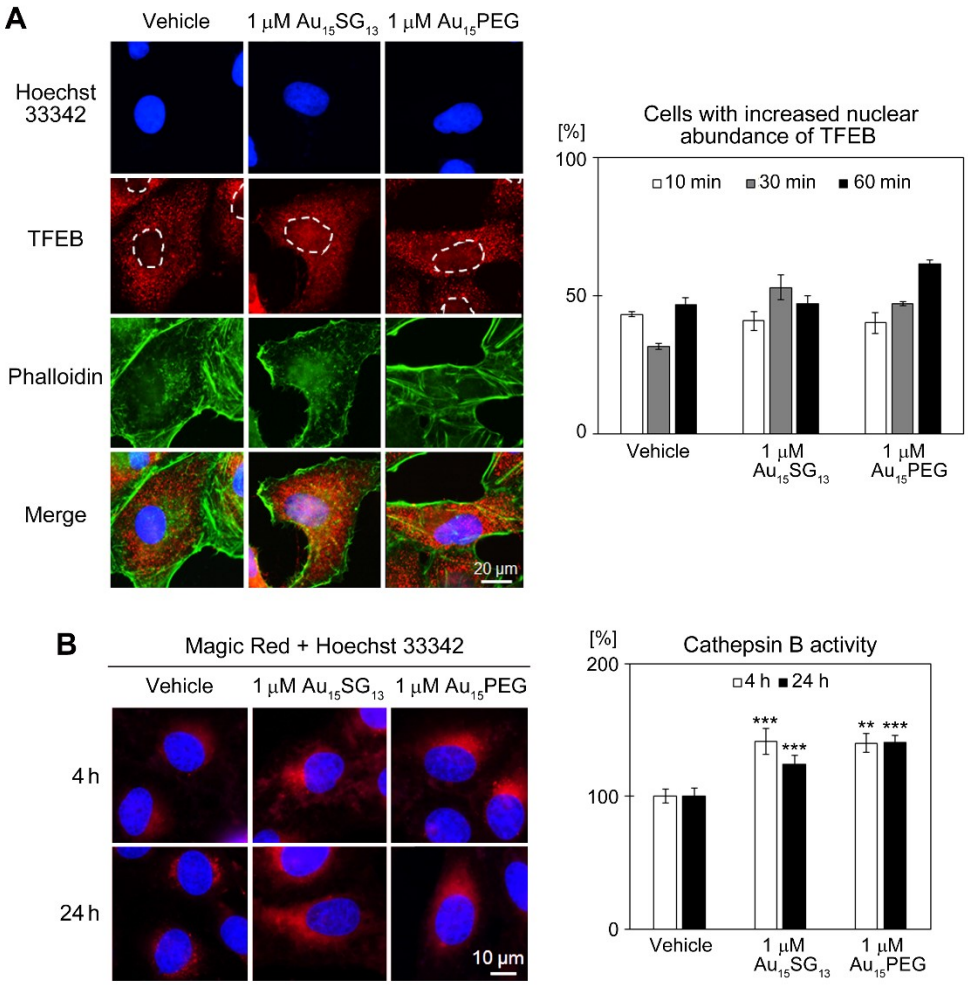

Figure 6. Effects of AuNCs on TFEB nucleocytoplasmic distribution and lysosomal activity. (A) U251N cells were treated with vehicle, 1 μM $Au_{15}SG_{13}$ or 1 μM $Au_{15}PEG$ in DMEM for the times indicated. Panels depict the results for cells incubated for 30 min with vehicle or AuNCs. TFEB was detected by immunocytochemistry, phalloidin stained F-actin, and Hoechst 33342 demarcated nuclei. Whole cell and nuclear fluorescence signals were quantified, and the nuclear/cytoplasmic ratio was calculated. The percentage of cells with elevated nuclear TFEB signals was determined for two independent experiments. For each condition and time point 80 to 101 cells were scored; bars show averages ± SEM. (B) AuNCs increase cathepsin B activity. Cathepsin B activity was measured in U251N cells treated with vehicle, 1 μM $Au_{15}SG_{13}$ or 1 μM $Au_{15}PEG$. Cells were incubated with Magic Red as described in the Methods section. Hoechst 33342 identified nuclei. For quantification, Magic Red fluorescence intensity was normalized to the vehicle control. Bars depict average ± SEM for at least two independent experiments. Between 34 and 92 cells were analyzed per condition and time point; **, $p<0.01$; ***, $p<0.001$.

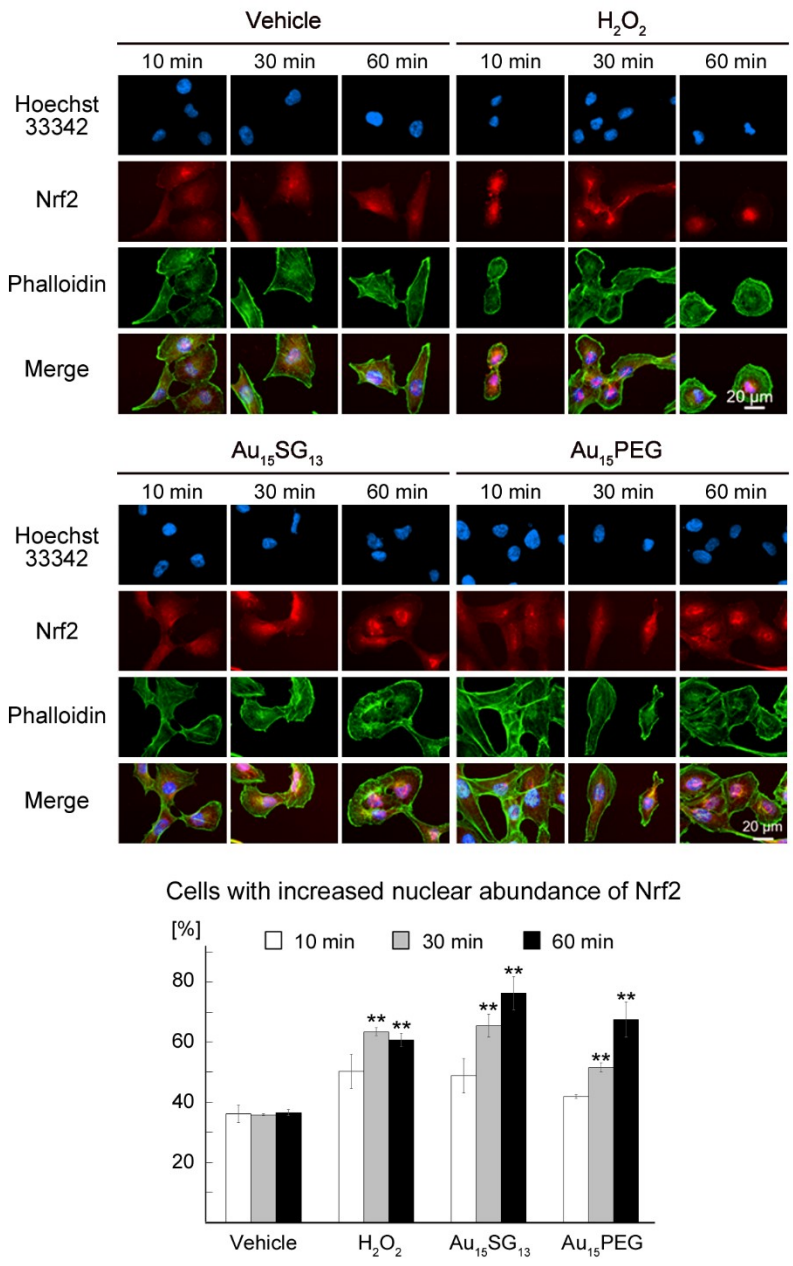

Figure 7. AuNCs promote the nuclear accumulation of Nrf2. U251N cells were treated for the times indicated with vehicle, 300 µM of H_2O_2, 10 µM of $Au_{15}SG_{13}$ or 10 µM $Au_{15}PEG$ for the times indicated. Cells were processed for immunocytochemistry with antibodies against Nrf2. Nuclei were detected with Hoechst 33342 and F-actin stained with phalloidin. After incubation for 10, 30 or 60 minutes, Nrf2 nuclear translocation was quantified by assessing Nrf2 fluorescence in the nucleus and cytosol. Three independent experiments were conducted and a total of 120 cells were analyzed. The graph shows average ± SEM; *, $p<0.05$; **, $p< 0.01$; ***, $p<0.001$.

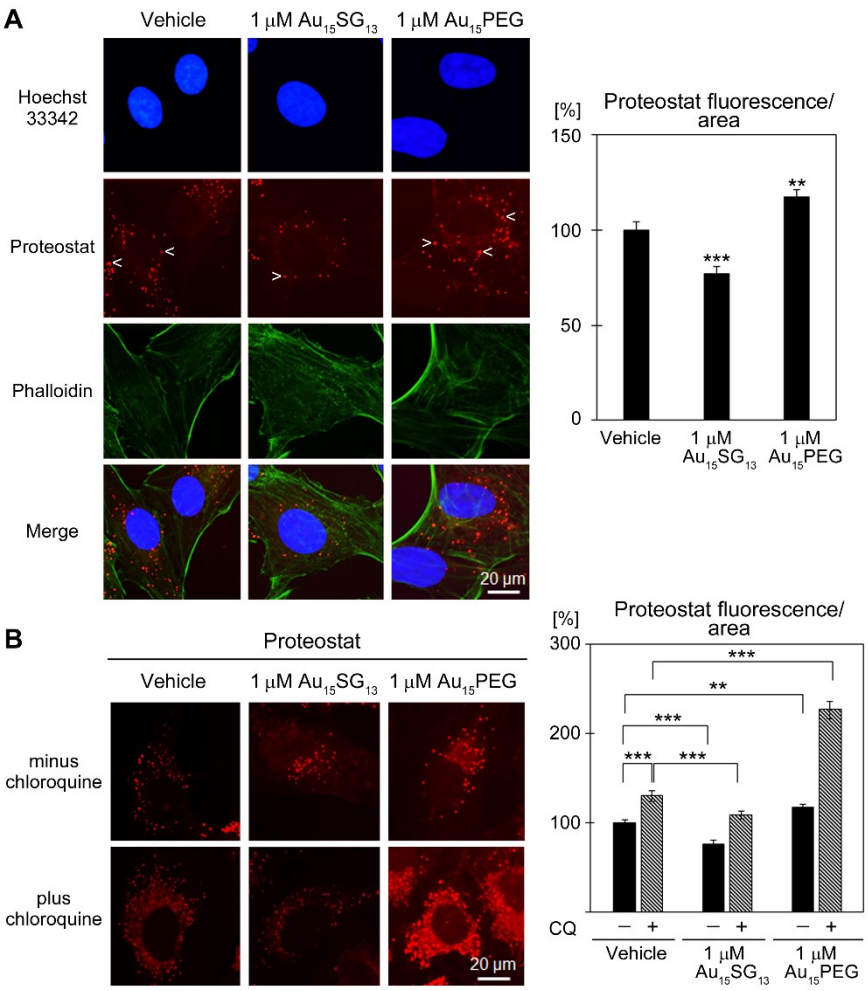

Figure 8. Effect of AuNCs on protein aggregation. (A) U251N cells treated with vehicle, 1 μM $Au_{15}SG_{13}$ or $Au_{15}PEG$ in DMEM for 24 hours were fixed and protein aggregation was evaluated with Proteostat. Some of the aggregates are marked with arrowheads. Fluorescence intensities/area were quantified for 97 to 105 cells for each condition. Results normalized to the vehicle control are shown as average ± SEM; ***, $p<0.001$. (B) U251N cells were incubated as described in part A. Chloroquine (CQ) was present during treatment as indicated. Proteostat signals were quantified for 88 to 105 cells per condition. Results were normalized to the vehicle control/minus chloroquine. Bars show average ± SEM; *$p<0.05$, **$p<0.01$, ***$p<0.001$.

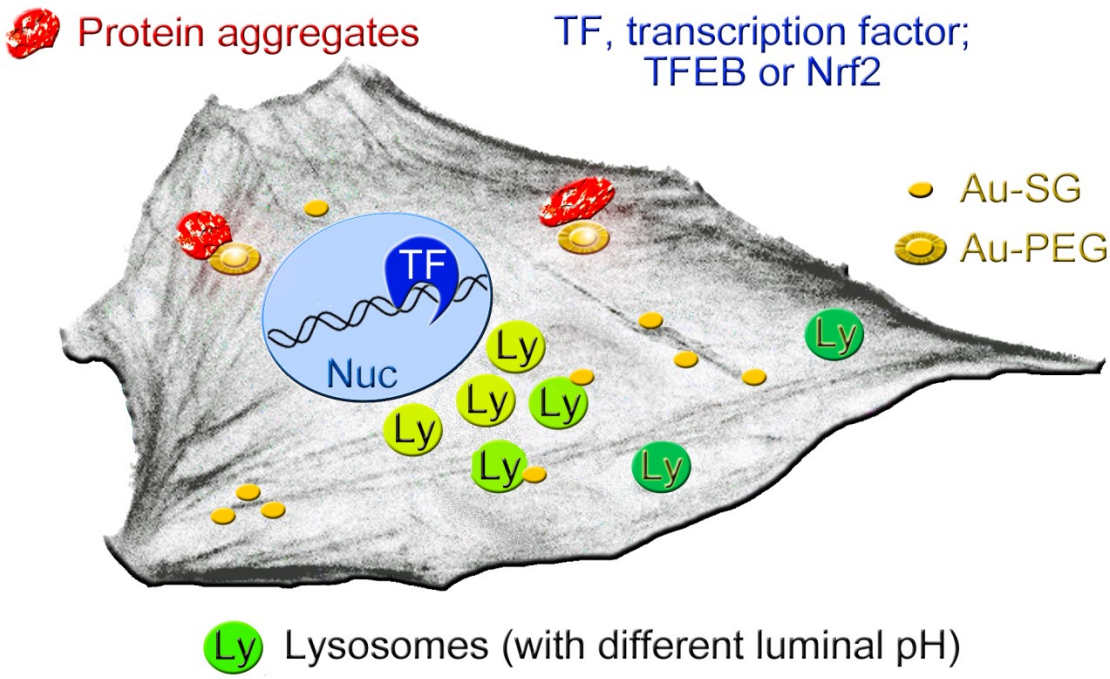

Figure 9. Simplified model depicting the cellular components that are affected, at least transiently, by AuNCs. AuNCs in this study were surface-modified with GSH (Au-SG) or PEGylated (Au-PEG). Lysosomes with more acidic pH (light green) are perinuclear, whereas peripheral lysosomes are less acidic (dark green). AuNCs stimulate the transient nuclear accumulation of transcription factors TFEB and Nrf2. PEGylated AuNCs may increase protein aggregation. See text for details.

2.9. Supplementary information

AuNC	Hydrodynamic diameter [nm]	Shape	Zeta [mV]
$Au_{15}SG_{13}$	2.9	asymmetric	-3.86
$Au_{15}SG_{13}$-$nPEO_{5000}$ ($Au_{15}PEG$)	6	spherical	-2.14
$Au_{25}SG_{18}$	3.3	spherical	-7.46
$Au_{25}SG_{18}$-$nPEO_{5000}$ ($Au_{25}PEG$)	4.5	spherical	-15.4

Table S1. Hydrodynamic size measurements and zeta potential for Au_{15}NCs and Au_{25}NCs. Hydrodynamic diameters were determined with time-resolved fluorescence anisotropy, according to our published protocols (Soleilhac et al., 2018). The zeta potential was measured with a Malvern Zetasizer Nano ZS; it was negative for all AuNCs studied here.

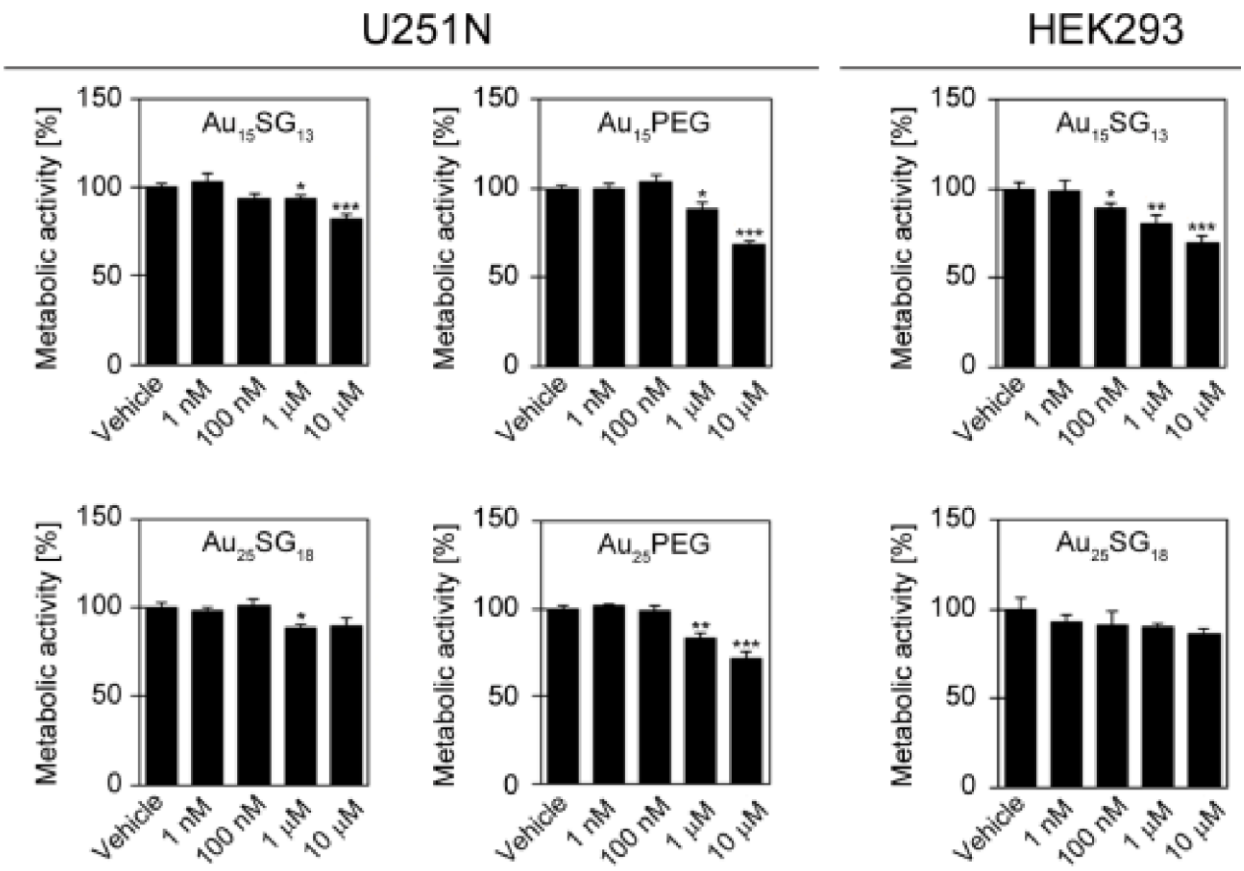

Figure S1. Effect of AuNCs on the metabolic activity of U251N and HEK293 cells. U251N cells incubated for 72 hours with AuNCs at the final concentrations indicated, using the methods described for Figure 2. The MTT assay assessed metabolic activities for at least two independent experiments, with triplicate samples for each data set. Results are shown as average + SEM; *, $p<0.05$; **, $p<0.01$; ***, $p<0.001$.

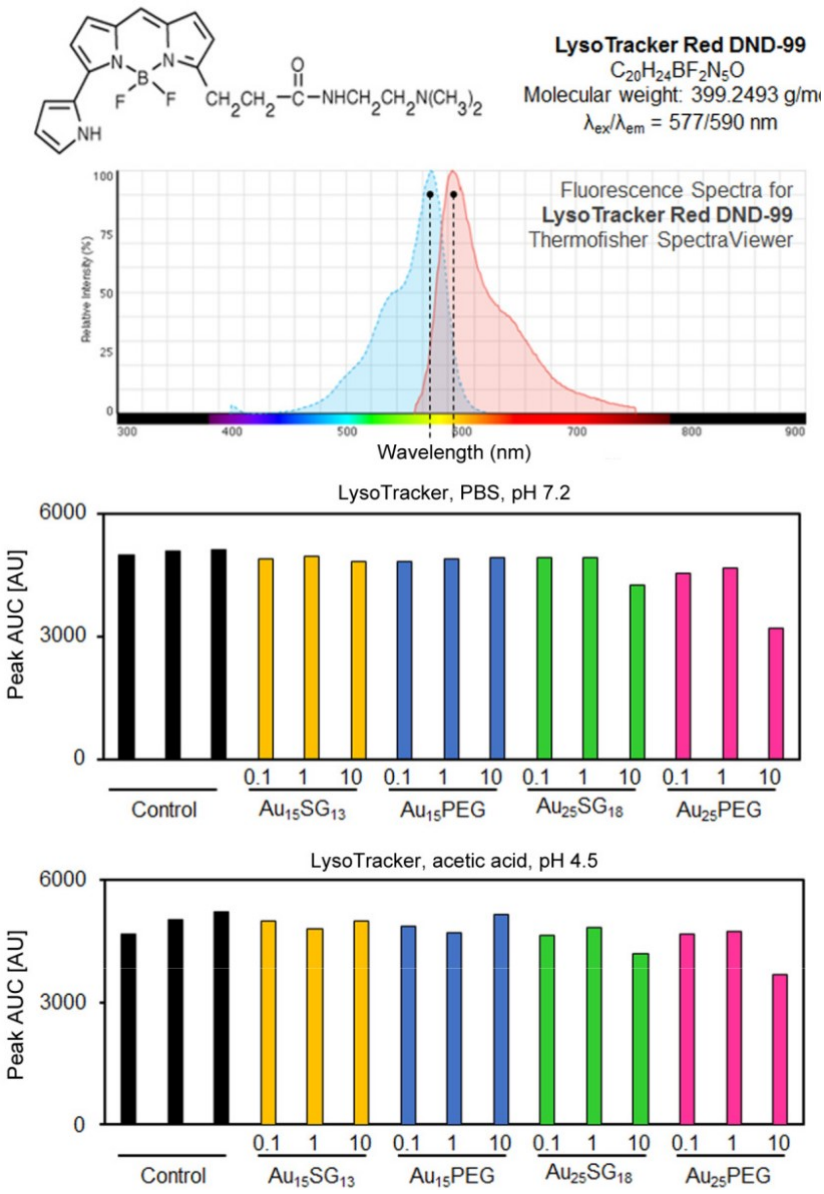

Figure S2. Effect of AuNCs on LysoTracker® Red DND-99 fluorescence. The fluorescence intensity of 100 nM LysoTracker Red in PBS (pH 7.2) or 100 mM sodium acetate buffer (pH 4.5) was measured in the presence of different AuNC concentrations as indicated. Excitation was at 576 nm, emission spectra were measured with a Cary Eclipse Fluorescence Spectrophotometer (Agilent Technologies) between 586 to 700 nm using an excitation slit of 10 nm and an emission slit of 10 nm with a photomultiplier tube voltage of 600 V. The area under the curve (AUC) was obtained by integrating the emission spectra between 586 and 700 nm. AuNCs did not quench LysoTracker Red DND-99 fluorescence at concentrations up to 10 µM. AU; arbitrary units.

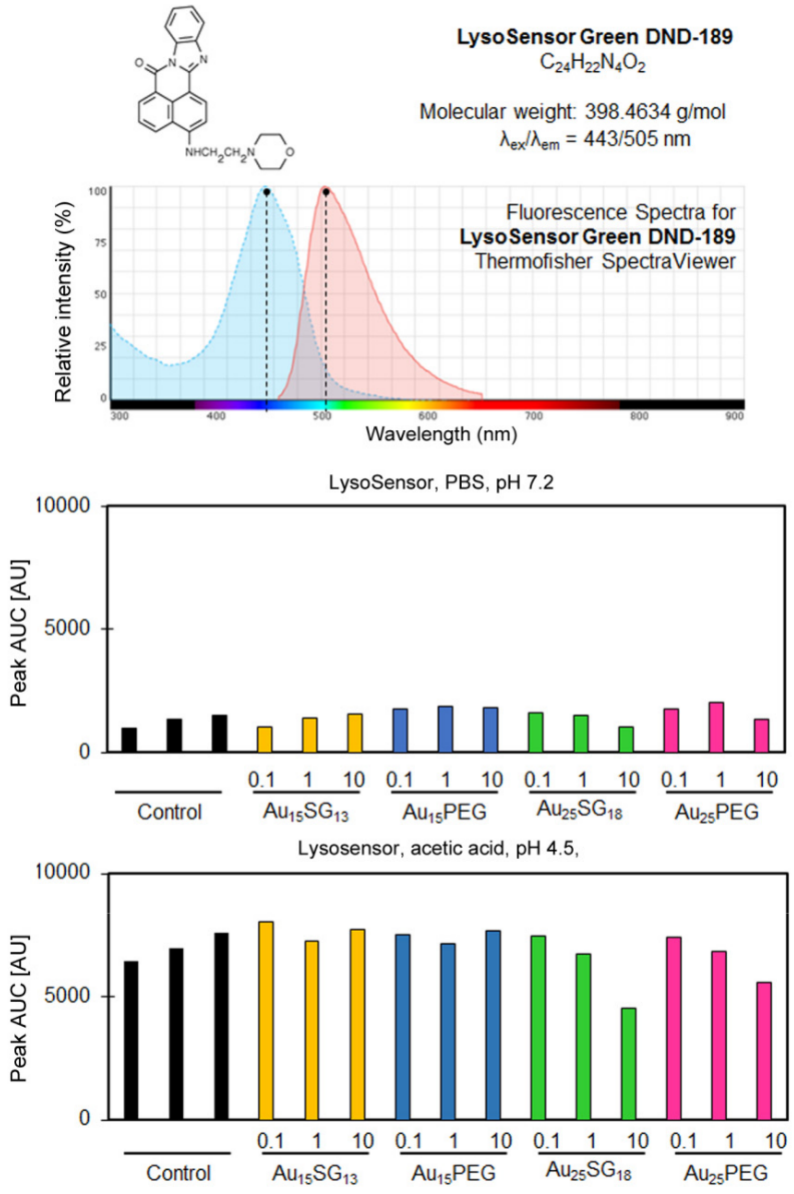

Figure S3. Effect of AuNCs on LysoSensor™ Green DND-189 fluorescence. The fluorescence intensity of 1 µM LysoSensor green in PBS (pH 7.2) or 100 mM acetate buffer (pH 4.5) was measured with a Cary Eclipse Fluorescence Spectrophotometer (Agilent Technologies) in the presence of different AuNC concentrations as indicated. Excitation was at 455 nm; emission was measured between 460 and 650 nm using excitation slit of 5 nm and an emission slit of 5 nm with a photomultiplier tube voltage of 600 V. The area under the curve (AUC) was obtained by integrating the emission spectra between 460 and 650 nm. AuNCs did not quench LysoSensor fluorescence at AuNC concentrations up to 10 µM. AU; arbitrary units.

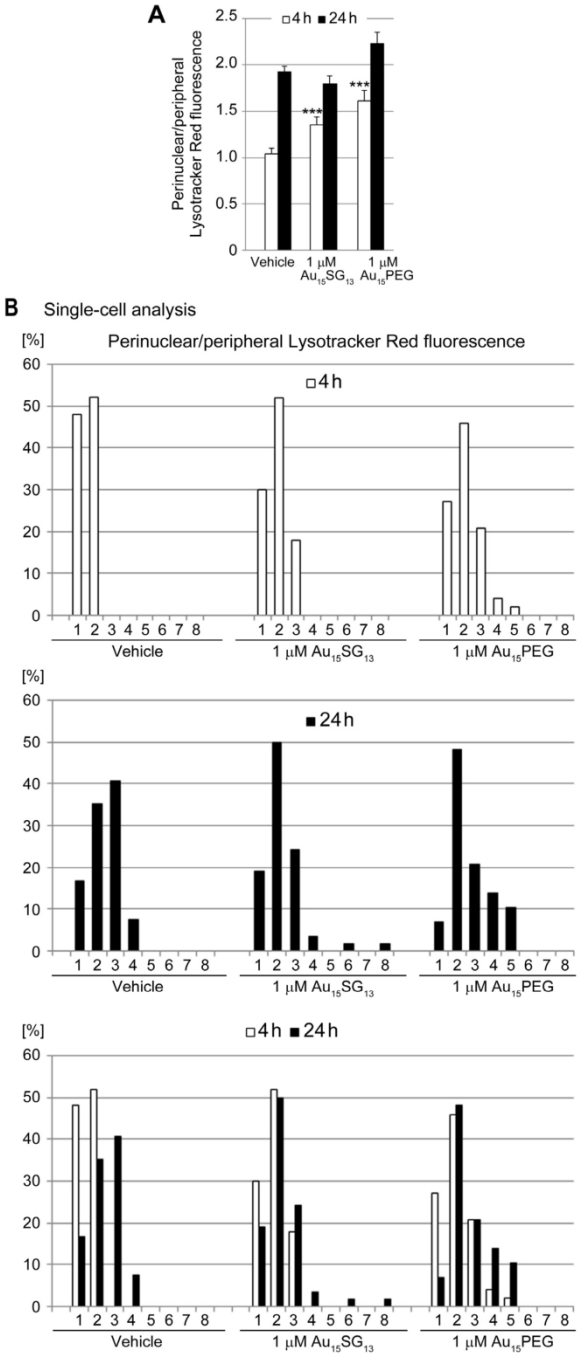

Figure S4. Detailed analysis of Lysotracker Red signal distribution. An in-depth evaluation was performed for the perinuclear and peripheral localization of lysosomes. The assessment was carried out on raw data calculated for the perinuclear/peripheral ratio of Lysotracker Red signals. (A) Bar graph depicting the ratio for vehicle, 1 µM $Au_{15}SG_{13}$ or 1 µM $Au_{15}PEG$ at 4 and 24 hours. Bars represent average ± SEM; in two independent experiments 43 to 58 cells were assessed for each condition; ***p<0.001. (B) The perinuclear/peripheral ratio of Lysotracker Red was evaluated for single cells and results of two independent experiments were binned. All bins have equal size. For example, bin 1 represents cells with a ratio of 0 to <1; bin 2 contains cells with a ratio of 1 to <2. The bars depict the percentage of cells in each bin.

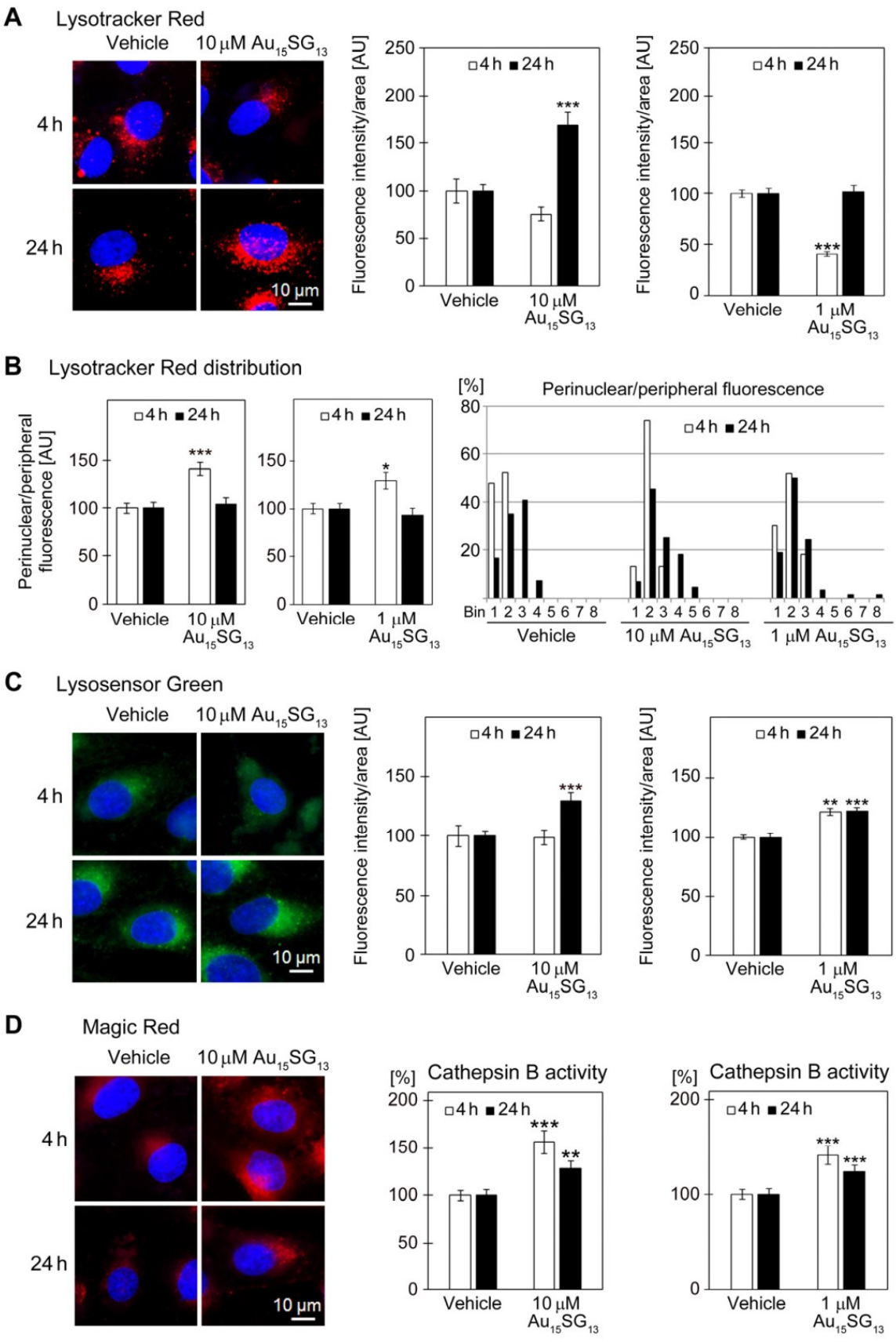
A
Lysotracker Red
Vehicle
10 μM Au15SG13
4 h
24 h
10 μm
Fluorescence intensity/area [AU]
□4 h ■24 h
***
Vehicle
10 μM Au15SG13
1 μM Au15SG13
B
Lysotracker Red distribution
Perinuclear/peripheral fluorescence [AU]
*
[%]
Perinuclear/peripheral fluorescence
Bin 1 2 3 4 5 6 7 8
C
Lysosensor Green
**
D
Magic Red
Cathepsin B activity

Figure S5. Impact of 10 µM $Au_{15}SG_{13}$ on the properties of acidic vesicles. U251N cells were treated and analyzed as described for Figures 3 and 6, with a final concentration of 10 µM $Au_{15}SG_{13}$. For comparison, bar graphs with the results for 1 µM $Au_{15}SG_{13}$ are also shown (see main manuscript). (A) Between 22 and 49 cells were scored with Lysotracker Red for each data point in two independent experiments. (B) Lysotracker Red distribution was determined for at least 38 cells per condition and two independent experiments. Binning was performed as described for Figure S4. (C) Lysosensor Green signals were quantified for 24 to 41 cells for each condition. One representative experiment was evaluated for the 4-hour time point; two independent experiments were assessed for the 24-hour incubation period. (D) Cathepsin B activity was quantified for at 53 to 92 cells per condition. Results for two independent experiments are depicted as average ± SEM; *$p<0.05$, **$p<0.01$, ***$p<0.001$.

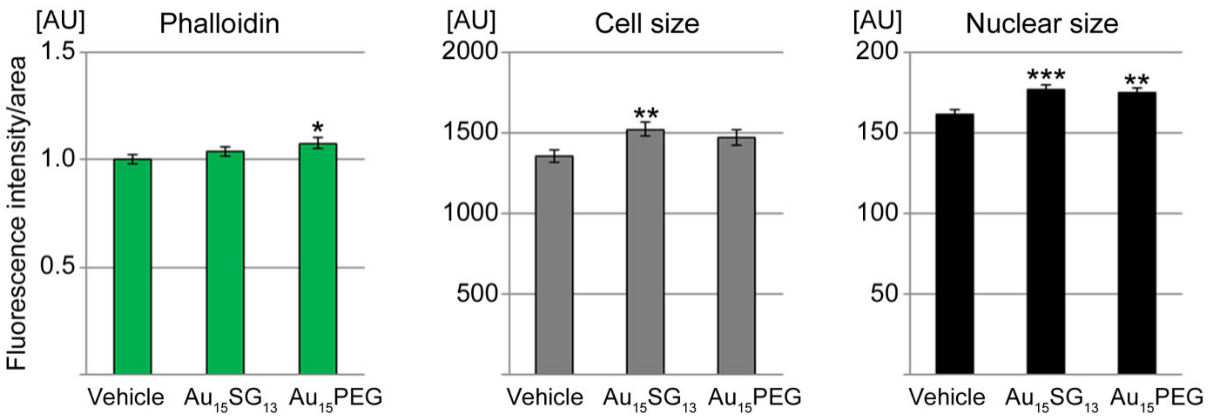

Figure S6. Effects of 1 µM $Au_{15}SG_{13}$ and $Au_{15}PEG$ on F-actin formation, cell and nuclear size. U251N cells were incubated 24 hours with vehicle, 1 µM $Au_{15}SG_{13}$ or 1 µM $Au_{15}PEG$. Cells were fixed, processed and imaged as described for Figure 5. F-actin was stained with Alexa Fluor® 488 phalloidin. Fluorescence intensities/cell area, cell and nuclear size were quantified. Results are shown for a representative experiment as average ± SEM. Between 97 and 103 cells were assessed per condition for phalloidin fluorescence and cell size. The size of nuclei was measured for 170 to 194 cells for each data point. Student's t-test uncovered significant differences between the vehicle control and AuNC-treated cells; *, $p<0.05$; **, $p<0.01$; **, $p<0.001$. AU, arbitrary units.

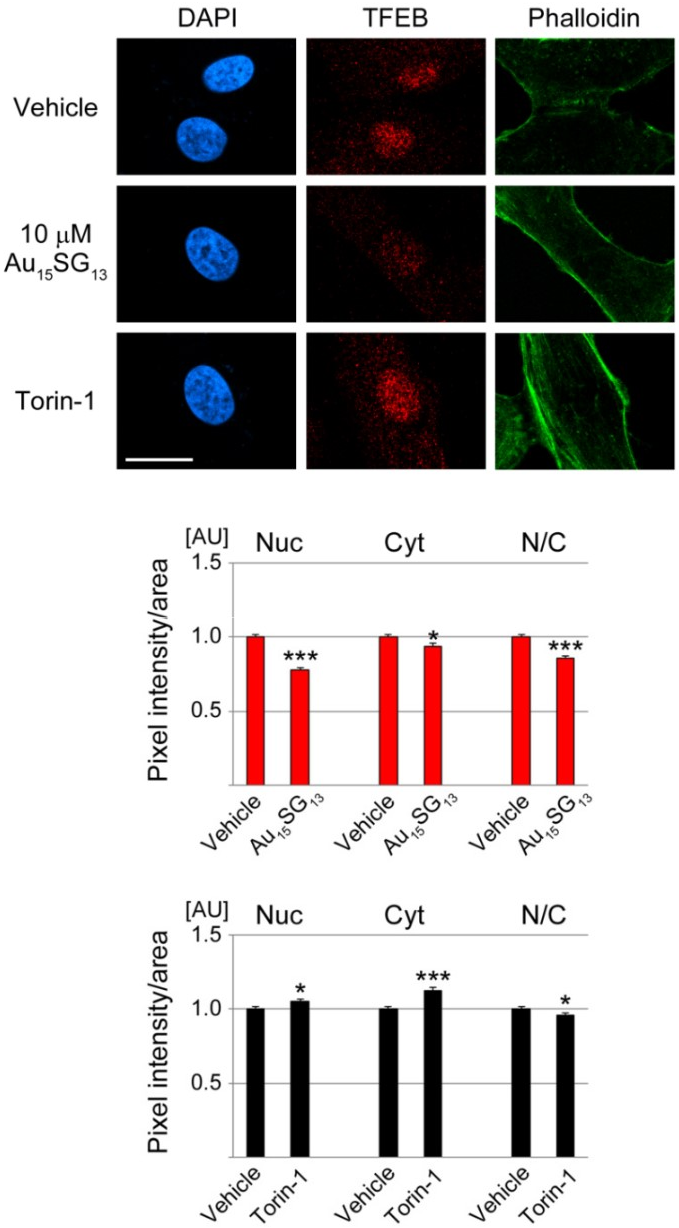

Figure S7. Effects of $Au_{15}SG_{13}$ and the mTOR inhibitor Torin-1 on the nucleocytoplasmic distribution of TFEB. Immunocytochemistry located TFEB in U251N cells treated for 24 hours with vehicle (175 cells), 10 μM $Au_{15}SG_{13}$ (205 cells) or 2 μM Torin-1 (165 cells). DAPI stained the nucleus; scale bar is 20 μm. Pixel intensities in the nucleus/area (Nuc), cytoplasm/area (Cyt) and the ratio nuclear/cytoplasmic fluorescence (N/C) was determined for one representative experiment. Results normalized to the vehicle control are depicted as average ± SEM. Student's t-test identified significant differences between vehicle and AuNC-treated samples; *, $p<0.05$; ***, $p<0.001$. AU, arbitrary units.

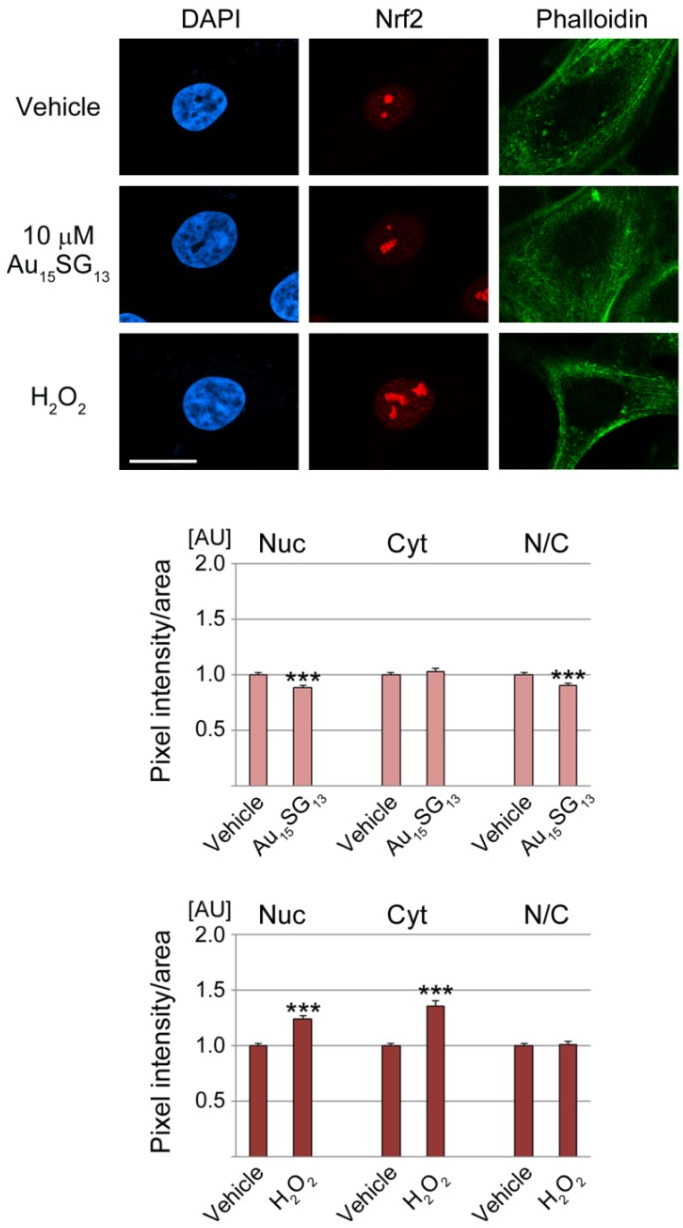

Figure S8. Effects of $Au_{15}SG_{13}$ and hydrogen peroxide on the nucleocytoplasmic distribution of Nrf2. Immunocytochemistry located Nrf2 in U251N cells treated for 24 hours with vehicle (196 cells), 10 μM $Au_{15}SG_{13}$ (179 cells) or 300 μM hydrogen peroxide (165 cells). DAPI demarcated nuclei; scale bar is 20 μm. Pixel intensities in the nucleus/area (Nuc), cytoplasm/area (Cyt) and the ratios of nuclear/cytoplasmic fluorescence (N/C) were determined for one representative experiment. Results normalized to the vehicle control are shown as average ± SEM. Student's t-test identified significant differences between vehicle and AuNC-treated samples; ***, $p<0.001$.

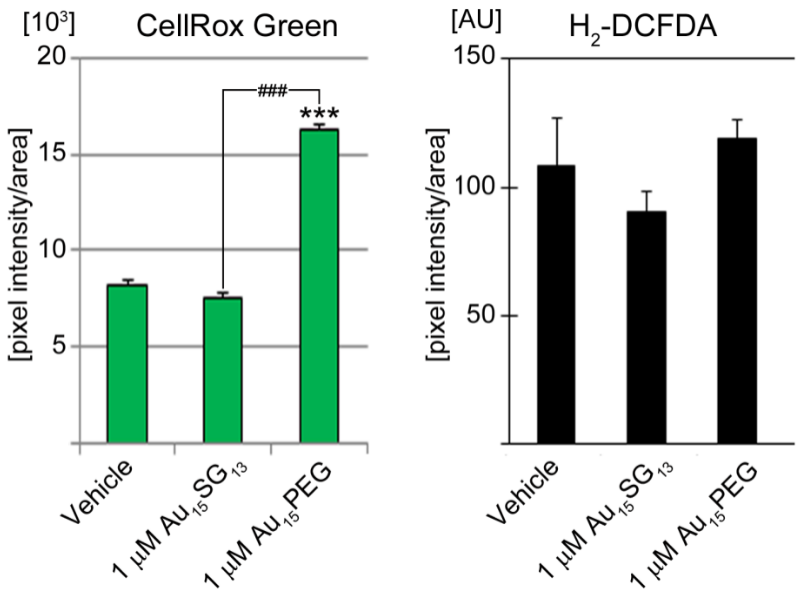

Figure S9. AuNC-dependent production of reactive oxygen species (ROS). U251N cells were treated with vehicle, 1 µM $Au_{15}SG_{13}$ or 1 µM $Au_{15}PEG$ for 24 hours, as in Figure 8. CellRox® Green or H_2-DCFDA was used to monitor changes in ROS abundance. Microscopic images were acquired, and pixel intensities were quantified per nuclear area (CellRox® Green) or per cell area (H_2-DCFDA). ROS production was evaluated for a typical experiment with CellRox® Green (192 to 215 cells per condition) or H_2-DCFDA (30 to 47 cells for each condition). Bars depict average +SEM. Student's t-test revealed significant differences between the vehicle control and AuNC-treated cells (***, $p<0.001$), or between cells treated with 1 µM $Au_{15}SG_{13}$ and 1 µM $Au_{15}PEG$. Note that CellRox® Green and H_2-DCFDA differ in the signal-to-noise ratio and stability.

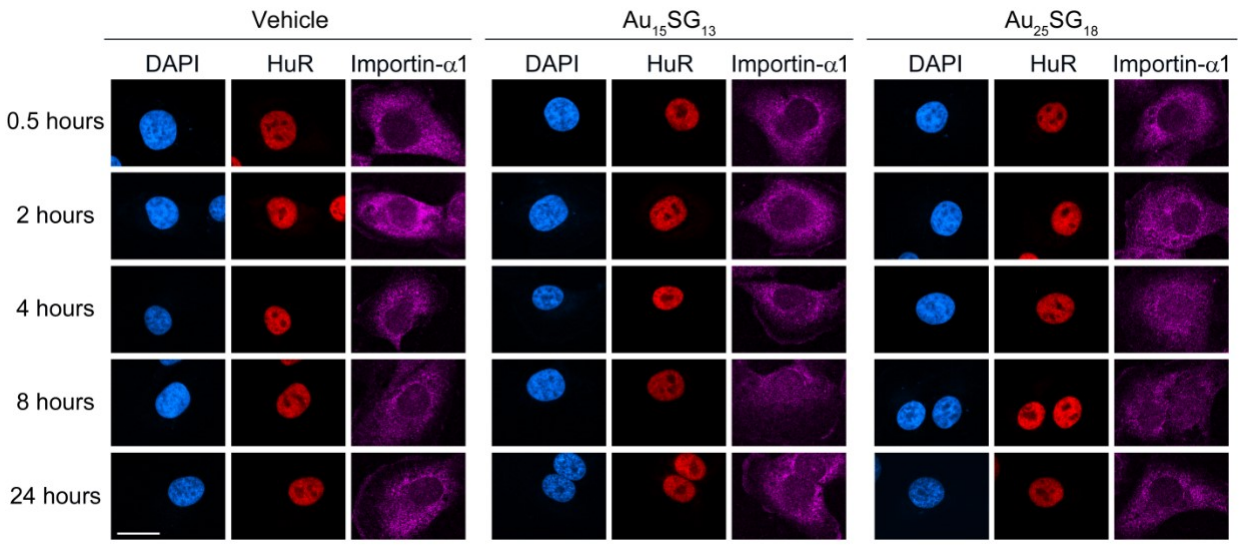

Figure S10. Lack of stress granule formation in response to AuNC treatment. U251N cells were incubated with vehicle, 10 μM $Au_{15}SG_{13}$ or 10 μM $Au_{15}PEG$. At the times indicated, samples were fixed and processed for immunocytochemistry for the detection of HuR and importin-α1. Nuclei were stained with DAPI. Scale bar is 20 μm.

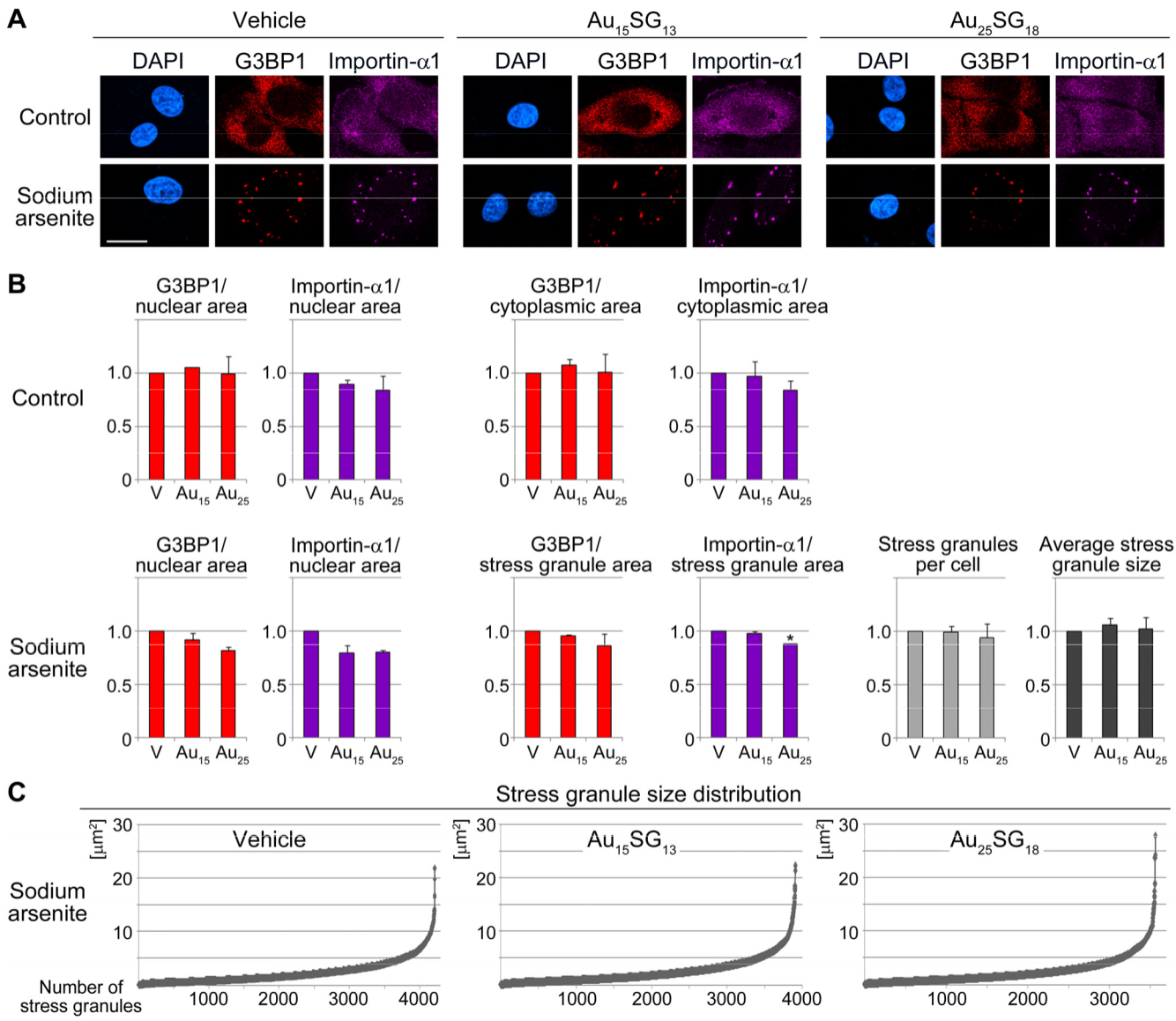

Figure S11. AuNC-induced changes in stress granule formation. U251N cells were incubated with vehicle, 10 µM $Au_{15}SG_{13}$ (Au_{15}) or 10 µM $Au_{25}SG_{18}$ (Au_{25}) for 24 hours and kept under non-stress control conditions (control) or exposed to oxidative stress (0.5 mM sodium arsenite, 2 hours). (A) The stress granule components G3BP1 and importin-α1 were detected by immunocytochemistry. Nuclei were demarcated with DAPI; scale bar is 20 µm. (B) Fluorescence intensities were measured for G3BP1 and importin-α1. Results were normalized to vehicle controls (V). Fluorescence signals/area were quantified in the nuclear and cytoplasmic compartments for 162 to 203 non-stressed cells (control, no sodium arsenite) per experiment and for each treatment. Nuclear pixel intensities/area were determined for 112 to 149 arsenite-treated cells for each of two independent experiments and per condition. Between 1448 and 2422 stress granules were assessed per experiment for each treatment. One-way ANOVA combined with Bonferroni posthoc analysis was performed for statistical evaluation; *$p<0.05$. (C) The stress granule size distribution was determined for the combined results of two independent experiments.

Connecting text

Chapter 2 provided data on AuNC effects in malignant astrocytes (i.e., GBM cells). The unanswered question remaining from these studies is the following: do AuNCs exert deleterious effects in the GBM microenvironment? The tumor microenvironment contributes to resistance to radiotherapy and chemotherapy of GBM cells, posing a major obstacle in GBM treatment. Of these interactions, astrocytes are paramount players in the progression of GBM tumors.

In **Chapter 3**, we describe the effects of AuNCs with varying sizes (Au_{10}, Au_{15}, Au_{18}, Au_{25}) and ligands (glutathione, polyethylene glycol, N-acetyl cysteine) on organellar homeostasis and cellular stress responses in human primary astrocytes. These effects were detected by changes in redox status, mitochondria abundance and morphology, lipid droplet number and distribution and activation of redox-responsive molecular pathways.

Elucidating organellar reorganization and stress responses will give us a better understanding on how astrocytes in the tumor microenvironment respond when exposed to these gold nanostructures. Results show that AuNCs can counteract undesirable effects caused by mild oxidative stress via reorganization of organelles and activation of cytoprotective transcription factors.

Chapter 3. Gold nanoclusters alter organellar state and translocation of transcription factors in human primary astrocytes[2]

Evan Rizzel Gran, Franck Bertorelle, Hussein Fakhouri, Rodolphe Antoine, Martina Perić Bakulić, Željka Sanader Maršić, Vlasta Bonačić-Koutecký, Manon Blain, Jack Antel, Dusica Maysinger

[2] Submitted to Nanoscale (in review).

3.1. Abstract

Astrocytes are the most abundant glial cells in the central nervous system maintaining cellular homeostasis, but also contributing to the onset and progression of neurological disorders. Astrocytes respond to stressors including reactive oxygen species (ROS). Gold nanoclusters (AuNCs) can modulate ROS quantities in cells. AuNCs were characterized at the atomic level, where computational analyses show size-dependent water penetration to the gold cluster core. In this study, primary human astrocytes were treated with AuNCs of varying sizes (Au_{10}, Au_{15}, Au_{18}, Au_{25}) and ligand composition (glutathione, polyethylene glycol, N-acetyl cysteine). Non-cytotoxic concentrations of AuNCs alter organellar state in human primary astrocytes and activate cytoprotective transcription factors in a size-dependent manner. Under mild oxidative stress at sublethal concentrations, AuNC re-balanced mitochondrial state and lipid droplet number and position in primary human astrocytes. Lipid droplets play a protective role by sequestering and reducing 4-hydroxynonenal, a major product of lipid peroxidation in the treated cells. AuNCs induce nuclear translocation of nuclear factor E2-related factor 2 and modulate the abundance of heat shock protein 70 in astrocytes under mild oxidative stress. AuNCs also show corrective influence on LPS-induced high mobility group box 1 nuclear release. In contrast, under severe oxidative stress induced by menadione, AuNCs are unable to sufficiently activate protective transcription factors to reduce by-products of excessive reactive oxygen species. Collectively, these findings suggest that AuNCs are not inert nanostructures in primary human astrocytes, and that their sizes play a critical role in modulation of organellar homeostasis and redox-responsive transcription factors in human primary astrocytes.

Keywords: gold nanoclusters, lipid droplets, mitochondria, cellular stress response, primary human astrocyte

3.2. Introduction

Gold nanoclusters (AuNCs) are extensively used for bioimaging and therapeutic purposes. There is growing research on AuNCs due to their chemical and physical characteristics, but also their intriguing catalytic properties (Chakraborty and Pradeep, 2017; Du and Jin, 2019; Jin et al., 2016; Kang et al., 2018). These nanostructures are versatile owing to the tunability of their sizes and functionalization, few of these nanoclusters synthesized with less than 100 gold atoms. Several studies in mice have shown that AuNCs are readily eliminated by the kidneys compared to other nanomaterials, and can accumulate passively in tumors (Porret et al., 2020). Previously, we have shown the effectiveness of AuNCs with 15 or 25 gold atoms to disturb organellar homeostasis in glioblastoma cells (Maysinger et al., 2020). A complex crosstalk between glial and glioblastoma cells contributes to tumor malignancy (Matias et al., 2018). Astrocytes represents the most prominent type of glial cells in the brain and the tumor. microenvironment. They play a pivotal role in nurturing and protecting neurons, such that damage to these glial cells is detrimental to normal neuronal function. Dysfunctional and reactive astrocytes are implicated in progression of multiple neurodegenerative disorders including multiple sclerosis, ALS, and Alzheimer's disease and other diseases, such as glioblastoma – hence understanding the role of human astrocytic response to nanotherapy is essential. However, data regarding human astrocytes and their interactions with nanostructures are sparse. In contrast, extensive studies were carried out with gold nanostructures including gold nanoclusters in rodent models but they cannot be directly translated to the human cell because of the differences between the morphology, genetic profile, variety and function of human and rodent astrocytes (Healy et al., 2020; Vasile et al., 2017). To the best of our knowledge, this study is among the first to report the response of primary human astrocytes to a range of ultra-small gold nanoclusters with varying sizes and ligand compositions.

Internalized nanostructures can trigger the activation of cytoprotective and deleterious processes in neural cells. A transcription factor, nuclear factor E2-related factor 2 (Nrf2) is a critical player in neuroprotection. Nrf2 regulates over a hundred antioxidant and cytoprotective genes. *In vitro* and *in* vivo evidence suggest that Nrf2

signaling is strongly induced in astrocytes, and thus conferring protection to neighboring neural cells. (Vargas et al., 2008) Under physiological conditions, Nrf2 resides in the cytosol and is bound by Kelch-like erythroid Keap1 (Keap1), an adapter protein that targets Nrf2 for proteasomal degradation. Exposure of Keap1 cysteine residues to oxidants or electrophiles lead to Nrf2 detachment and translocation to the nucleus. Nrf2 binds to antioxidant response element (ARE) promoter regions, targeting genes involved with glutathione and thioredoxin antioxidant systems (Robledinos-Antón et al., 2019a). Dysregulation of Nrf2 leads to sensitization to redox-associated stresses. As a result, Nrf2 has become an important clinical target for conditions underlined by oxidative stress and inflammation, such as cancer and neurodegenerative diseases (Liddell, 2017; Vargas et al., 2008). Another transcription factor of interest in astrocytes associated with physiological and pathological conditions is high mobility group box 1 (HMGB1).

HMGB1 is a transcription factor conserved and expressed in all nucleated animal cells. Plant and fungal species also have closely related proteins, showing the importance of HMGB1 biological function. HMGB1 acts as alarmin both extra- and intra-cellularly (Andersson et al., 2018a; Lotze and Tracey, 2005). Compartmentalization determines HMGB1 function, which is tightly regulated by its molecular binding partners and redox state. Normally, HMGB1 localizes in the nucleus. Inside the nucleus, HMGB1 enhances transcriptional activation and may act as DNA chaperone (Reeves, 2010). When altered by post-translational modification (e.g. acetylation), HMGB1 is exported from the nucleus. Once released into the cytosol and ultimately the extracellular space, HMGB1 mediates inflammation, modulates chemokine and cytokine functions, neuroimmune activities and metabolic activities (Lotze and Tracey, 2005).

Similar to HMGB1, hear shock protein 70 (HSP70) may be released into the extracellular space and act as an alarmin (Gülke et al., 2018). HSP70 is responsive to different stressors; it can be induced and modified at the post-translational level (Griffith and Holmes, 2019). HSP70 fulfills several housekeeping activities by acting as a chaperone. In the cytosol, expression of HSP70 prevents protein aggregation, and aids

in refolding misfolded or aggregated proteins. Cellular distribution of proteins including cytoplasmic transcription factors is often linked with their association with organelles.

As a part of homeostatic and adaptive processes, changes in organellar distribution, morphology and function are also characteristic of cellular stress response. Such subcellular structures are tightly interconnected, namely mitochondria, lipid droplets and lysosomes. Mitochondria are the center of cellular signaling, metabolism and redox balance in a cell (Willems et al., 2015). Disruption of mitochondrial function can lead to deregulation in cellular reactive oxygen species and ultimately, cell death. Damaged mitochondria can be degraded by mitophagy, a process which involves the lysosomal degradation pathway. Lysosomes eliminate damaged mitochondria by mitophagy (Lemasters, 2005; Palikaras et al., 2018) and other damaged cell compartments (Kroemer and Jäättelä, 2005). Studies by several groups including ours, showed that mitochondria and lipid droplets interact (Tremblay et al., 2016). Peroxidized lipids produced by oxidative damages, are often accumulated in lipid droplets. Lipid droplets are mainly recognized as storage organelles, but their functions are far beyond this. Lipid droplets play both the protective and destructive roles in neural and other cells depending on their inducing stimuli, size and associated surface proteins (Thiam and Dugail, 2019). We have previously shown that lipid droplet formation is induced in the mouse neural cells exposed to nanocrystals quantum dots (Griffith and Holmes, 2019). Lipid droplet abundance and size change with different treatments and exposures to viruses and bacterial toxins (Herker and Ott, 2012; Libbing et al., 2019).

Herein, we investigate ultra-small AuNCs that, given select size and ligand composition, elicit protective mechanisms in human astrocytes, sufficient to reduce by-products of oxidative stress. L-buthionine sulfoximine (BSO) or menadione (MenD) were used as pharmacological tools to disrupt redox homeostasis. Human astrocytes were treated with sublethal concentration of AuNCs of varying sizes (Au_{10}, Au_{15}, Au_{18}, Au_{25}) and ligand composition (glutathione, acetylcysteine, polyethylene glycol). Our study reveals organellar reorganization upon AuNC treatment, as well as the activation of key cytoprotective transcription factors. Taken together, the assessment of organellar reorganization and redox-responsive transcription factor regulation by AuNC

characterized at the atomic level will allow for better understanding of neural and other cellular responses to these and other gold nanostructures.

3.3. Results and Discussion

3.3.1. Synthesis and characterization of AuNCs

The control of the number of gold atoms in ultra-small gold nanoclusters (AuNCs) at the atomic precision allows for an exhaustive observation of size dependency on the interactions of gold nanoclusters with primary human astrocytes. Xie and coworkers reported the gram-scale production of various discrete-sized AuNCs ($Au_{10–12}$, Au_{15}, Au_{18}, and Au_{25}) protected by glutathione (GSH) were synthesized by via pH Controlling CO Reduction (Yu et al., 2013) **(Fig. S1†)**. Such nanoclusters display sizes in the 1-3 nm range (Soleilhac et al., 2017) and has allowed for an exploration of the size dependency in glomerular filtration. It was reported a slowdown in the extravasation of sub-nanometer AuNCs from normal blood vessels and enhances their passive targeting to cancerous tissues through an enhanced permeability and retention effect. (Du et al., 2017) As a consequence, ultrasmall glutathione-protected gold nanoclusters were proposed as next generation radiotherapy sensitizers with high tumor uptake and high renal clearance (Zhang et al., 2015).

Ascorbic acid, glutathione, and N-acetyl cysteine (NAC, a precursor of glutathione) are known antioxidants that have been used in clinical practice. In a facile AuNC synthetic process with NAC, this compound served both as a reducing agent and as a pH -responsive ligand (Deng et al., 2015). However, while atomically precise gold clusters were synthesized with L-cysteine (Russier-Antoine et al., 2014; Yuan et al., 2012), to our knowledge, it was not the case for NAC as ligands.

In this study two strategies were explored: (i) AuNCs of different sizes but with the same surface ligand, e.g. GSH ($Au_{25}SG_{18}$, $Au_{18}SG_{14}$, $Au_{15}SG_{13}$ and $Au_{10}SG_{10}$). (ii) AuNCs with the same size but different ligands, e.g. Au_{15} or Au_{25}, and GSH, PEG or NAC.

Not only the size increases from Au_{10} to Au_{25}, but also subtle changes in the structures of NCs are observed. For $Au_{10}(SG)_{10}$, a catenane structure containing two interpenetrating pentagons has been found to be the most stable structure (Bertorelle et al., 2017). The structure of $Au_{25}SG_{18}$, $Au_{18}SG_{14}$, and $Au_{15}SG_{13}$ have not been yet addressed by X-Ray single crystal. For $Au_{15}SR_{13}$, De-en Jiang proposed an “asymmetric” shape with cyclic [Au(I)-SR] pentamer in the ligand shell, together with two regular trimer motifs, protecting a Au_4

nucleus (Jiang et al., 2013). However, X-ray crystal structure of $[Au_{18}(SC_6H_{11})_{14}]$ cluster exhibits an unprecedented bi-octahedral (or hexagonal close packing) Au_9 kernel protected by staple-like motifs including one tetramer, one dimer, and three monomers (Das et al., 2015). Finally, the 25-gold-atom cluster (1.27 nm diameter, surface-to-surface distance) protected by eighteen phenylethanethiol ligands exhibits a "spherical" shape with a quasi-icosahedral Au_{13}-core fully protected by four -SR-Au-SR- and two -SR-Au-SR-Au-SR- staple motifs (Zhu et al., 2008).

In order to study different accessibility of biological targets toward the gold cluster core, we carried out simulations allowing the penetration of water into glutathione ligated $Au_{10}SG_{10}$, $Au_{15}SG_{13}$, $Au_{18}SG_{14}$, and $Au_{25}SG_{18}$ nanoclusters. Our findings illustrated in **Fig. 1** clearly shows the difference between smaller cluster sizes Au_{10}, Au_{15} and Au_{18} versus Au_{25}. The symmetrical structure of Au_{25} is completely protected by 18 glutathione molecules and does not allow penetration of water molecules close to the core which is not the case for smaller size clusters. Only one water molecule approaches the core of $Au_{25}SG_{18}$. In fact, dependent on the structural properties, penetration of water is lower for Xray structure of $Au_{18}SG_{14}$ (Das et al., 2015) then for the DFT predicted one (Tang and Jiang, 2015), as can be seen from the insert window in **Fig. 1A,** as well as from **Fig. 1B**. In addition, $Au_{15}SG_{13}$ is more accessible to water than $Au_{10}SG_{10}$ due to the compact catenane structure in the latter case (cf insert in **Fig. 1**). Notice that for distances larger than 10 Å, accessibility of water is present independent from the cluster size. Based on these described findings, we expected size-dependent effects in primary human astrocytes treated with ligated gold nanoclusters.

3.3.2. AuNCs activate Nrf2 oxidative stress response and modulate HSP70 protein abundance

Response implicated in nanostructure-induced oxidative stress and toxicity highly involves the concerted activation of master transcription factors Nrf2 (Manke et al., 2013a; Zheng and Li, 2019). To determine whether AuNCs activate these cytoprotective pathways, we performed immunocytochemical analyses of their intracellular distribution in human astrocytes **(Fig. 2).** One-hour treatment of 10 μM AuNC with larger number of gold atoms (Au_{18}, Au_{25}), regardless of ligand composition, is sufficient to induce an increase in nuclear-to-cytosolic Nrf2 ratio of at least 21.27±4.67% ($p<0.001$) **(Fig. 2B)**. Among the AuNCs with smaller number

of gold atoms, Au_{15}PEG is the only one to induce Nrf2 activation, that is an increase in nuclear-to-cytosolic Nrf2 ratio of 20.71±4.51% ($p<0.001$) compared to vehicle control **(Fig. S2B†)**. Under oxidative stress mediated by buthionine-sulfoximine (BSO), all AuNCs, regardless of size or ligand composition, caused a greater increase of 8.31±5.19% to 39.91±8.53% ($p<0.001$) in nuclear-to-cytosolic Nrf2 ratio compared to human astrocytes treated with BSO alone (2.82±4.06%) **(Fig. S2B†)**. However, when cells are treated with menadione, AuNCs fail to increase nuclear-to-cytosolic Nrf2 ratio, in exception of Au_{25}PEG and $Au_{25}AcCys_{18}$. Although not statistically significant, these AuNCs showed respectively 25.95±7.83% and 23.50±6.10% increase in Nrf2 ratio compared to MenD treatment alone (12.68±4.55%, $p<0.05$) **(Fig. S2C†).**

Nrf2 total protein abundance was decreased by AuNC up to -35.01±2.23% ($p<0.001$) in the absence of drugs (MenD or BSO) that change cellular redox status **(Fig. S3A†)**. Interestingly, when oxidative stress in human astrocytes was induced by glutathione depletion using BSO or by ROS accumulation using MenD, AuNCs was found to differentially modulate the total Nrf2 protein levels depending on the stress stimulus. AuNCs cause an overall decrease in total Nrf2 protein levels in BSO-mediated glutathione depleted condition between -6.76±5.62% to -45.45±4.76% ($p<0.001$) **(Fig. S3B†)**. In contrast, AuNCs cause an overall increase in total Nrf2 protein levels in menadione-mediated oxidative stress between 26.13±6.12% to 109.39±16.18% ($p<0.001$), whereas treatment with MenD alone only increases total Nrf2 levels by 30.25±6.52% ($p<0.001$) **(Fig. S3C†)**.

As a proteolytic defense mechanism, heat shock proteins (HSP) are produced at high levels and can be used as indicators of cellular stress (Aït-Aïssa et al., 2003; Lewis et al., 1999). In denaturing conditions, such as extreme temperatures or oxidative stress, expression and distribution of HSP proteins are changed (Griffith and Holmes, 2019). One of the most studied HSP proteins is HSP70. Levels of HSP70 in the cell can change following exposure to stressors. To assess stress levels in human astrocytes, we monitored the changes in intracellular HSP70 proteins treated with AuNCs **(Fig. 2C-D)**.

Considering that some proteins can undergo degradation or elimination within an hour or less, we determined the abundance of HSP70 after one hour. Within one hour of

treatment, all AuNC treatment (except $Au_{15}SG_{13}$) reduced intracellular HSP70 protein content by 10.57±1.88% to 16.60±2.05% ($p<0.001$) in human astrocytes **(Fig. 2D)**. There was no overall change in HSP70 levels when human astrocytes were treated with $Au_{15}SG_{13}$ alone (-1.41±3.28%, $p>0.05$). Depending on the pharmacological inducer of oxidative stress, AuNCs differentially regulated intracellular HSP70 protein content. When glutathione was depleted by BSO treatment, all AuNCs, in exception to $Au_{10}SG_{10}$, further reduced HSP70 protein content by 6.14±5.75% to 31.78±2.30% ($p<0.001$) **(Fig. S4C†)**. When cells were treated with menadione, a strong inducer of oxidative stress, HSP70 levels increased by 81.99±6.28% ($p<0.001$) above levels in vehicle-treated cells **(Fig. S4D†)**. AuNCs with smaller number of gold atoms (Au_{10}, Au_{15}, Au_{18}) reduced the production of HSP70 caused by menadione treatment above control levels, between 32.59±5.09% to 42.28±5.67% ($p<0.001$). Interestingly, among AuNCs with Au_{25}, only $Au_{25}AcCys_{18}$ was found to reduce production of HSP70 caused by menadione.

3.3.3. AuNCs enhance HMGB1 relocation

Another important transcription factor involved in stress responses is HMGB1 (Tang et al., 2011; Yu et al., 2015). HMGB1 plays a critical role in the CNS, where its release into the extracellular space is known to contribute to pathogenesis (Andersson et al., 2018b; Fang et al., 2012). Glial cells, including astrocytes, contribute to the release of HMGB1 into the extracellular milieu in response to stressful stimuli (Fang et al., 2012). In this study, the ability of AuNCs to cause HMGB1 relocation in basal and stressed conditions was determined by immunocytochemistry. Cells treated with AuNCs alone did not show significant change in HMGB1 intracellular distribution **(Fig. 2E)**. LPS served as positive control, where LPS drives the release of HMGB1 from the nucleus into the cytosol, and eventually into the extracellular matrix. As anticipated, LPS reduced HMGB1 nuclear-to-cytosolic ratio, by -28.12±4.63% ($p<0.001$) below the levels in vehicle-treated cells **(Fig 2G)**. However, treatments with smaller AuNCs can reduce LPS-induced HMGB1 translocation outside the nucleus, where $Au_{15}SG_{13}$ increased nuclear-to-cytosolic HMGB1 ratio by 60.17±9.02% ($p<0.001$) compared to vehicle control **(Fig. 2F)**. In contrast, larger AuNC are less effective at reducing LPS-induced HMGB1 translocation.

3.3.4. AuNC treatments exert negligible toxicity in human astrocytes

To evaluate the ability of AuNCs to affect cell survival, human astrocytes were cultured and treated with 10 μM AuNC. Little to no decline in cell viability was observed at 10 μM of all AuNCs after 24 hours **(Fig. S5†)**. These results support previous findings, where high concentrations of AuNCs (up to 100 μM) did not decrease cell viability in organotypic culture or primary mouse astrocytes after 24 hours (Ji et al., 2019). Assessment of nuclear morphology using Hoechst 33342 fluorescent dye show minimal effects of AuNCs on nuclear area size, suggesting no early signs apoptotic cell death characterized by pyknotic nuclei **(Fig. S6†)**.

3.3.5. AuNCs affects mitochondrial redox homeostasis

To investigate how AuNCs impacts cellular homeostasis, we evaluated the effect of AuNC treatments on the oxidative status of human astrocytes. Regardless of ligand composition, AuNCs with smaller gold number (Au_{10}, Au_{15}, Au_{18}) and not larger (Au_{25}), increased baseline CellROX fluorescence by 13.06±0.66% to 16.24±0.82% ($p<0.05$) **(Fig. 3A)**. Under oxidative stress induced by menadione treatment, AuNCs with smaller gold number (Au_{10}, Au_{15}, Au_{18}) induced the greatest increase in ROS, that is at least double the increase caused by menadione treatment alone **(Fig. 3B)**. Whereas AuNCs with larger gold number (Au_{25}) could even reduce ROS levels below that of endogenous ROS in human astrocytes treated with menadione alone, that is up to a 147.56% reduction ($p<0.05$) with $Au_{25}AcCys_{18}$.

The changes in the levels of reactive oxygen species by AuNC raises the question of how organellar structures could be affected by these gold nanostructures. We examined the morphology and density of mitochondria, a fundamental source of reactive oxygen species in astrocytes treated with AuNC with 10-25 gold atoms (Dan Dunn et al., 2015). To determine whether the increase of reactive oxygen species was accompanied by changes in mitochondria, MitoTracker Deep Red was used **(Fig. 3C)**. MitoTracker is a mitochondrial-selective fluorescent label that maximally sequesters in active mitochondria with undisrupted membrane potentials. A decrease in MitoTracker labelling was detected when human astrocytes were treated with 10 μM of any AuNC in serum-deprived media. The greatest decrease was found when human astrocytes were treated with AuNCs with 25 gold atoms, the most significant with $Au_{25}AcCys_{18}$ (-54.47±2.03%, $p<0.001$) **(Fig. 3D)**.

3.3.6. AuNCs modulate lipid droplet distribution, abundance, and lipid peroxidation

Dysfunctional mitochondria are a source of reactive oxygen species, which can lead to the oxidation of several biomolecules, including DNA, proteins, and lipids. Lipid peroxidation products, such as 4-HNE, can react with other macromolecules such as DNA and proteins, causing adduct formation and cross-linking. Thus, cells must rely on several different protective mechanisms to deal with the accumulation of oxidative products. One of such protective mechanisms involves lipid droplet formation. Lipid droplets are dynamic structures mainly deriving from endoplasmic reticulum. They are pleiotropic dynamic organelles mainly known for their role as storage organelles for neutral lipids. Lipid droplets can associate with different proteins and interact with different organelles, including lysosomes, mitochondria and other lipid droplets (Thiam and Dugail, 2019). These organelles are often held in the proximity of lipid droplets to allow exchange of lipids and proteins (Olzmann and Carvalho, 2019). Importantly, lipid droplets are critical to buffer levels of toxic lipid sources from the cell membrane or membranes of damaged organelles. Our goal was to determine if AuNCs modulate lipid homeostasis and induce lipid droplet formation. We assessed changes in lipid droplet distribution and number in human astrocytes (**Fig. S7†)**. Neutral lipids were labelled using BODIPY 493/503 fluorescent dye. Staining of lipid droplets showed that, regardless of size, AuNC with glutathione ligands, did not significantly change lipid droplet distribution or number (**Fig. S7A†)**. Vehicle-treated control human astrocytes showed approximately 18±1.77 lipid droplets per cells, whereas, oleic acid (OA) treatment, which served as a positive control, resulted in lipid droplet number over 152±12.81 (**Fig. S7B†)**. Mean distance of lipid droplets was maintained in human astrocytes treated with AuNCs with smaller number of Au (Au_{10}, Au_{15}) similar to control (23.64±1.11 μm from the center of the nucleus) (**Fig. S7C†)**. Interestingly, treatments with Au_{25}PEG or $Au_{25}AcCys_{18}$ increased number of lipid droplets closer to the nucleus, (distance of 20.66±0.69 μm ($p<0.05$) or 20.56±1.52 μm ($p<0.05$) relative to the center of the nucleus, respectively). Both treatments with Au_{25}PEG or $Au_{25}AcCys_{18}$ also slightly increased lipid droplet number to 30±2.79 ($p<0.001$) or 31±1.59 ($p<0.001$) relative to the vehicle-treated control, respectively.

To determine whether the redistribution and changes in lipid droplet number caused by AuNCs served as protective mechanism against lipid perodixation, we performed immunofluorescence analyses on the abundance of 4-HNE adducts, one of the major

products of advanced lipid peroxidation. Remarkably, 24-hour treatment of only 10 μM AuNC was sufficient to decrease baseline 4-HNE levels between -5.06±2.39% and 19.05±2.71% ($p<0.001$) **(Fig. 4B)**. This suggests that Nrf2 and HMGB1 participate in protective mechanisms triggered in response to AuNCs. Under oxidative stress induced by glutathione depletion, AuNCs also prevented the accumulation of 4-HNE products **(Fig. 4C)**. However, AuNCs could not prevent menadione-induced accumulation of 4-HNE products in astrocytes, but instead, exacerbated its effects **(Fig. 4D)**.

Among gold nanostructures, gold nanoclusters (AuNCs) are of significant interest in biomedical research, pre-clinical and eventually clinical studies due to their high stability, unique optical properties, easy preparation and functionalization (Bonačić-Koutecký and Antoine, 2019; Yau et al., 2013). With scalable and precise synthesis, ultra-small AuNCs have been applied for bioimaging, biolabeling and more recently, theranostics (Cantelli et al., 2017; Katla et al., 2018; Nie et al., 2016; Zhang et al., 2018). Many studies performed with AuNC in non-primates show promise for applications in human non-transformed cells. Capitalizing on the tunability of AuNCs, varying sizes of AuNCs (e.g., Au_{10}, Au_{15}, Au_{18}, Au_{25}) with different surface compositions (e.g., GSH, PEG, NAC) AuNC, we investigated their effects in primary human astrocytes. Astrocytes are the most abundant glial cells in the brain, and they play substantial roles in brain physiology and pathology (Matias et al., 2018; Vainchtein and Molofsky, 2020; Westergard and Rothstein, 2020). We investigated non-transformed human astrocytes under "homeostatic" and stress conditions.

Accessibility of gold atoms, which is dependent on size, can allow the shuttling of electrons directly to gold nanostructures (Lee et al., 2012; Malel and Mandler, 2019). Gold nanostructures of approximately 1 nm in size show catalytic activity, which were not present in larger nanoparticles (Kizling et al., 2018). Water penetration is an indirect probe of the accessibility to gold in ligated nanoclusters. Analysis of water molecules penetration shows that smaller size clusters, with water molecules approaching very close to the cluster core (up to 3 ångström), are more open to engage in biological mechanisms versus the larger ones. Our findings show that, again, size of nanoclusters matters for such accessibility (and possibly in their mediation of enzymatic processes).

We induced mild oxidative stress using BSO, and a more powerful one by MenD. BSO is a pro-oxidant agent which impedes glutathione synthesis by inhibiting γ-

glutamylcysteine synthetase. Several studies have shown successful depletion of reduced glutathione levels by BSO in astrocytes (Bhatia et al., 2019; Macco et al., 2013). MenD is another oxidizing agent with a different mode of action. MenD is a strong generator of reactive oxygen species, mainly produced through redox cycling (Hollensworth et al., 2000). Both BSO and MenD served as pharmacological tools to disrupt redox homeostasis of human astrocytes in this study.

Some nanostructures can induce oxidative stress and toxicity by involving different stress pathways (Manke et al., 2013b). Our studies tested AuNC of different sizes to show if some critical transcription factors are engaged. The results show that AuNCs have an early effect on the activation of Nrf2 in primary human astrocytes. This effect on Nrf2 nuclear translocation was also previously observed in human glioblastoma cells treated with $Au_{15}SG_{13}$ or $Au_{25}SG_{18}$. Consistent with our previous study, a one-hour treatment with AuNCs was sufficient to induce a transient Nrf2 activation in glioblastoma (Maysinger et al., 2020).

Complementary to Nrf2 activation, human astrocytes also showed redistribution of HMGB1. This transcription factor is an alarmin protein whose distribution and redox status are tightly interconnected. HMGB1 in the nucleus is a chaperone, but in the extracellular compartment, it is mostly deleterious to the cells (Kang et al., 2014). Results from our current studies support such a notion showing that the protective effects of AuNC were associated with HMGB1 location as maintained in the nuclei. In contrast, extracellular and cytoplasmic HMGB1 are not protective and often cause deterioration of cell functions (Kang et al., 2014; Kigerl et al., 2018). Future studies will be dedicated to assessing changes in HMGB1 release into the extracellular matrix. Aside from HMGB1 in the nucleus acting as a chaperone, there are cytoplasmic proteins which function as chaperones (Buchner, 2019). We investigated heat shock protein 70 (HSP70).

Heat shock proteins (HSP) are crucial molecular chaperones that function to reduce proteotoxicity. Abundance of HSP70 was previously used as biomarker of the severity of cellular stress conditions. The HSP70 activation in human astrocytes differs from that of Nrf2; although Nrf2 activation was induced within one-hour treatment with AuNCs, there was no accompanied increase in HSP70 abundance. On the contrary, there was a decrease in intracellular HSP70 abundance suggesting that AuNCs do not cause significant proteotoxic

stress in human astrocytes, at least not during short treatment periods. However, an important consideration is that, under certain conditions, HSP70 can also be released extracellularly. Release of HSP70 has been proposed as a mechanism for glial cells to protect vulnerable neighbouring cells (Pockley and Henderson, 2018). The decrease in intracellular HSP70 could also result of astrocytes maintaining cellular homeostasis of its own and neighbouring cells. Collectively, results in this study show the modulation of Nrf2, HMGB1 and HSP70 cytoprotective pathways in astrocytes under mild and severe oxidative stress by AuNC.

Related with the modulatory effects of AuNC on redox-responsive transcription factors are modulations of organelles including mitochondria, lysosomes, and lipid droplets. Nrf2 targets a network of cytoprotective genes affecting mitochondrial respiration (Holmström et al., 2016). Mitochondria are responsible for energy production and maintenance of cellular homeostasis. However, these organelles are also potentially detrimental sources of ROS. In all conditions, there was an increased mitochondrial membrane permeability due to a decreased mitochondrial membrane potential as revealed with MitoTracker Deep Red labeling. Cells treated with any AuNC studied here showed an increased number of elongated mitochondria, suggesting a re-balancing of mitochondrial fusion and fission events. A re-balancing of mitochondrial morphology and membrane potential suggest a protective measure to reduce mitochondrial ROS formation and re-setting the redox status to survive (Eisner et al., 2018).

ROS can damage biomolecules, including lipids. A major product of lipid peroxidation is 4-hydroxynonenal (4-HNE), and its accumulation can induce or promote oxidative stress. Human astrocytes treated with AuNCs have maintained or reduced levels of 4-HNE. Given these results, we hypothesized that the decrease in peroxidised lipids could result from their sequestration in lipid droplets that could explain a protective role of lipid droplets in human astrocytes treated with AuNC. Such an interpretation is in line with the sequestration of oxidized lipids into lipid droplets limiting lipotoxicity in cancer cells, and drosophila neural cells (Jarc and Petan, 2019, 2020; Welte and Gould, 2017).

Our results suggest an alternative or additional interpretation: AuNC could engage other mechanisms for the reduction in 4-HNE accumulation. For example, the prevention of 4-HNE accumulation may be linked to the lysosomal degradation system. Lysosomes act as cellular waste disposal machinery, which degrade subcellular components, including

mitochondria, lipid droplets and other toxic cellular products. AuNCs have previously been shown to affect lysosomal distribution, acidity, and degradative capacity in human glioblastoma cells (Maysinger et al., 2020). Lysosomal activity could have been promoted in AuNC-treated human astrocytes, as it was in human glioblastoma cells. Lysosomes are essential for lipophagy which must be controlled to maintain physiological cellular functions (Settembre and Ballabio, 2014; Singh et al., 2009). Indeed, dysregulated lipophagy was suggested for neurodegenerative changes in the neural cells (Liu et al., 2015).

Collectively, findings in this study show that AuNC of larger sizes, particularly Au_{25}PEG and $Au_{25}AcCys_{18}$, are consistently protective in conditions of mild oxidative stress. These AuNC successfully induced the early activation of Nrf2. Such activation promotes glutathione synthesis, expression, and activity of antioxidant/stress-responsive enzymes (Hayes and Dinkova-Kostova, 2014; Robledinos-Antón et al., 2019b). Larger AuNCs also promoted lipid droplet formation, which is a protective mechanism to mitigate lipid peroxidation (Thiam and Dugail, 2019). This increase in lipid droplet number could be an explanation for the reduction in lipid peroxidation products, 4-HNE. However, in severe conditions of oxidative stress, as the case for treatments with MenD, their ability to induce Nrf2 activation does not suffice to reduce by-products of excessive ROS.

3.4. Conclusions

Our study highlights the importance of tailoring AuNCs by the appropriate size and surface ligand, as these are important characteristics in determining their pro- or antioxidant role. Redox status of human astrocytes is modulated by AuNCs in a size-dependent manner. Three key players, Nrf2, HMGB1 and HSP70, were identified to participate in protective mechanisms triggered in response to AuNCs. Disruption of cellular homeostasis induced the reorganization of subcellular components, including mitochondria and lipid droplets. Our findings suggest that sublethal concentrations of AuNCs of different sizes for a short exposure can disrupt organellar homeostasis or re-establish it by relocation and activation of several stress responsive transcription factors in human astrocytes as illustrated in **Fig. 5**.

We have yet to elucidate the effects of the AuNC-induced stress responses in human astrocytes to neighboring neural cells. Activation of stress responses may not only affect astrocyte homeostasis but also that of surrounding cells, such as neurons and microglia (Vainchtein and Molofsky, 2020). Microglia, being specialized macrophages, survey the

central nervous system and can internalize nanostructures (Choi et al., 2010). Astrocytes and microglia maintain close contacts and are constantly involved in bi-and multi-directional communication. Such studies combined with time lapse experiments and proteomic analyses including post-translational modifications of the studied proteins are warranted in more complex models with human glial cells and neurons, e.g., cerebral organoids (Di Lullo and Kriegstein, 2017).

3.5. Experimental section

Materials. For AuNC synthesis and characterisation, all chemicals were commercially available and were used without purification. $HAuCl_4 \cdot 3H_2O$, acetic acid, triethylamine, tributylamine, diethyl ether, methanol (HPLC grade), N-acetyl-L-cysteine and GSH (γ-Glu-Cys-Gly, MW 307 Da) were purchased from Carl Roth. Borane trimethylamine complex, tetrabutylammonium borohydride, tetramethylammonium borohydride were purchased from Sigma Aldrich. MilliQ water with a resistivity of 18.2 MΩ cm was used for all experiments. For biological experiments: Dulbecco's modified eagle medium (DMEM) high glucose (Sigma-Aldrich, D5648), GlutaMAX (Thermofisher, 35050061), L-buthionine sulfoximine (Sigma–Aldrich), menadione (Sigma-Aldrich), lipopolysaccharide (Sigma-Aldrich), dimethyl sulfoxide (Sigma–Aldrich), paraformaldehyde (Sigma–Aldrich), Hoechst 33342 (Sigma–Aldrich), BODIPY 493/503 (Invitrogen), MitoTracker Deep Red FM (Thermofisher, M22426), 3-[4,5-dimethylthiazol-2-yl]-2,5-diphenyl tetrazolium bromide (Sigma-Aldrich), Alexa Fluor 488 Phalloidin (Invitrogen), Aqua-Poly/Mount medium (Polysciences), and EveryBrite mounting medium (Biotium, 23001) were used as received. Primary antibodies against the following antigens were used: Nrf2 (Abcam, ab31163, diluted 1:500), HSP70 (Enzo Life Sciences, SPA-822, dilute 1:1000), 4-hydroxynonenal (Abcam, ab46545, diluted 1:500), HMGB1 (Abcam, ab18256, diluted 1:1000). Secondary antibodies were used: Alexa Fluor 647 anti-rabbit IgG (Invitrogen, A21244, diluted 1:500), and Alexa Fluor 488 anti-mouse IgG (Invitrogen, A28175, diluted 1:500).

Synthesis of AuNCs. $Au_{10}SG_{10}$ was synthesized as reported by Bertorelle et al (Bertorelle et al., 2017). $Au_{15}SG_{13}$ was synthesized as reported by Russier-Antoine et al (Russier-Antoine et al., 2014). $Au_{18}SG_{14}$ was synthesized as reported in refs. (Bertorelle et al., 2018; Soleilhac et al., 2017) $Au_{25}SG_{18}$ was synthesized as reported by Ji et al (Ji et al., 2019). Au_{15}PEG and Au_{25}PEG were synthesized as reported by Maysinger et al (Maysinger et al.,

2020). For all synthesis, the as-obtained precipitates were then repeatedly washed with excess methanol and dried under vacuum to yield Au nanoclusters in powder form. As mentioned in Introduction, while atomically precise gold clusters were synthesized with L-cysteine (Russier-Antoine et al., 2014; Yuan et al., 2012), to our knowledge, it was not the case for NAC as ligands.

Synthesis of $Au_{25}(AcCys)_{18}$. 100 mg of gold salts ($HAuCl_4,3H_2O$) were added to a solution of NAC (234 mg) dissolved in methanol (35 mL), tributylamine (2 mL) and triethylamine (2 mL). After stirring for 5 minutes at room temperature, a first reducing agent was added (tetrabutylammonium borohydride, 3x25 mg spaced by 30 min). Then water (15 mL) and diethyl ether (15 mL) were added, followed by the addition of a second reducing agent (tetramethylammonium borohydride, 4x50 mg spaced by 30 min). The solution was left undisturbed overnight before purification. Precipitation was induced by adding NH_4OH (1 mL, 10%) and solution was centrifuged. The unwanted products were removed with cycles of dissolution/precipitation/centrifugation. The powder was dissolved in a minimum of H_2O/NH_4OH then precipitated with MeOH. After centrifugation, the powder was dissolved again in water (10 mL). Then glacial acetic acid (2 mL) was added, and solution was left undisturbed 1 hour before being centrifuged. The supernatant was collected and precipitated with MeOH. A last cycle of dissolution/precipitation with H_2O/NH_4OH and MeOH was done before drying the powder under vacuum. Typically, more than 74 mg of high purity $Au_{25}AcCys_{18}$ were collected.

Characterization of AuNCs. The as-prepared AuNC were characterized by mass spectrometry. The mono-dispersity in terms of the size of the prepared gold clusters was verified by electrospray ionization (ESI) on a commercial quadrupole time-of-flight (micro-qTOF, Bruker-Daltonics, Bremen, Germany, mass resolution ∼10 000).

Human primary astrocytes. Human fetal astrocytes were isolated as previously described (Rothhammer et al., 2016, 2017) from 17–23 weeks of gestation age fetal brain tissue specimens obtained from the Birth Defects Research Laboratory at the University of Washington Dept. of Pediatrics (Project Number: 5R24HD000836–51) following Canadian Institutes of Health Research-approved guidelines. The sex of the human fetal astrocytes used is unknown.

Cell culture and treatments. Primary human astrocytes were seeded in serum-supplemented medium (DMEM, high glucose, glutaMAX, 10% fetal bovine serum, 1% penicillin-streptomycin). Cells were seeded at the appropriate density as indicated for specific assays. Primary human astrocytes were treated with AuNC of varying sizes and ligands ($Au_{10}SG_{10}$, $Au_{15}SG_{13}$, $Au_{15}PEG$, $Au_{18}SG_{14}$, $Au_{25}SG_{18}$, $Au_{25}PEG$, or $Au_{25}AcCys_{18}$) with or without pharmacological agents (L-buthionine sulfoximine (100 μM, BSO) or menadione (25 μM, MenD)) at indicated concentrations for a specified length of time (1h or 24h). Treatments include a "vehicle" control, in which cells were exposed to the vehicle in which AuNCs or pharmacological agent was dissolved or dispersed.

Cell counting. Cells were seeded in 96-well plates at a density of 5,000 cells per well in serum-supplemented medium (DMEM, high glucose, glutaMAX, 10% fetal bovine serum, 1% penicillin-streptomycin). Cells were left to adhere for 48 hours at 37°C with 5% CO2 and 95% relative humidity. After 48 hours, cells were washed with PBS and treated for 24 hours with AuNCs or pharmacological agents in serum-deprived medium. Wells were sampled in triplicates. Cell viability was assessed by cell counting. Following treatments, cells were fixed with paraformaldehyde (PFA, 4%) for 10 minutes. Nuclei were labeled with Hoechst 33342 (10 μM, 10 min) and imaged with a Leica DMI4000B fluorescence microscope. Cell counting was performed with ImageJ software.

Fluorescence microscopy and immunocytochemistry. Human astrocytes were plated onto poly-*D*-lysine (PDL)-coated glass coverslips (12 mm diameter) at 5,000 cells per coverslip and left to adhere. Cells were treated as indicated in serum-deprived media. Following incubation with dyes, cells were washed twice with phosphate buffered saline (PBS) and imaged live. For immunocytochemistry, treated cells were fixed in PFA (4%) at room temperature for 10 minutes and permeabilized with Triton X-100 (0.1%) in PBS for another 10 minutes at room temperature. After permeabilization, cells were blocked for 1 hour in goat serum (10%). Cells were washed three times for five minutes with PBS, before being incubated overnight with primary antibodies at 4°C. The following day, cells were washed three times for five minutes, incubated with secondary antibodies for 1 hour at room temperature, and washed again in PBS. Nuclei were labeled with Hoechst 33342 (10 μM, 10 min), and F-actin was identified with Alexa Fluor 488 Phalloidin (1:50, 20 min). Cells were mounted on glass

slides with Aqua-Poly/Mount medium. Cells were imaged using a Leica DMI4000B fluorescence microscope.

Measurement of intracellular ROS with CellROX Deep Red. Human astrocytes were treated with AuNC (10 μM, 24h) in serum-deprived media in the absence or presence of menadione (25 μM, 24h). Thirty minutes prior to the end of the treatment period, CellROX Deep Red (5 μM, 30 min) was added directly to cells. Following incubation with reagent, media was aspirated. Cells were lysed using dimethyl sulfide and collected. Fluorescence intensities were measured with TECAN SPARK10M microplate reader (excitation: 635 nm, bandwidth 35 nm; emission: 680 nm, bandwidth 30 nm).

Mitochondrial staining with MitoTracker Deep Red FM. Human astrocytes were treated with AuNC (10 μM, 24h) in serum-deprived media. Twenty minutes prior to the end of the treatment period, MitoTracker Deep Red FM (200 nM, 20 min) and Hoechst 33342 (10 μM 20 min) was added directly to cells. Following incubation with mitochondrial dye, cells were washed, and fixed with PFA (4%).

Staining of neutral lipid droplets with BODIPY 493/503. Human astrocytes were treated with AuNC (10 μM, 24h) in serum-deprived media. Cells were fixed with 4% PFA for 10 minutes and washed three times for fives minutes with PBS at room temperature. Lipid droplets were labeled using BODIPY 493/503 (10 μM, 10 min), and nuclei using Hoechst 33342 (10 μM, 10 min). Cells were washed three times for 5 minutes, and mounted on glass slides with EverBrite mounting medium.

Quantification of lipid droplet number and positioning. Lipid droplets were counted using ImageJ software. To measure lipid droplet position, X-Y coordinates were obtained from images from both lipid droplet and center of nucleus. Distance (D) between points P1 (x_1, y_1) and P2 (x_2, y_2) was measured based on their coordinates using the following equation:

$$D = \sqrt{(x_2 - x_1)^2 + (y_2 - y_1)^2} \qquad (1)$$

Computational details. The structural properties of ligated gold clusters including the 500 water molecules have been determined using QM/MM method (Buceta et al., 2015) (two-layer ONIOM method (Dapprich et al., 1999) implemented in Gaussian (Frisch, 2016)) employing the PM7 (Stewart, 2013) in QM for ligated gold clusters and UFF (Rappe et al., 1992) force field for water molecules in MM. Since PM7 is semiempirical method the gold core and sulfur atoms from glutathione molecules have been fixed according to

previously obtained density functional theory (DFT) structures (Bertorelle et al., 2017; Das et al., 2015; Jiang et al., 2013; Zhu et al., 2008). Radial distribution of the density of water molecules was obtained using R-studio software (RStudio Team, 2020).

Statistical analysis. Student's t-test was used for statistical analysis. A p value of less than 0.05 was identified as statistically significant and indicated in figures as follows: *p<0.05, **p<0.01, ***p<0.001.

Data availability. Data files are available at the Open Science Framework, https://osf.io/7zmcv/.

3.6. Conflicts of interest

The authors declare no conflict of interest.

3.7. Acknowledgements

This research was supported by the project STIM-REI, Contract Number: KK.01.1.1.01.0003, funded by the European Union through the European Regional Development Fund – the Operational Programme Competitiveness and Cohesion 2014–2020 (KK.01.1.1.01). M.P.B., Ž.S.M. and V.B.K. acknowledge computational facilities of the HPC computer within the STIM-REI project. These studies were supported by the Canadian Institute for Health Research (D.M.), Natural Sciences and Engineering Research (D.M.), and McGill University for contributing to the internal fellowship of E.R.G. We also wish to thank the Give & Grow Foundation for E.R.G.'s scholarship award.

3.8. References

Aït-Aïssa, S., Pandard, P., Magaud, H., Arrigo, A.-P., Thybaud, E., and Porcher, J.-M. (2003). Evaluation of an in vitro hsp70 induction test for toxicity assessment of complex mixtures: comparison with chemical analyses and ecotoxicity tests. Ecotoxicology and Environmental Safety *54*, 92–104.

Andersson, U., Yang, H., and Harris, H. (2018a). High-mobility group box 1 protein (HMGB1) operates as an alarmin outside as well as inside cells. Semin. Immunol. *38*, 40–48.

Andersson, U., Yang, H., and Harris, H. (2018b). Extracellular HMGB1 as a therapeutic target in inflammatory diseases. Expert Opin. Ther. Targets *22*, 263–277.

Bertorelle, F., Russier-Antoine, I., Calin, N., Comby-Zerbino, C., Bensalah-Ledoux, A., Guy, S., Dugourd, P., Brevet, P.-F., Sanader, Ž., Krstić, M., et al. (2017). Au10(SG)10: A Chiral Gold Catenane Nanocluster with Zero Confined Electrons. Optical Properties and First-Principles Theoretical Analysis. J. Phys. Chem. Lett. *8*, 1979–1985.

Bertorelle, F., Moulin, C., Soleilhac, A., Comby-Zerbino, C., Dugourd, P., Russier-Antoine, I., Brevet, P.-F., and Antoine, R. (2018). Bulky Counterions: Enhancing the Two-Photon Excited Fluorescence of Gold Nanoclusters. Chemphyschem *19*, 165–168.

Bhatia, T.N., Pant, D.B., Eckhoff, E.A., Gongaware, R.N., Do, T., Hutchison, D.F., Gleixner, A.M., and Leak, R.K. (2019). Astrocytes Do Not Forfeit Their Neuroprotective Roles After Surviving Intense Oxidative Stress. Front. Mol. Neurosci. *12*.

Bonačić-Koutecký, V., and Antoine, R. (2019). Enhanced two-photon absorption of ligated silver and gold nanoclusters: theoretical and experimental assessments. Nanoscale *11*, 12436–12448.

Buceta, D., Busto, N., Barone, G., Leal, J.M., Domínguez, F., Giovanetti, L.J., Requejo, F.G., García, B., and López-Quintela, M.A. (2015). Ag2 and Ag3 clusters: synthesis, characterization, and interaction with DNA. Angew. Chem. Int. Ed. Engl. *54*, 7612–7616.

Buchner, J. (2019). Molecular chaperones and protein quality control: an introduction to the JBC Reviews thematic series. J Biol Chem *294*, 2074–2075.

Cantelli, A., Guidetti, G., Manzi, J., Caponetti, V., and Montalti, M. (2017). Towards Ultra-Bright Gold Nanoclusters. European Journal of Inorganic Chemistry *2017*, 5068–5084.

Chakraborty, I., and Pradeep, T. (2017). Atomically Precise Clusters of Noble Metals: Emerging Link between Atoms and Nanoparticles. Chem. Rev. *117*, 8208–8271.

Choi, J., Zheng, Q., Katz, H.E., and Guilarte, T.R. (2010). Silica-based nanoparticle uptake and cellular response by primary microglia. Environ. Health Perspect. *118*, 589–595.

Dan Dunn, J., Alvarez, L.A., Zhang, X., and Soldati, T. (2015). Reactive oxygen species and mitochondria: A nexus of cellular homeostasis. Redox Biol *6*, 472–485.

Dapprich, S., Komáromi, I., Byun, K.S., Morokuma, K., and Frisch, M.J. (1999). A new ONIOM implementation in Gaussian98. Part I. The calculation of energies, gradients, vibrational frequencies and electric field derivatives. Journal of Molecular Structure: THEOCHEM *461–462*, 1–21.

Das, A., Liu, C., Byun, H.Y., Nobusada, K., Zhao, S., Rosi, N., and Jin, R. (2015). Structure determination of [Au18(SR)14]. Angew. Chem. Int. Ed. Engl. *54*, 3140–3144.

Deng, H.-H., Wu, G.-W., Zou, Z.-Q., Peng, H.-P., Liu, A.-L., Lin, X.-H., Xia, X.-H., and Chen, W. (2015). pH-Sensitive gold nanoclusters: preparation and analytical applications for urea, urease, and urease inhibitor detection. Chem. Commun. (Camb.) *51*, 7847–7850.

Di Lullo, E., and Kriegstein, A.R. (2017). The use of brain organoids to investigate neural development and disease. Nature Reviews Neuroscience *18*, 573–584.

Du, X., and Jin, R. (2019). Atomically Precise Metal Nanoclusters for Catalysis. ACS Nano *13*, 7383–7387.

Du, B., Jiang, X., Das, A., Zhou, Q., Yu, M., Jin, R., and Zheng, J. (2017). Glomerular barrier behaves as an atomically precise bandpass filter in a sub-nanometre regime. Nat Nanotechnol *12*, 1096–1102.

Eisner, V., Picard, M., and Hajnóczky, G. (2018). Mitochondrial dynamics in adaptive and maladaptive cellular stress responses. Nature Cell Biology *20*, 755–765.

Fang, P., Schachner, M., and Shen, Y.-Q. (2012). HMGB1 in Development and Diseases of the Central Nervous System. Mol Neurobiol *45*, 499–506.

Griffith, A.A., and Holmes, W. (2019). Fine Tuning: Effects of Post-Translational Modification on Hsp70 Chaperones. Int J Mol Sci *20*.

Gülke, E., Gelderblom, M., and Magnus, T. (2018). Danger signals in stroke and their role on microglia activation after ischemia. Ther Adv Neurol Disord *11*.

Hayes, J.D., and Dinkova-Kostova, A.T. (2014). The Nrf2 regulatory network provides an interface between redox and intermediary metabolism. Trends in Biochemical Sciences *39*, 199–218.

Healy, L.M., Yaqubi, M., Ludwin, S., and Antel, J.P. (2020). Species differences in immune-mediated CNS tissue injury and repair: A (neuro)inflammatory topic. Glia *68*, 811–829.

Herker, E., and Ott, M. (2012). Emerging Role of Lipid Droplets in Host/Pathogen Interactions. J. Biol. Chem. *287*, 2280–2287.

Hollensworth, S.B., Shen, C., Sim, J.E., Spitz, D.R., Wilson, G.L., and LeDoux, S.P. (2000). Glial cell type-specific responses to menadione-induced oxidative stress. Free Radic. Biol. Med. *28*, 1161–1174.

Holmström, K.M., Kostov, R.V., and Dinkova-Kostova, A.T. (2016). The multifaceted role of Nrf2 in mitochondrial function. Curr Opin Toxicol *1*, 80–91.

Jarc, E., and Petan, T. (2019). Lipid Droplets and the Management of Cellular Stress. Yale J Biol Med *92*, 435–452.

Jarc, E., and Petan, T. (2020). A twist of FATe: Lipid droplets and inflammatory lipid mediators. Biochimie *169*, 69–87.

Ji, J., Moquin, A., Bertorelle, F., Ky Chang, P., Antoine, R., Luo, J., McKinney, R.A., and Maysinger, D. (2019). Organotypic and primary neural cultures as models to assess effects of different gold nanostructures on glia and neurons. Nanotoxicology *13*, 285–304.

Jiang, D., Overbury, S.H., and Dai, S. (2013). Structure of Au15(SR)13 and Its Implication for the Origin of the Nucleus in Thiolated Gold Nanoclusters. J. Am. Chem. Soc. *135*, 8786–8789.

Jin, R., Zeng, C., Zhou, M., and Chen, Y. (2016). Atomically Precise Colloidal Metal Nanoclusters and Nanoparticles: Fundamentals and Opportunities. Chem. Rev. *116*, 10346–10413.

Kang, R., Chen, R., Zhang, Q., Hou, W., Wu, S., Cao, L., Huang, J., Yu, Y., Fan, X., Yan, Z., et al. (2014). HMGB1 in health and disease. Molecular Aspects of Medicine *40*, 1–116.

Kang, X., Chong, H., and Zhu, M. (2018). Au25(SR)18: the captain of the great nanocluster ship. Nanoscale *10*, 10758–10834.

Katla, S.K., Zhang, J., Castro, E., Bernal, R.A., and Li, X. (2018). Atomically Precise Au25(SG)18 Nanoclusters: Rapid Single-Step Synthesis and Application in Photothermal Therapy. ACS Appl Mater Interfaces *10*, 75–82.

Kigerl, K.A., Lai, W., Wallace, L.M., Yang, H., and Popovich, P.G. (2018). High mobility group box-1 (HMGB1) is increased in injured mouse spinal cord and can elicit neurotoxic inflammation. Brain Behav Immun *72*, 22–33.

Kizling, M., Dzwonek, M., Więckowska, A., and Bilewicz, R. (2018). Size Does Matter—Mediation of Electron Transfer by Gold Clusters in Bioelectrocatalysis. ChemCatChem *10*, 1988–1992.

Kroemer, G., and Jäättelä, M. (2005). Lysosomes and autophagy in cell death control. Nature Reviews Cancer *5*, 886–897.

Lee, S., Ringstrand, B.S., Stone, D.A., and Firestone, M.A. (2012). Electrochemical Activity of Glucose Oxidase on a Poly(ionic liquid)–Au Nanoparticle Composite. ACS Appl. Mater. Interfaces *4*, 2311–2317.

Lemasters, J.J. (2005). Selective mitochondrial autophagy, or mitophagy, as a targeted defense against oxidative stress, mitochondrial dysfunction, and aging. Rejuvenation Res *8*, 3–5.

Lewis, S., Handy, R.D., Cordi, B., Billinghurst, Z., and Depledge, M.H. (1999). Stress proteins (HSP's): Methods of Detection and Their Use as an Environmental Biomarker. Ecotoxicology *8*, 351–368.

Libbing, C.L., McDevitt, A.R., Azcueta, R.-M.P., Ahila, A., and Mulye, M. (2019). Lipid Droplets: A Significant but Understudied Contributor of Host–Bacterial Interactions. Cells *8*.

Liddell, J.R. (2017). Are Astrocytes the Predominant Cell Type for Activation of Nrf2 in Aging and Neurodegeneration? Antioxidants (Basel) *6*.

Liu, L., Zhang, K., Sandoval, H., Yamamoto, S., Jaiswal, M., Sanz, E., Li, Z., Hui, J., Graham, B.H., Quintana, A., et al. (2015). Glial Lipid Droplets and ROS Induced by Mitochondrial Defects Promote Neurodegeneration. Cell *160*, 177–190.

Lotze, M.T., and Tracey, K.J. (2005). High-mobility group box 1 protein (HMGB1): nuclear weapon in the immune arsenal. Nat. Rev. Immunol. *5*, 331–342.

M. J. Frisch, G. W. Trucks, H. B. Schlegel, G. E. Scuseria, M. A. Robb, J. R. Cheeseman, G. Scalmani, V. Barone, G. A. Petersson, H. Nakatsuji, X. Li, M. Caricato, A. V. Marenich, J. Bloino, B. G. Janesko, R. Gomperts, B. Mennucci, H. P. Hratchian, J. V. Ortiz, A. F. Izmaylov, J. L. Sonnenberg, D. Williams-Young, F. Ding, F. Lipparini, F. Egidi, J. Goings, B. Peng, A. Petrone, T. Henderson, D. Ranasinghe, V. G. Zakrzewski, J. Gao, N. Rega, G. Zheng, W. Liang, M. Hada, M. Ehara, K. Toyota, R. Fukuda, J. Hasegawa, M. Ishida, T. Nakajima, Y. Honda, O. Kitao, H. Nakai, T. Vreven, K. Throssell, J. A. Montgomery, Jr., J. E. Peralta, F. Ogliaro, M. J. Bearpark, J. J. Heyd, E. N. Brothers, K. N. Kudin, V. N. Staroverov, T. A. Keith, R. Kobayashi, J. Normand, K. Raghavachari, A. P. Rendell, J. C. Burant, S. S. Iyengar, J. Tomasi, M. Cossi, J. M. Millam, M. Klene, C. Adamo, R. Cammi, J. W. Ochterski, R. L. Martin, K. Morokuma, O. Farkas, J. B. Foresman, and D. J. Fox (2016). Gaussian 16, Revision C.01 (Wallingford CT: Gaussian, Inc.).

Macco, R., Pelizzoni, I., Consonni, A., Vitali, I., Giacalone, G., Martinelli Boneschi, F., Codazzi, F., Grohovaz, F., and Zacchetti, D. (2013). Astrocytes acquire resistance to iron-dependent oxidative stress upon proinflammatory activation. Journal of Neuroinflammation *10*, 897.

Malel, E., and Mandler, D. (2019). Direct Electron Transfer between Glucose Oxidase and Gold Nanoparticles; When Size Matters. ChemElectroChem *6*, 147–154.

Manke, A., Wang, L., and Rojanasakul, Y. (2013a). Mechanisms of nanoparticle-induced oxidative stress and toxicity. Biomed Res Int *2013*, 942916.

Manke, A., Wang, L., and Rojanasakul, Y. (2013b). Mechanisms of Nanoparticle-Induced Oxidative Stress and Toxicity. BioMed Research International.

Matias, D., Balça-Silva, J., da Graça, G.C., Wanjiru, C.M., Macharia, L.W., Nascimento, C.P., Roque, N.R., Coelho-Aguiar, J.M., Pereira, C.M., Dos Santos, M.F., et al. (2018). Microglia/Astrocytes–Glioblastoma Crosstalk: Crucial Molecular Mechanisms and Microenvironmental Factors. Front. Cell. Neurosci. *12*.

Maysinger, D., Gran, E.R., Bertorelle, F., Fakhouri, H., Antoine, R., Kaul, E.S., Samhadaneh, D.M., and Stochaj, U. (2020). Gold nanoclusters elicit homeostatic perturbations in glioblastoma cells and adaptive changes of lysosomes. Theranostics *10*, 1633–1648.

Nie, L., Xiao, X., and Yang, H. (2016). Preparation and Biomedical Applications of Gold Nanocluster. Journal of Nanoscience and Nanotechnology *16*, 8164–8175.

Olzmann, J.A., and Carvalho, P. (2019). Dynamics and functions of lipid droplets. Nat. Rev. Mol. Cell Biol. *20*, 137–155.

Palikaras, K., Lionaki, E., and Tavernarakis, N. (2018). Mechanisms of mitophagy in cellular homeostasis, physiology and pathology. Nature Cell Biology *20*, 1013–1022.

Pockley, A.G., and Henderson, B. (2018). Extracellular cell stress (heat shock) proteins—immune responses and disease: an overview. Philosophical Transactions of the Royal Society B: Biological Sciences *373*, 20160522.

Porret, E., Guével, X.L., and Coll, J.-L. (2020). Gold nanoclusters for biomedical applications: toward in vivo studies. Journal of Materials Chemistry B *8*, 2216–2232.

Rappe, A.K., Casewit, C.J., Colwell, K.S., Goddard, W.A., and Skiff, W.M. (1992). UFF, a full periodic table force field for molecular mechanics and molecular dynamics simulations. J. Am. Chem. Soc. *114*, 10024–10035.

Reeves, R. (2010). Nuclear functions of the HMG proteins. Biochimica et Biophysica Acta (BBA) - Gene Regulatory Mechanisms *1799*, 3–14.

Robledinos-Antón, N., Fernández-Ginés, R., Manda, G., and Cuadrado, A. (2019a). Activators and Inhibitors of NRF2: A Review of Their Potential for Clinical Development. Oxid Med Cell Longev *2019*, 9372182.

Robledinos-Antón, N., Fernández-Ginés, R., Manda, G., and Cuadrado, A. (2019b). Activators and Inhibitors of NRF2: A Review of Their Potential for Clinical Development.

Rothhammer, V., Mascanfroni, I.D., Bunse, L., Takenaka, M.C., Kenison, J.E., Mayo, L., Chao, C.-C., Patel, B., Yan, R., Blain, M., et al. (2016). Type I interferons and microbial metabolites of tryptophan modulate astrocyte activity and central nervous system inflammation via the aryl hydrocarbon receptor. Nature Medicine *22*, 586–597.

Rothhammer, V., Kenison, J.E., Tjon, E., Takenaka, M.C., de Lima, K.A., Borucki, D.M., Chao, C.-C., Wilz, A., Blain, M., Healy, L., et al. (2017). Sphingosine 1-phosphate receptor modulation suppresses pathogenic astrocyte activation and chronic progressive CNS inflammation. Proc Natl Acad Sci U S A *114*, 2012–2017.

RStudio Team (2020). RStudio: Integrated Development Environment for R. (Boston MA: RStudio, PBC.).

Russier-Antoine, I., Bertorelle, F., Vojkovic, M., Rayane, D., Salmon, E., Jonin, C., Dugourd, P., Antoine, R., and Brevet, P.-F. (2014). Non-linear optical properties of gold quantum clusters. The smaller the better. Nanoscale *6*, 13572–13578.

Settembre, C., and Ballabio, A. (2014). Lysosome: regulator of lipid degradation pathways. Trends Cell Biol *24*, 743–750.

Singh, R., Kaushik, S., Wang, Y., Xiang, Y., Novak, I., Komatsu, M., Tanaka, K., Cuervo, A.M., and Czaja, M.J. (2009). Autophagy regulates lipid metabolism. Nature *458*, 1131–1135.

Soleilhac, A., Bertorelle, F., Comby-Zerbino, C., Chirot, F., Calin, N., Dugourd, P., and Antoine, R. (2017). Size Characterization of Glutathione-Protected Gold Nanoclusters in the Solid, Liquid and Gas Phases. J. Phys. Chem. C *121*, 27733–27740.

Stewart, J.J.P. (2013). Optimization of parameters for semiempirical methods VI: more modifications to the NDDO approximations and re-optimization of parameters. J Mol Model *19*, 1–32.

Tang, Q., and Jiang, D. (2015). Revisiting Structural Models for Au18(SR)14. J. Phys. Chem. C *119*, 2904–2909.

Tang, D., Kang, R., Zeh, H.J., and Lotze, M.T. (2011). High-Mobility Group Box 1, Oxidative Stress, and Disease. Antioxid Redox Signal *14*, 1315–1335.

Thiam, A.R., and Dugail, I. (2019). Lipid droplet–membrane contact sites – from protein binding to function. J Cell Sci *132*.

Tremblay, M.-E., Zhang, I., Bisht, K., Savage, J.C., Lecours, C., Parent, M., Titorenko, V., and Maysinger, D. (2016). Remodeling of lipid bodies by docosahexaenoic acid in activated microglial cells. Journal of Neuroinflammation *13*, 116.

Vainchtein, I.D., and Molofsky, A.V. (2020). Astrocytes and Microglia: In Sickness and in Health. Trends in Neurosciences *43*, 144–154.

Vargas, M.R., Johnson, D.A., Sirkis, D.W., Messing, A., and Johnson, J.A. (2008). Nrf2 activation in astrocytes protects against neurodegeneration in mouse models of familial amyotrophic lateral sclerosis. J. Neurosci. *28*, 13574–13581.

Vasile, F., Dossi, E., and Rouach, N. (2017). Human astrocytes: structure and functions in the healthy brain. Brain Struct Funct *222*, 2017–2029.

Welte, M.A., and Gould, A.P. (2017). Lipid droplet functions beyond energy storage. Biochim Biophys Acta *1862*, 1260–1272.

Westergard, T., and Rothstein, J.D. (2020). Astrocyte Diversity: Current Insights and Future Directions. Neurochem Res.

Willems, P.H.G.M., Rossignol, R., Dieteren, C.E.J., Murphy, M.P., and Koopman, W.J.H. (2015). Redox Homeostasis and Mitochondrial Dynamics. Cell Metab. *22*, 207–218.

Yau, S.H., Varnavski, O., and Goodson, T. (2013). An Ultrafast Look at Au Nanoclusters. Acc. Chem. Res. *46*, 1506–1516.

Yu, Y., Chen, X., Yao, Q., Yu, Y., Yan, N., and Xie, J. (2013). Scalable and Precise Synthesis of Thiolated Au10–12, Au15, Au18, and Au25 Nanoclusters via pH Controlled CO Reduction. Chem. Mater. *25*, 946–952.

Yu, Y., Tang, D., and Kang, R. (2015). Oxidative stress-mediated HMGB1 biology. Front. Physiol. *6*.

Yuan, X., Yu, Y., Yao, Q., Zhang, Q., and Xie, J. (2012). Fast Synthesis of Thiolated Au25 Nanoclusters via Protection–Deprotection Method. J. Phys. Chem. Lett. *3*, 2310–2314.

Zhang, Q., Yang, M., Zhu, Y., and Mao, C. (2018). Metallic Nanoclusters for Cancer Imaging and Therapy. Curr Med Chem *25*, 1379–1396.

Zhang, X.-D., Luo, Z., Chen, J., Song, S., Yuan, X., Shen, X., Wang, H., Sun, Y., Gao, K., Zhang, L., et al. (2015). Ultrasmall glutathione-protected gold nanoclusters as next generation radiotherapy sensitizers with high tumor uptake and high renal clearance. Sci Rep *5*, 8669.

Zheng, F., and Li, H. (2019). Evaluation of Nrf2 with Exposure to Nanoparticles. Methods Mol. Biol. *1894*, 229–246.

Zhu, M., Aikens, C.M., Hollander, F.J., Schatz, G.C., and Jin, R. (2008). Correlating the crystal structure of a thiol-protected Au25 cluster and optical properties. J. Am. Chem. Soc. *130*, 5883–5885.

3.9.Figures

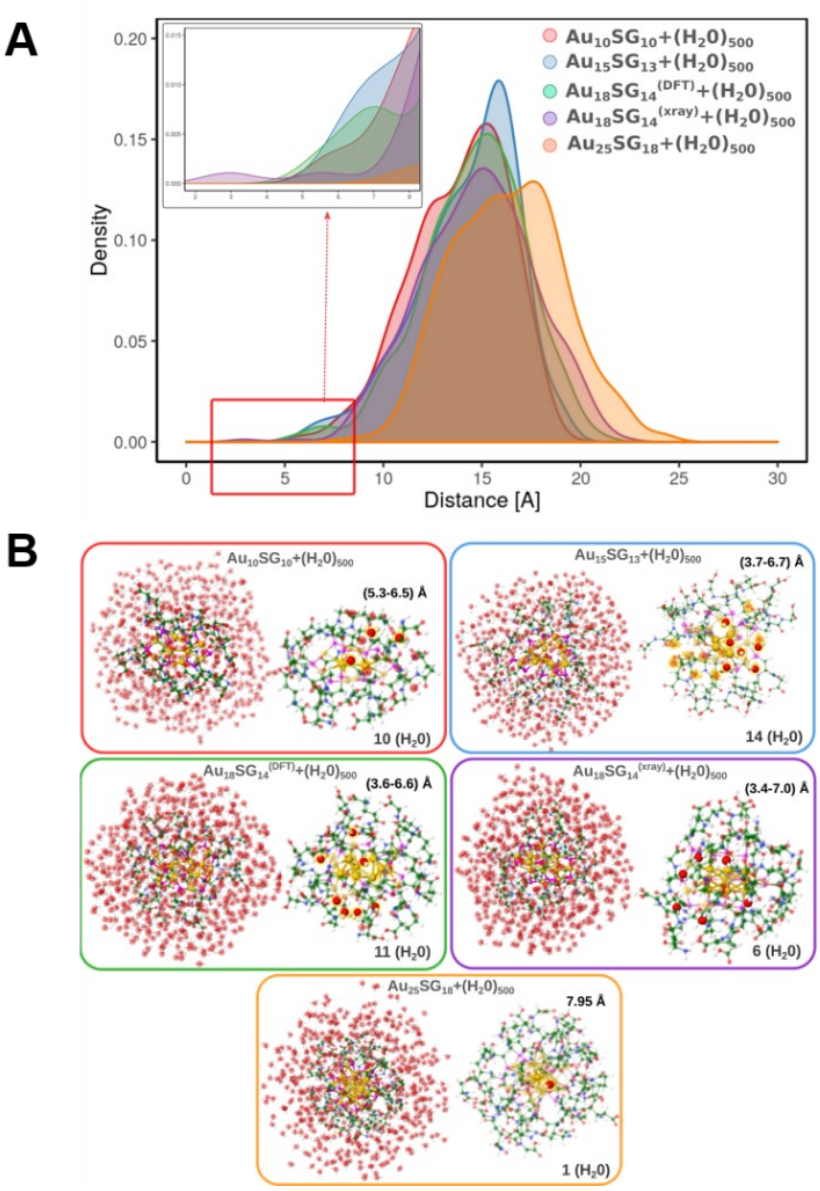

Figure 1. Density of water molecules as a function of radial distance from the central Au atom within ligated gold clusters. (A) $Au_{10}SG_{10}$ (red), $Au_{15}SG_{13}$ (blue), $Au_{18}SG_{14}$ (green and purple), and $Au_{25}SG_{18}$ (orange). 500 labels number of water molecules. Insert illustrates radial distance of water molecules in the range of 2-8 Å. (B) Structures of $Au_{10}SG_{10}$ (red), $Au_{15}SG_{13}$ (blue), $Au_{18}SG_{14}$ (green and purple), and $Au_{25}SG_{18}$ (orange) with 500 water molecules (left side). Water molecules located up to 8 Å distances are presented illustrating their penetration (right side).

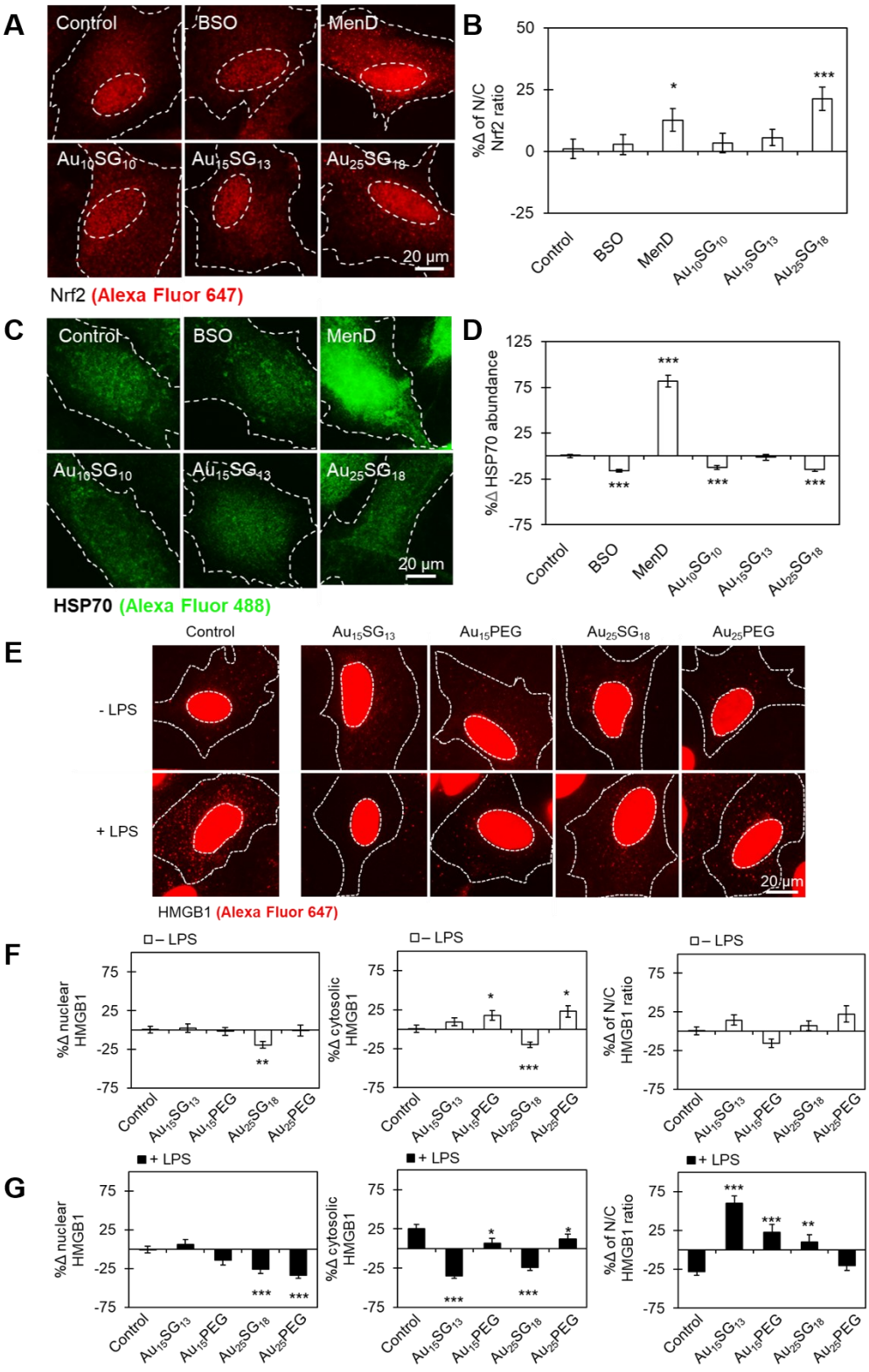

Figure 2. AuNCs exert redox sensitive cellular responses. (A-B) Primary human astrocytes were treated with 10 μM AuNC for 1 hour. Pharmacological inducers of oxidative stress were used as positive controls: 100 μM L-buthionine sulfoximine (BSO) or 25 μM menadione (MenD). (A-B)

Nrf2 and (C-D) Hsp70 cellular distribution were assessed by immunocytochemistry. Nuclei and/or cells are outlined. (B) Shown are percentage change of Nrf2 nuclear-to-cytoplasmic (N/C) ratio of mean fluorescence intensities per unit area (μm^2) ± SEM. Over 680 cells were analyzed in total (minimum 90 cells/condition). (D) Shown are percentage change of Hsp70 mean fluorescence intensities per unit area (μm^2) ± SEM. Over 690 cells were analyzed in total (minimum 95 cells/condition). (E-G) Primary human astrocytes were treated with 10 µM AuNC for 24 hours in the (F) absence or (G) presence of 1 ng/mL lipopolysaccharide (LPS). HMGB1 cellular distribution was assessed by antibody labelling. Nuclei and cells are outlined. Shown are percentage change of fluorescence intensities in the nucleus per area (μm^2), cytoplasm per area (μm^2) and the ratio nuclear/cytoplasmic fluorescence (N/C) ± SEM. Over 800 cells were analyzed in total (minimum 70 cells/condition). A p value of less than 0.05 was identified as statistically significant as follows: *$p<0.05$, **$p<0.01$, ***$p<0.001$.

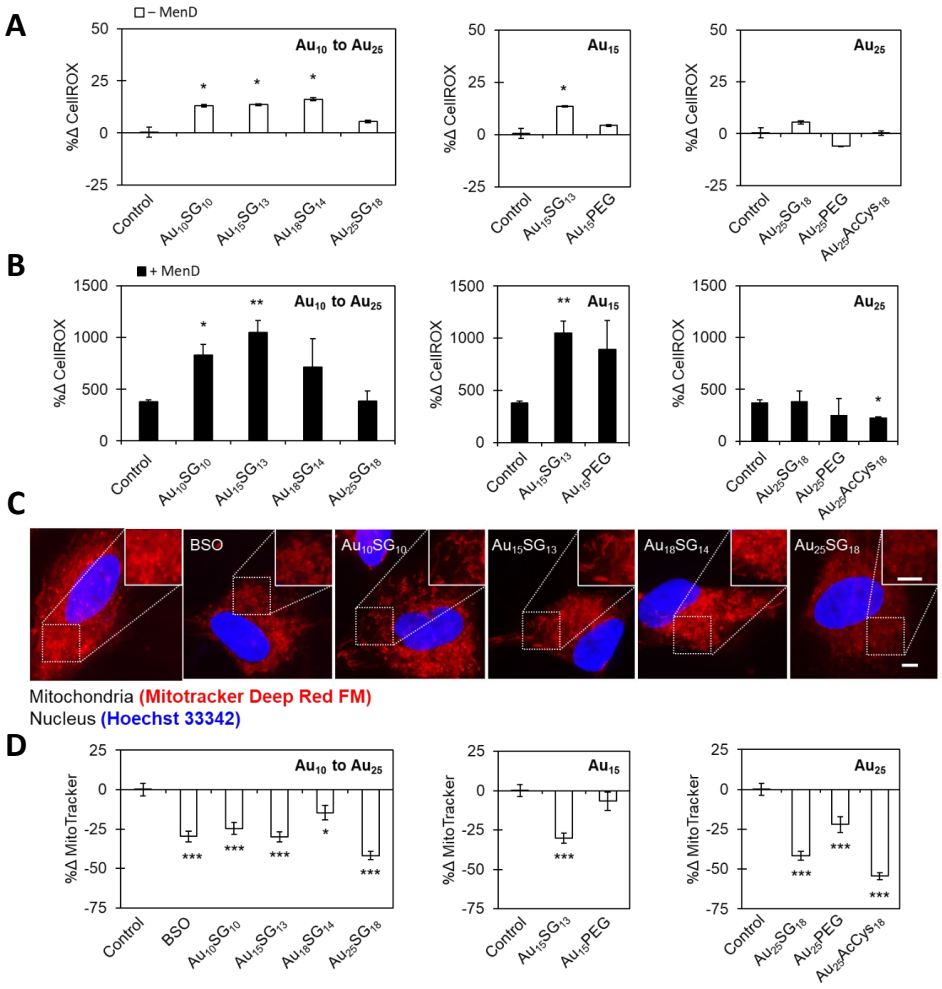

Figure 3. AuNCs impact intracellular redox status and mitochondria. Primary human astrocytes were treated with 10 μM AuNC in the (A) absence or (B) presence of ROS-inducer, menadione (MenD, 25 μM) for 24 hours. (A-B) Percentage change in mean CellROX fluorescence intensity per cell relative to control ± standard error of the mean. (C-D) Percentage change in mean MitoTracker fluorescence intensity relative to control ± standard error of the mean. Cell nuclei were labeled with Hoechst 33342. Scale bars represent 10 μm. Over 400 cells were analyzed in total. A p value of less than 0.05 was identified as statistically significant as follows: *$p<0.05$, **$p<0.01$, ***$p<0.001$.

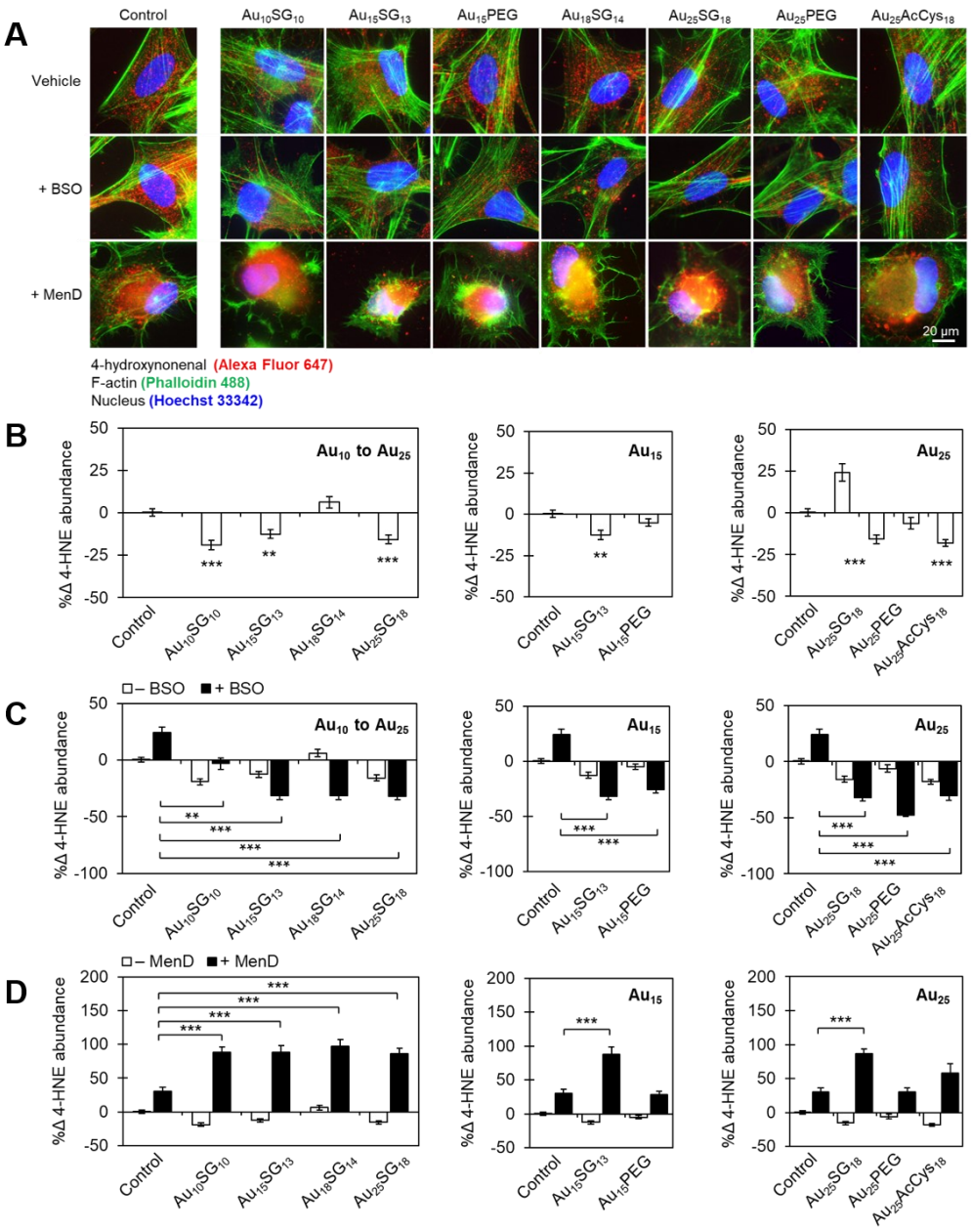

Figure 4. The abundance of peroxidized lipids is differentially altered by AuNCs. (A-D) Human astrocytes were treated with 10 µM AuNC for 24 hours (B) in the absence or (C) presence of 100 µM L-buthionine-sulfoximine (BSO) or (D) 25 µM menadione (MenD). Lipid peroxidation was assessed by antibody labeling of 4-hydroxynonenal (4-HNE). Nuclei were stained with Hoechst 33342. F-actin was labeled using Alexa Fluor phalloidin 488. Mean fluorescence intensities per unit area (μm^2) are normalized to control ± SEM. A minimum of 68 cells in (B), 51 cells in (C), and 14 cells in (D) were analyzed per condition. Over 1600 cells were analyzed in total. A p value of less than 0.05 was identified as statistically significant as follows: *p<0.05, **p<0.01, ***p<0.001.

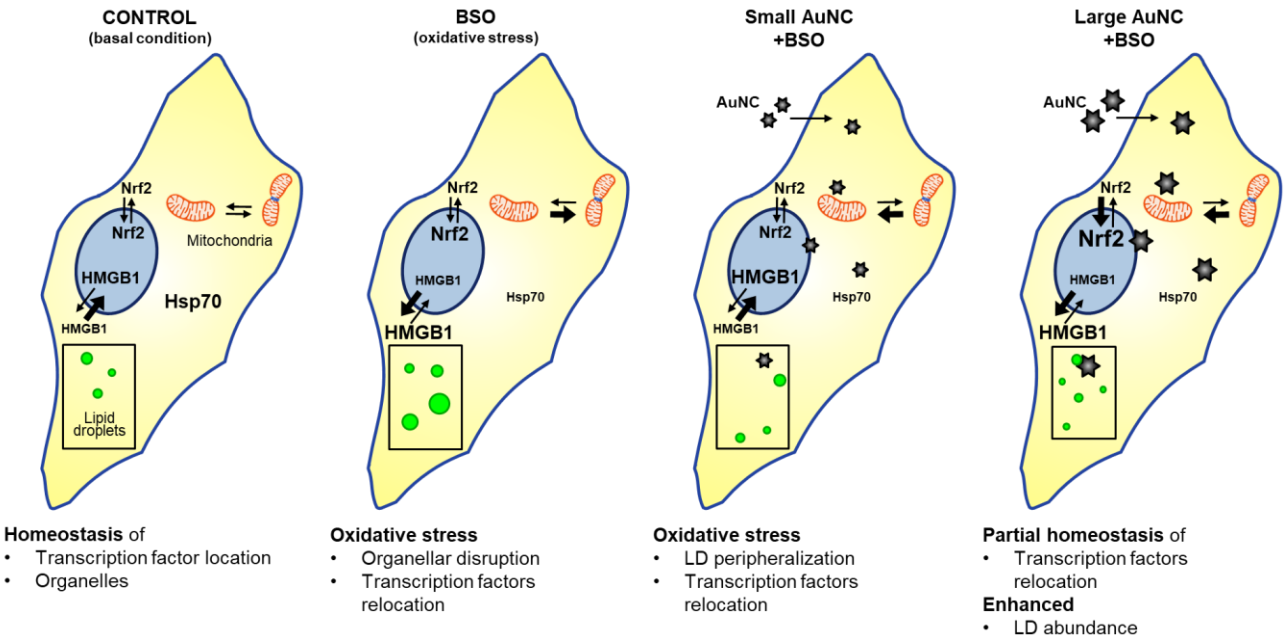

Figure 5. AuNCs alter organellar organization and location of key transcription factors in primary human astrocytes.

3.10. Supplementary Information

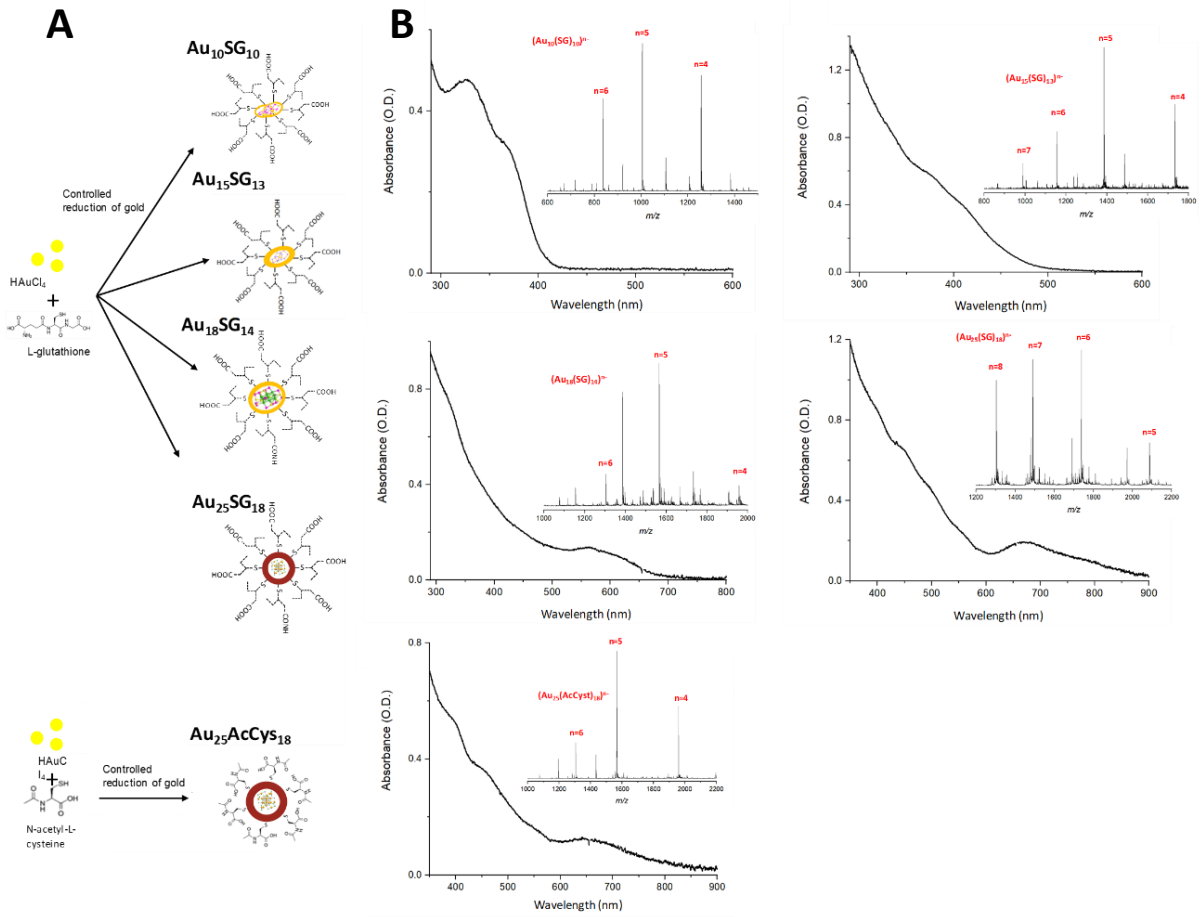

Supplemental Figure 1. Principle of formation of AuNCs using controlled reduction of gold. (A) Principle of formation of Au(SG) and Au(AcCys) involving a controlled reduction of gold. (B) Characterisation of $Au_{10}SG_{10}$, $Au_{15}SG_{13}$, $Au_{18}SG_{14}$ and $Au_{25}SG_{18}$, and $Au_{25}AcCys_{18}$. UV-vis absorption spectra and insets: Electrospray ionization mass spectroscopy of AuNCs.

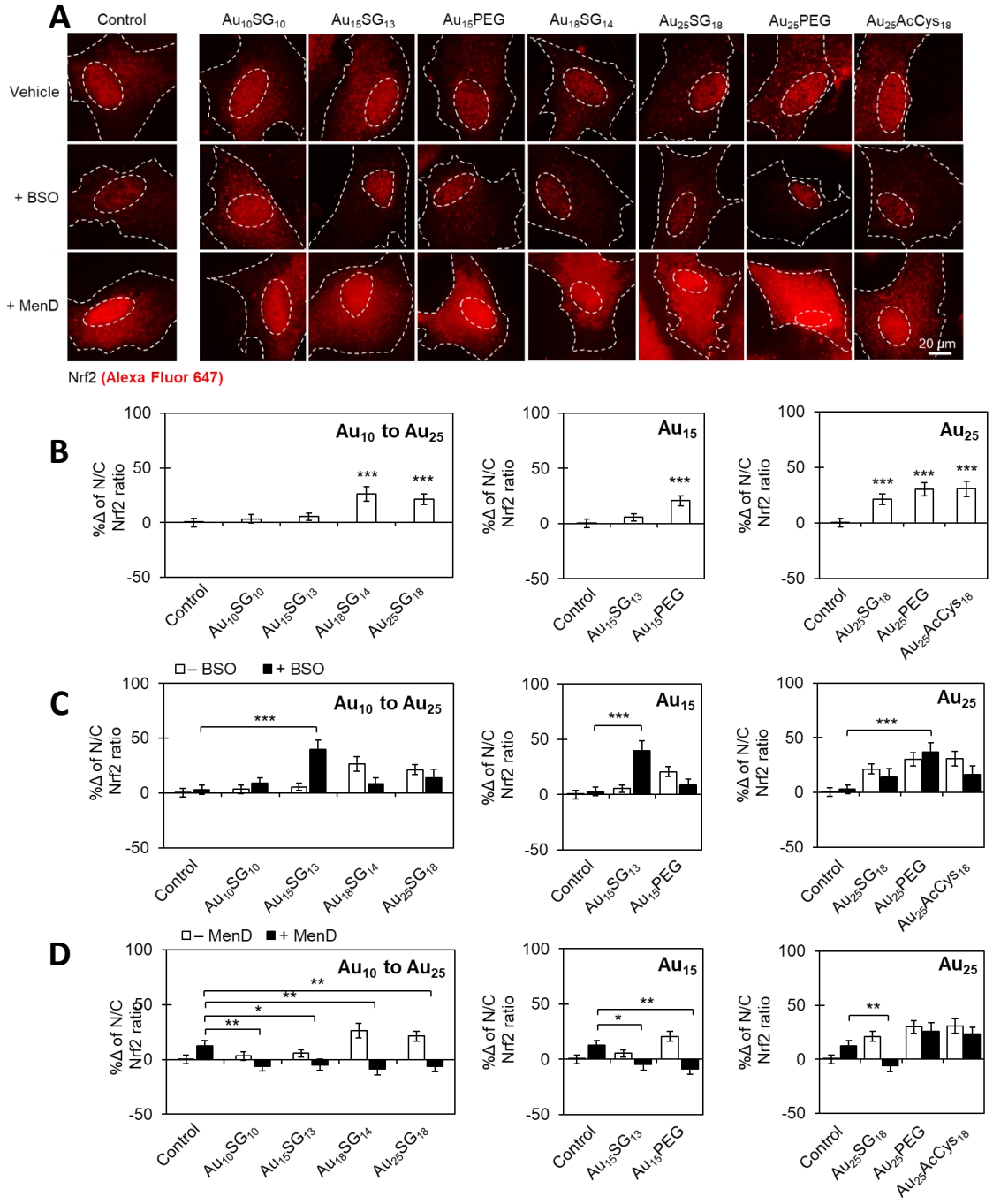

Supplemental figure 2. AuNC induces redistribution of Nrf2. (A) Primary human astrocytes were treated with 10 µM AuNC for 1 hour in the (B) absence or (C) presence of 100 µM L-buthionine-sulfoximine (BSO) or (D) 25 µM menad ione (MenD).Nrf2 cellular distribution was assessed by antibody labelling. Nuclei and cells are outlined. Shown are percentage change of nuclear-to-cytoplasmic (N/C) ratio of mean fluorescence intensities per unit area (μm^2) ± SEM. A minimum of 84 cells in (B), 32 cells in (C), and 54 cells in (D) were analyzed per condition. Over 1800 cells were analyzed in total. A p value of less than 0.05 was identified as statistically significant as follows: *p<0.05, **p<0.01, ***p<0.001.

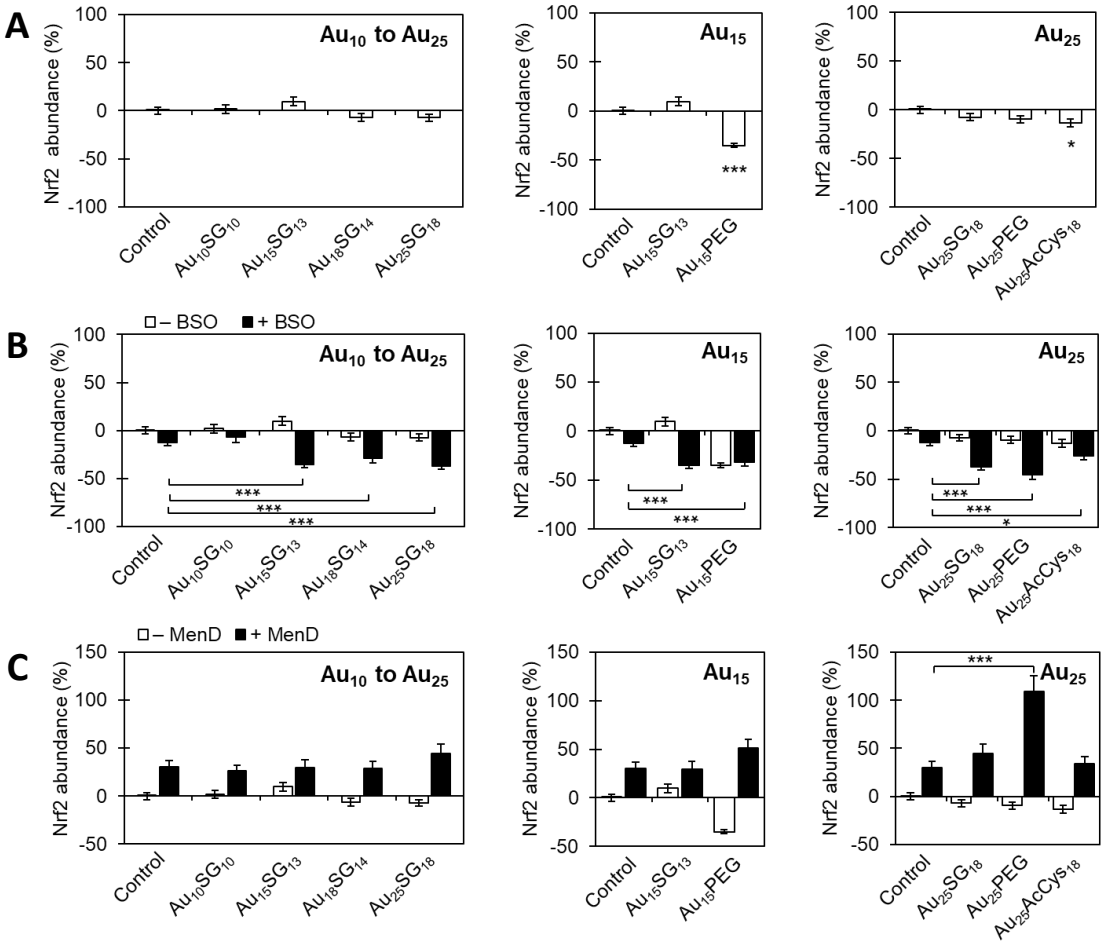

Supplemental Figure 3. AuNCs change total Nrf2 abundance. Human astrocytes were treated with 10 μM AuNC for 1 hour in serum-deprived media in the (A) absence or (B) presence of 100 μM L-buthionine-sulfoximine (BSO) or (C) 25 μM menadione (MenD). BSO or MenD was used as inducer of oxidative stress. Following treatment, cells were fixed and processed for immunocytochemistry. Nuclear factor erythroid 2-related factor 2 (Nrf2) cellular abundance was assessed by antibody labelling. Nuclei and cells are outlined in Supplementary Figure 2. Shown are percentage change of total Nrf2 mean fluorescence intensities per unit area (μm^2) ± SEM. A minimum of 84 cells in (A), 32 cells in (B), and 54 cells in (C) were analyzed per condition. Over 1800 cells were analyzed in total. A p value of less than 0.05 was identified as statistically significant as follows: *$p<0.05$, **$p<0.01$, ***$p<0.001$.

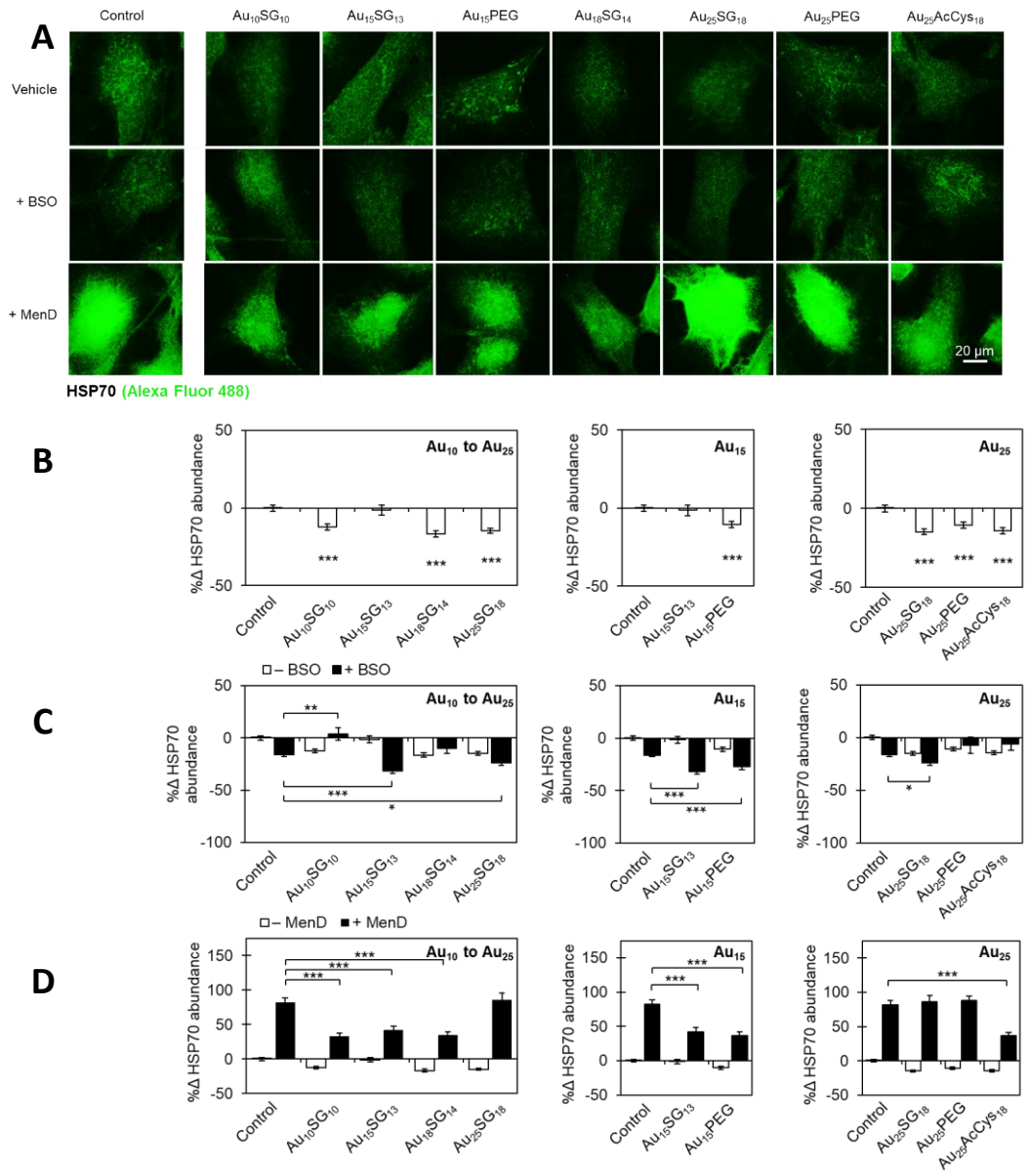

Supplemental Figure 4. AuNCs modulate HSP70 abundance. (A) Primary human astrocytes were treated with 10 µM AuNC for 1 hour in the (B) absence or (C) presence of 100 µM L-buthionine-sulfoximine (BSO) or (D) 25 µM menadione (MenD). BSO or MenD was used as inducer of oxidative stress. Heat shock protein 70 (Hsp70) cellular distribution was assessed by antibody labelling. Shown are percentage change of mean fluorescence intensities per unit area (µm2) ± standard error of the mean. A minimum of 95 cells in (B), 32 cells in (C), and 54 cells in (D) were analyzed per condition. Over 1800 cells were analyzed in total. A p value of less than 0.05 was identified as statistically significant and indicated as: *p<0.05, **p<0.01, ***p<0.001.

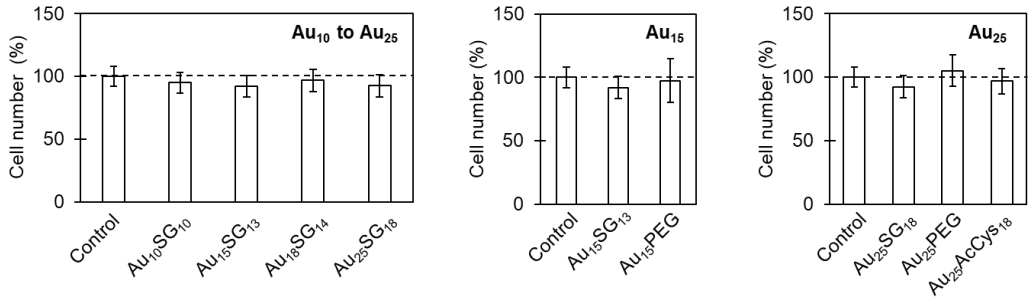

Supplemental Figure 5. AuNCs do not markedly reduce cell number. Primary human astrocytes were treated with 10 μM AuNC for 24 hours. Cell viability was assessed by cell counting, using Hoechst 33342 nuclear stain. Cell number was quantified and normalised to vehicle control. Shown are mean cell number ± SEM from two independent experiments performed in triplicates.

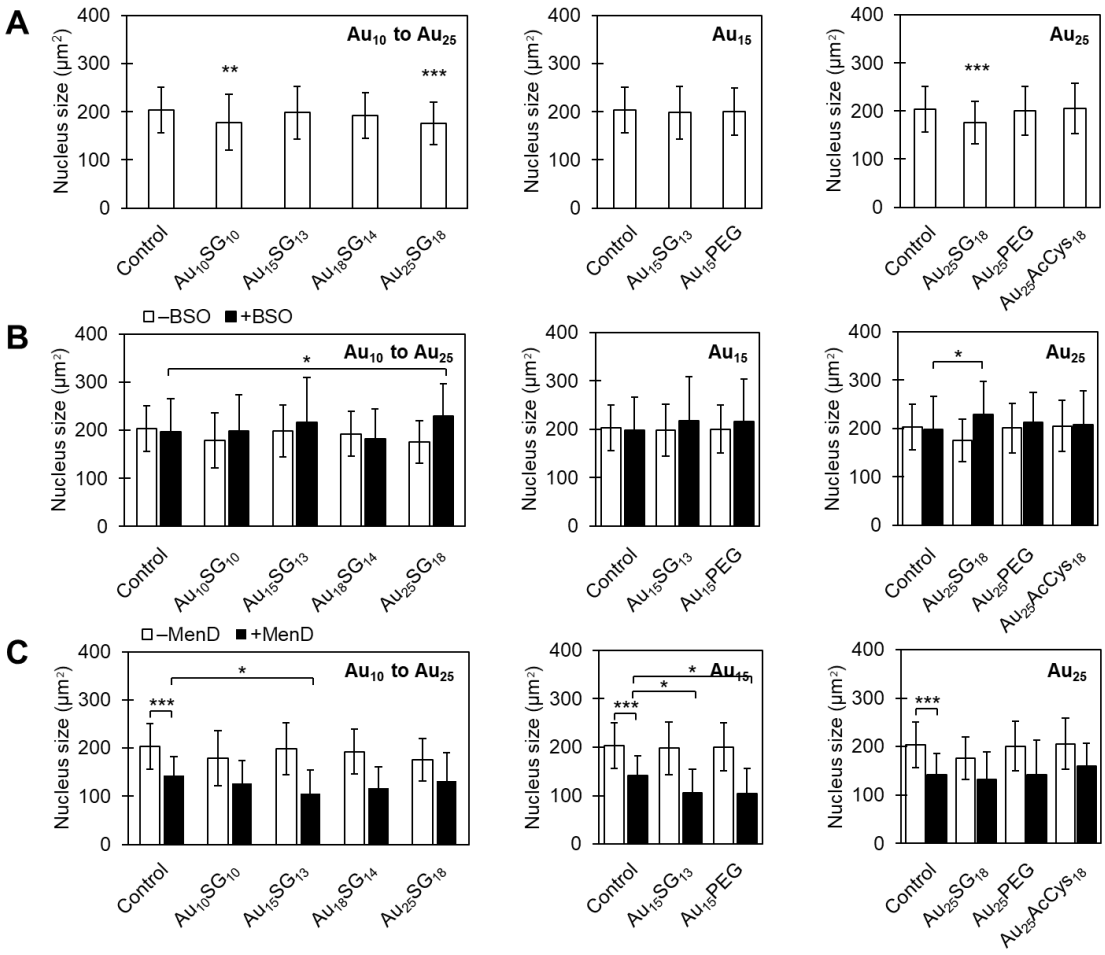

Supplemental figure 6. AuNCs cause minor changes in nuclear area size. Human astrocytes were treated with 10 µM AuNC for 24 hours in serum-deprived media with or without 100 µM L-buthionine-sulfoximine (BSO) or 25 µM menadione (MenD). BSO or MenD was used as inducer of oxidative stress. Following treatment, cells were fixed and processed for immunocytochemistry. Nuclei were stained with Hoechst 33342. Nuclear area (µm2) was quantified using ImageJ, and normalized to vehicle control± SD. A minimum of 65 cells in (A), 40 cells in (B), and 14 cells in (C) were analyzed per condition. Over 1000 cells were analyzed in total. A p value of less than 0.05 was identified as statistically significant and indicated in figures as follows: *p<0.05, **p<0.01, ***p<0.001.

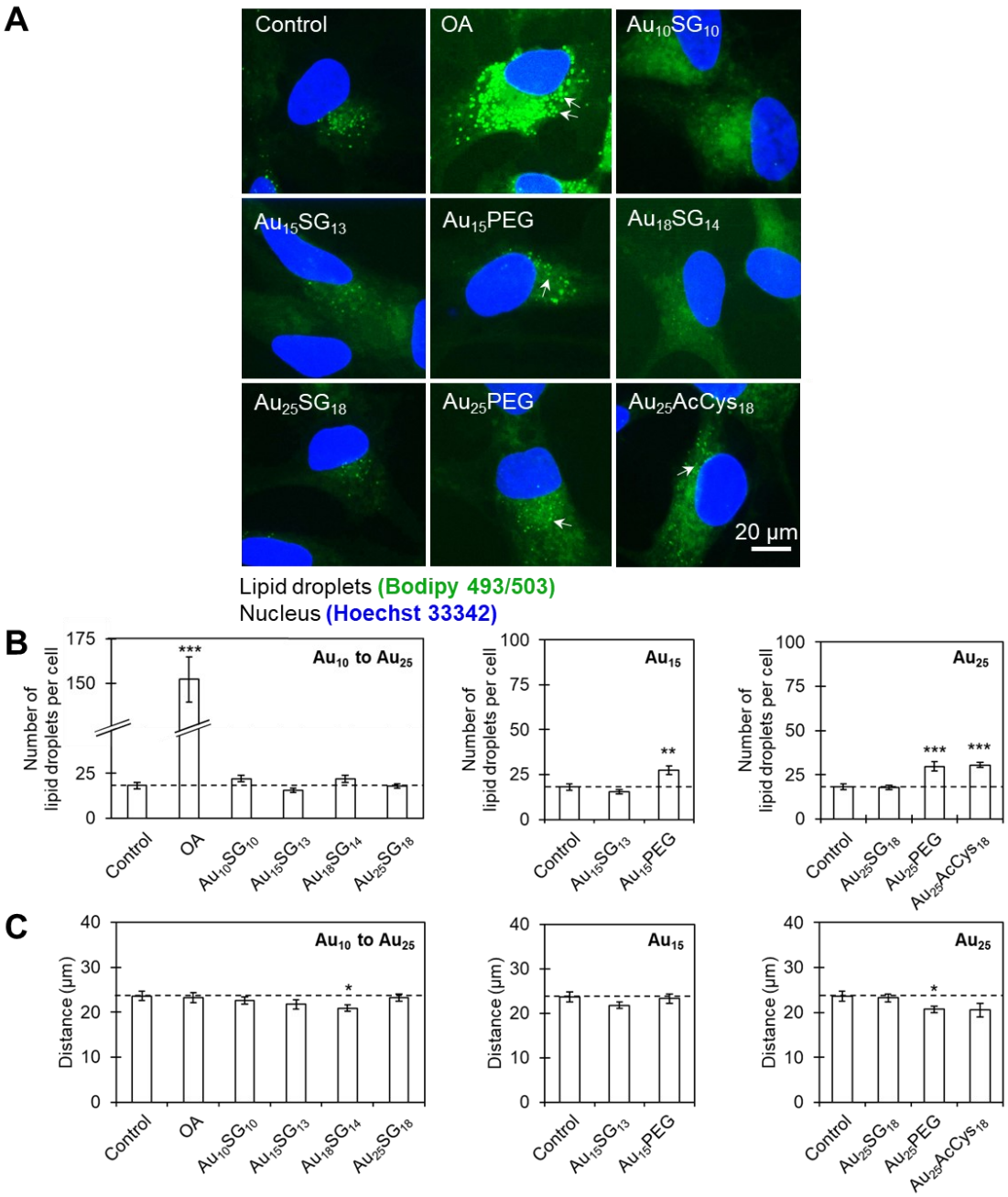

Supplemental figure 7. Reorganization of lipid droplets caused by AuNCs. (A) Human astrocytes were treated with 10 µM AuNC for 24 hours. Oleic acid (300 µM) was used as positive control. Following treatment, neutral lipid droplets were labelled using Bodipy 493/503. Lipid droplet average (B) number, and (C) distance from center of nucleus were quantified and normalized to control ± standard error of the mean. A minimum of 80 cells were analyzed per condition. Over 800 cells were analyzed in total. A p value of less than 0.05 was identified as statistically significant as follows: *p<0.05, **p<0.01, ***p<0.001.

Chapter 4. General discussion

Owing to their atomically precise structures and unique physicochemical properties, AuNCs show potential in diverse biological applications, ranging from imaging, labeling, sensing, and biomedicine. Despite versatile applications, a detailed understanding of biological responses to these nanostructures is required before clinical translation.

The objectives of this thesis were (1) to assess the impact of AuNCs on redox status in cells, (2) to determine the modulatory effects of AuNCs on organellar homeostasis and (3) to elucidate the molecular mechanisms underlying the response of GBM cells and human primary astrocytes to AuNCs of varying sizes and surface ligands. In this chapter, we will discuss the relevance of our findings, highlighting limitations of AuNCs *in vitro* and *in vivo* models and status of AuNCs in biomedical investigations.

		Cell number (% Control±SD)		Mitochondrial metabolic activity (% Control±SD)	
		24h	72h	24h	72h
U251N	10 μM $Au_{15}SG_{13}$	-	73.2±7.9	88.6±2.7*	80.5±6.2
	10 μM $Au_{25}SG_{18}$	-	83.7±10.6	96.3±5.8*	83.7±8.2
Primary astrocytes	10 μM $Au_{15}SG_{13}$	92.0±12.1	-	83.0±27.5*	-
	10 μM $Au_{25}SG_{18}$	92.5±12.6	-	101.7±12.4*	-
HEK293	10 μM $Au_{15}SG_{13}$	-	-	75.5±16.2*	69.8±16.2
	10 μM $Au_{25}SG_{18}$	-	-	89.3±9.0*	86.1±8.1

** unpublished data*

Table 1. Summary of $Au_{15}SG_{13}$ and $Au_{25}SG_{18}$ impact on viability and metabolic activity of human U251N glioblastoma cells, primary astrocytes and HEK293 kidney cells.

Previous studies from our research group reported impact of AuNCs on mouse neural, glial, astrocytic, and 3D organotypic hippocampal cultures (Ji et al., 2019). $Au_{15}SG_{13}$ was found to decrease cell viability and total spine density, although $Au_{25}SG_{18}$ minimally affected viability and total spine density. In **Chapter 2**, we showed that increasing AuNC concentrations reduces GBM number and metabolic activity *in vitro*. In **Chapter 3**, AuNCs minimally affected cell viability at the concentrations tested in human primary astrocytes. As renal clearance is a possible elimination route of nanostructures in living organisms, kidney cells become susceptible to AuNC toxicity. We assessed AuNC toxicity in HEK293 kidney cells and found that Au_{15}NCs moderately affected cell viability, in contrast to Au_{25}NCs (see summary **Table 1**). *In vivo* studies in mice show nanostructures larger than 6 nm are readily eliminated by the reticuloendothelial system. Gold

nanoparticles larger than 6 nm in size have long kidney retention (less than 10%ID after 24 hours) (Xu et al., 2018). In contrast, injected dose of AuNCs with 25 gold atoms decreases by 50%ID, 24 hours following peritoneal injection in healthy mice. As for clusters sizes below Au_{25}, renal clearance efficiency decreases exponentially (Xu et al., 2018). These studies highlight the importance of size in renal excretion of AuNCs and their toxicities. Chronic toxicity tests were performed in cynomolgus monkeys for over 90 days after intravenous injection of gold nanostructures. It was reported that renal clearance and biocompatibility of these gold nanostructures in mice was translated in non-human primates (Yu et al., 2019). Gold nanostructures were excreted mainly by renal clearance rather than bowel elimination. No adverse effects were observed in behavior, weight, heart, spleen, liver, or kidneys after injection of approximately 1000 mg kg^{-1} nanostructures of 2.5 nm core size, suggesting AuNCs are well tolerated by non-human primates (Yu et al., 2019). Regardless, at non-cytotoxic concentrations subtle changes at cellular and molecular levels can be observed, as evidenced by our studies.

Size-dependent effects of AuNCs on redox status was measured, where smaller AuNCs were more effective at increasing oxidative stress in cells. Accessibility of gold atoms, which is dependent on size and surface ligand composition, allows shuttling of electrons and mediation of enzymatic processes (Lee et al., 2012; Malel and Mandler, 2019). In **Chapter 3**, we show that smaller sized clusters display greater water penetration to the core, suggesting smaller sized clusters are more open to engage in biological mechanisms versus the larger sized clusters. These results comply with other studies also reporting that smaller sized gold nanostructures show catalytic activity, which is weaker or lost in larger ones (Kizling et al., 2018). Oxidative stress induction by nanostructures can be predicted by several factors, including the number of surface ligand composition, non-bonded hydrophobic contact preference, interaction potential with water molecules and electrostatic positivity (Wang et al., 2017). Greater water penetration could suggest that smaller sized clusters are more likely to engage in molecular interactions, ultimately resulting in increased oxidative damage.

Collectively, in **Chapters 2** and **3**, we determined the modulatory effects of AuNCs on lysosome, mitochondrion, and lipid droplet homeostasis. In **Chapter 2**, we elucidated cellular mechanisms underlying toxicity of AuNCs, where we found that TFEB-driven lysosomal biogenesis, acidity and activity were important mechanisms for adaptation in GBM. As reported in the literature, exposure to nanoparticles can lead to the activation and translocation of TFEB, as

an effort to boost lysosomal function. Lysosomes are particularly important to cancer biology, as they are essential to eliminate damaged proteins, lipids, organelles and internalized cargo through autophagy or exocytosis (Stern et al., 2012). Lysosomal function in GBM and other tumor cells can enhance tumor survival, whereas the inhibition of lysosomal degradative capacity can successfully lead to cancer cell death and overcome treatment resistance (Cordani and Somoza, 2019; Lahiri et al., 2019).

Several mechanisms can be associated to the difference in cytotoxicity of gold nanoclusters in glioblastoma cells and normal astrocytes: glioblastoma cells **1)** have enhanced cellular uptake (Bjerknes et al., 1987), and **2)** are vulnerable to lysosomal destabilization. Glioblastoma cells exhibit enhanced phagocytic properties compared to normal astrocytes, which is likely utilized to help their survival and proliferation (Bjerknes et al., 1987; Persson and Englund, 2012). However, this pro-survival adaptation increases their vulnerability to the internalization of xenobiotics such as drugs and nanomaterial, compared to normal astrocytes. In **Chapter 2**, we discuss the perturbation of lysosomal parameters, specific aspects of the integrated stress response, and protein aggregation in glioblastoma cells exposed to gold nanoclusters. Results on protein aggregation suggest, given the size and surface composition of nanostructures, a change could be produced in the internal organization of proteins in cells, as reported by Auclair et al., 2020, 2021. Several studies suggest that glioblastoma cells are vulnerable to lysosomal destabilization. Lysosomotrophic pharmacological agents exhibit cytotoxic effects in GBM cells without major effects on normal neural cells (Jacobs et al., 2020). Thus, targeting lysosomes has emerged as promising strategy to kill GBM cells.

Uptake mechanisms of nanostructures depend on nanostructure size, charge, and surface composition. Cellular internalization of nanostructures may occur through the plasma membrane by diffusion, clathrin- or caveolae-mediated endocytosis, phagocytosis, or pinocytosis. Measuring less than 5 nm in size, AuNCs easily diffuse and penetrate through cellular membrane (Lahiri et al., 2019). Weak signals of gold nanoclusters obtained by fluorescence microscopy were inconclusive on AuNC intracellular distribution. Although electron microscopy analyses showed that aggregated clusters were found associated with vesicles, individual gold nanoclusters were difficult to visualize as they are too small (<2 nm). Future studies assessing size-dependency of ultra-small gold nanocluster accumulation in lysosomes are warranted using super-resolution microscopy. Several reports show size-dependent lysosomal accumulation of larger

nanostructures, such as nanoparticles between 10 and 50 nm in diameter. Maximum uptake occurred with 50 nm nanoparticles (Wu et al., 2019). However, a different trend was observed with 20 nm nanoparticles compared to 1,000 nm particles, with maximum uptake occurring with 20 nm nanoparticles (Seydoux et al., 2014). The trend on the lysosomal accumulation of nanostructures of less than 5 nm in diameter, are yet to be determined. Nevertheless, experiments with pharmacological inhibitors of endocytosis pathways reveal that AuNC uptake and transport is partly mediated by clathrin-mediated and F-actin dependent endocytosis, such that AuNCs can ultimately accumulate in lysosomes (Le Guével et al., 2015; Muraca et al., 2020). Such experiments also show that AuNC internalization is mediated, to a lesser degree, by macropinocytosis. To promote receptor mediated endocytosis, AuNC can be functionalized with biomolecules (e.g. receptor ligands or their mimetics) (Le Guével et al., 2015; Muraca et al., 2020).

In **Chapter 3**, we demonstrated that non-cytotoxic concentration of AuNCs can induce short-term functional changes at an organellar level in human primary astrocytes. We observed mitochondria are susceptible to AuNCs, as evidenced by moderate alterations in mitochondrial morphology and fission-fusion dynamics. Subtler changes were detected on lipid droplet number and distribution in response to AuNCs. Interestingly, significant effects in lipid composition were observed upon exposure to AuNC, where AuNCs protected human primary astrocytes from BSO-induced lipid peroxidation. In contrast, astrocytes suffering from severe levels of lipid peroxidation could not be counteracted by AuNC treatments.

Finally, we demonstrated that AuNCs can have a size-dependent impact on the degree of activation of cytoprotective pathways in primary human astrocytes under mild oxidative stress. Au_{25}NC successfully induced the early activation of Nrf2, where the activation of the Nrf2 pathway promotes glutathione synthesis, and activity of antioxidant enzymes (Hayes and Dinkova-Kostova, 2014). Findings in **Chapter 3** show that larger sized Au_{25}NCs, as oppose to clusters with 10 to 18 gold atoms, are consistently protective in conditions of mild oxidative stress.

Herein, spherical AuNCs were produced and assessed in biological systems. A difference in cellular and/or molecular effects could be expected between spherical and linear gold nanoclusters. Nanostructures of similar hydrodynamic sizes and surface potentials, exhibit differential rate of cellular internalization dependent on shape (e.g. sphere, star, rod, triangle) (Li et al., 2015; Xie et al., 2017). Spherical nanostructures demonstrate greater cellular uptake among differently shaped nanostructures (Li et al., 2015), partly owing to the lower energy required for

membrane binding energy during endocytosis. Shape of nanostructures can also influence protein interactions. Rod-shaped (linear) nanostructures have greater surface area than spherical structures for a given volume. The higher surface area of linear nanostructures can enhance protein corona formation (Visalakshan et al., 2020), cytoskeleton disruption, thereby contributing to greater stress involved in intracellular trafficking (Auclair et al., 2021).

As modulators of reactive oxygen species in biological systems, AuNCs show potential as treatment for diseases associated with oxidative stress and neuroinflammation. Although moderate levels of ROS are essential for normal cellular function and signaling, chronic and/or excessive levels of ROS in neuronal and glial cells poses a risk to the progression of neurological diseases. Oxidative stress can lead to progressive neuronal injury and glial reactivity, inflicting genotoxicity, proteotoxicity and lipid peroxidation in the brain. Antioxidant therapy for neuroprotection is a vital strategy for the management of neurodegenerative disorders and brain cancers (Teleanu et al., 2019). Considering the instability of natural antioxidants, modulation of redox status and cytoprotective mechanisms by AuNCs can potentially improve neuroprotection in response to oxidative stress. Future studies are needed to evaluate efficiencies of different routes of administration and assess AuNCs systemic toxicity.

Chapter 5. General conclusions

The results described in this thesis suggest that (1) AuNCs are not inert and have cell-dependent effects, (2) effects of AuNCs are primarily dependent on size, and less on surface ligand, (3) AuNCs can activate cytoprotective responses to redox stress.

In **Chapter 2**, we describe the involvement of lysosomes in the adaptation of human GBM cells to AuNC-induced cytotoxicity. The key finding from this study is that, even below cytotoxic concentrations, AuNCs are effective at causing homeostatic perturbations at the lysosomal and molecular levels in glioblastoma cells.

In **Chapter 3**, we explored the modulatory effects of AuNCs on various organelles and stress responses in human primary astrocytes. The novelty of this study comes from the assessment of the impact of AuNCs of different sizes and surface ligands, in human primary astrocytes under different stress conditions. This is the first study reporting the effects of AuNCs in human untransformed primary astrocytes, and the role of nanocluster core size.

The studies presented in this thesis build a case for AuNCs as modulators of processes contributing to neuroinflammation and neuroprotection. Modulatory processes by AuNC are tightly dependent on the number of the gold atoms and the accessibility to their catalytic surfaces. AuNC present a unique class of nanostructures mimicking enzymatic activity and therefore are named “nanozymes”.

The progress of AuNC research warrants long-term studies *in vitro* and *in vivo* to further define biological responses to AuNCs. We propose that future studies explore the effects of AuNCs in other cell types including those in the tumor microenvironment (e.g., human neurons and microglia). Another set of follow-up studies should be conducted in multicellular models, such as human organoids. Finally, further computational computation analyses merit investigation to reveal direct interactions of key biomolecules as AuNC protein targets, their precise sites of interactions, and the role of these individual sites contributing to AuNC-biomolecule interactions.

References

Ahsan, A., Ramanand, S.G., Whitehead, C., Hiniker, S.M., Rehemtulla, A., Pratt, W.B., Jolly, S., Gouveia, C., Truong, K., Waes, C.V., et al. (2012). Wild-type EGFR Is Stabilized by Direct Interaction with HSP90 in Cancer Cells and Tumors. Neoplasia *14*, 670-IN1.

Ajlan, A., Thomas, P., Albakr, A., Nagpal, S., and Recht, L. (2017). Optimizing bevacizumab dosing in glioblastoma: less is more. J Neurooncol *135*, 99–105.

Andersson, U., Yang, H., and Harris, H. (2018). High-mobility group box 1 protein (HMGB1) operates as an alarmin outside as well as inside cells. Semin. Immunol. *38*, 40–48.

Auclair, J., Peyrot, C., Wilkinson, K.J., and Gagné, F. (2020). Biophysical effects of polystyrene nanoparticles on Elliptio complanata mussels. Environ Sci Pollut Res Int *27*, 25093–25102.

Auclair, J., Peyrot, C., Wilkinson, K.J., and Gagné, F. (2021). The geometry of the toxicity of silver nanoparticles to freshwater mussels. Comparative Biochemistry and Physiology Part C: Toxicology & Pharmacology *239*, 108841.

Awasthi, R., Roseblade, A., Hansbro, P.M., Rathbone, M.J., Dua, K., and Bebawy, M. (2018). Nanoparticles in Cancer Treatment: Opportunities and Obstacles. Curr Drug Targets *19*, 1696–1709.

Ballabio, A. (2016). The awesome lysosome. EMBO Molecular Medicine *8*, 73–76.

Beere, H.M. (2004). `The stress of dying': the role of heat shock proteins in the regulation of apoptosis. Journal of Cell Science *117*, 2641–2651.

Bjerknes, R., Bjerkvig, R., and Laerum, O.D. (1987). Phagocytic capacity of normal and malignant rat glial cells in culture. J Natl Cancer Inst *78*, 279–288.

Borran, A.A., Aghanejad, A., Farajollahi, A., Barar, J., and Omidi, Y. (2018). Gold nanoparticles for radiosensitizing and imaging of cancer cells. Radiation Physics and Chemistry *152*, 137–144.

Bosch, M., Sánchez-Álvarez, M., Fajardo, A., Kapetanovic, R., Steiner, B., Dutra, F., Moreira, L., López, J.A., Campo, R., Marí, M., et al. (2020). Mammalian lipid droplets are innate immune hubs integrating cell metabolism and host defense. Science *370*.

Brandao, M., Simon, T., Critchley, G., and Giamas, G. (2019). Astrocytes, the rising stars of the glioblastoma microenvironment. Glia *67*, 779–790.

Cappello, F., Macario, E.C. de, Marasà, L., Zummo, G., and Macario, A.J.L. (2008). Hsp60 expression, new locations, functions, and perspectives for cancer diagnosis and therapy. Cancer Biology & Therapy *7*, 801–809.

Chithrani, B.D., Ghazani, A.A., and Chan, W.C.W. (2006). Determining the Size and Shape Dependence of Gold Nanoparticle Uptake into Mammalian Cells. Nano Lett. *6*, 662–668.

Chowdhary, S.A., Ryken, T., and Newton, H.B. (2015). Survival outcomes and safety of carmustine wafers in the treatment of high-grade gliomas: a meta-analysis. J Neurooncol *122*, 367–382.

Cohen, M.H., Shen, Y.L., Keegan, P., and Pazdur, R. (2009). FDA Drug Approval Summary: Bevacizumab (Avastin®) as Treatment of Recurrent Glioblastoma Multiforme. The Oncologist *14*, 1131–1138.

Cordani, M., and Somoza, Á. (2019). Targeting autophagy using metallic nanoparticles: a promising strategy for cancer treatment. Cell. Mol. Life Sci. *76*, 1215–1242.

Cruz, A.L.S., Barreto, E. de A., Fazolini, N.P.B., Viola, J.P.B., and Bozza, P.T. (2020). Lipid droplets: platforms with multiple functions in cancer hallmarks. Cell Death & Disease *11*, 1–16.

Deus, C.M., Yambire, K.F., Oliveira, P.J., and Raimundo, N. (2020). Mitochondria–Lysosome Crosstalk: From Physiology to Neurodegeneration. Trends in Molecular Medicine *26*, 71–88.

Dreaden, E.C., Austin, L.A., Mackey, M.A., and El-Sayed, M.A. (2012). Size matters: gold nanoparticles in targeted cancer drug delivery. Ther Deliv *3*, 457–478.

Du, B., Jiang, X., Das, A., Zhou, Q., Yu, M., Jin, R., and Zheng, J. (2017). Glomerular barrier behaves as an atomically precise bandpass filter in a sub-nanometre regime. Nat Nanotechnol *12*, 1096–1102.

Easaw, J.C., Mason, W.P., Perry, J., Laperrière, N., Eisenstat, D.D., Maestro, R.D., Bélanger, K., Fulton, D., and Macdonald, D. (2011). Canadian recommendations for the treatment of recurrent or progressive glioblastoma multiforme. Current Oncology *18*, e126–e136.

Escudero-Francos, M.A., Cepas, V., González-Menéndez, P., Badía-Laíño, R., Díaz-García, M.E., Sainz, R.M., Mayo, J.C., and Hevia, D. (2017). Cellular Uptake and Tissue Biodistribution of Functionalized Gold Nanoparticles and Nanoclusters. Journal of Biomedical Nanotechnology *13*, 167–179.

Fernandes, C., Costa, A., Osório, L., Lago, R.C., Linhares, P., Carvalho, B., and Caeiro, C. (2017). Current Standards of Care in Glioblastoma Therapy. In Glioblastoma, S. De Vleeschouwer, ed. (Brisbane (AU): Codon Publications), p.

Fields, R.D., Araque, A., Johansen-Berg, H., Lim, S.-S., Lynch, G., Nave, K.-A., Nedergaard, M., Perez, R., Sejnowski, T., and Wake, H. (2013). Glial Biology in Learning and Cognition: The Neuroscientist.

Fogel, D.B. (2018). Factors associated with clinical trials that fail and opportunities for improving the likelihood of success: A review. Contemporary Clinical Trials Communications *11*, 156–164.

Friedman, J.R., and Nunnari, J. (2014). Mitochondrial form and function. Nature *505*, 335–343.

Fröhlich, E. (2012). The role of surface charge in cellular uptake and cytotoxicity of medical nanoparticles. Int J Nanomedicine *7*, 5577–5591.

Gao, Q., and Goodman, J.M. (2015). The lipid droplet—a well-connected organelle. Front. Cell Dev. Biol. *3*.

Hainfeld, J.F., Dilmanian, F.A., Slatkin, D.N., and Smilowitz, H.M. (2008). Radiotherapy enhancement with gold nanoparticles. Journal of Pharmacy and Pharmacology *60*, 977–985.

Halcrow, P., Datta, G., Ohm, J.E., Soliman, M.L., Chen, X., and Geiger, J.D. (2019). Role of endolysosomes and pH in the pathogenesis and treatment of glioblastoma. Cancer Reports *2*, e1177.

Hanif, F., Muzaffar, K., Perveen, K., Malhi, S.M., and Simjee, S.U. (2017). Glioblastoma Multiforme: A Review of its Epidemiology and Pathogenesis through Clinical Presentation and Treatment. Asian Pacific Journal of Cancer Prevention *18*, 3–9.

Harder, B.G., Blomquist, M.R., Wang, J., Kim, A.J., Woodworth, G.F., Winkles, J.A., Loftus, J.C., and Tran, N.L. (2018). Developments in Blood-Brain Barrier Penetrance and Drug Repurposing for Improved Treatment of Glioblastoma. Front. Oncol. *8*.

Hayes, J.D., and Dinkova-Kostova, A.T. (2014). The Nrf2 regulatory network provides an interface between redox and intermediary metabolism. Trends in Biochemical Sciences *39*, 199–218.

Henne, M. (2019). And three's a party: lysosomes, lipid droplets, and the ER in lipid trafficking and cell homeostasis. Current Opinion in Cell Biology *59*, 40–49.

Henrik Heiland, D., Ravi, V.M., Behringer, S.P., Frenking, J.H., Wurm, J., Joseph, K., Garrelfs, N.W.C., Strähle, J., Heynckes, S., Grauvogel, J., et al. (2019). Tumor-associated reactive astrocytes aid the evolution of immunosuppressive environment in glioblastoma. Nature Communications *10*, 2541.

Herd, H., Daum, N., Jones, A.T., Huwer, H., Ghandehari, H., and Lehr, C.-M. (2013). Nanoparticle Geometry and Surface Orientation Influence Mode of Cellular Uptake. ACS Nano *7*, 1961–1973.

Hirn, S., Semmler-Behnke, M., Schleh, C., Wenk, A., Lipka, J., Schäffler, M., Takenaka, S., Möller, W., Schmid, G., Simon, U., et al. (2011). Particle size-dependent and surface charge-dependent biodistribution of gold nanoparticles after intravenous administration. European Journal of Pharmaceutics and Biopharmaceutics *77*, 407–416.

Hong, B., Muili, K., Bolyard, C., Russell, L., Lee, T.J., Banasavadi-Siddegowda, Y., Yoo, J.Y., Yan, Y., Ballester, L.Y., Bockhorst, K.H., et al. (2019). Suppression of HMGB1 Released in the Glioblastoma Tumor Microenvironment Reduces Tumoral Edema. Molecular Therapy - Oncolytics *12*, 93–102.

Huang, L.-H., Wang, H.-S., and Kang, L. (2008). Different evolutionary lineages of large and small heat shock proteins in eukaryotes. Cell Research *18*, 1074–1076.

Huang, X., Li, L., Liu, T., Hao, N., Liu, H., Chen, D., and Tang, F. (2011). The Shape Effect of Mesoporous Silica Nanoparticles on Biodistribution, Clearance, and Biocompatibility in Vivo. ACS Nano *5*, 5390–5399.

Hudson, A.L., Parker, N.R., Khong, P., Parkinson, J.F., Dwight, T., Ikin, R.J., Zhu, Y., Chen, J., Wheeler, H.R., and Howell, V.M. (2018). Glioblastoma Recurrence Correlates With Increased APE1 and Polarization Toward an Immuno-Suppressive Microenvironment. Front. Oncol. *8*.

Islam, A., Kagawa, Y., Miyazaki, H., Shil, S.K., Umaru, B.A., Yasumoto, Y., Yamamoto, Y., and Owada, Y. (2019). FABP7 Protects Astrocytes Against ROS Toxicity via Lipid Droplet Formation. Mol Neurobiol *56*, 5763–5779.

Jacobs, K.A., Maghe, C., and Gavard, J. (2020). Lysosomes in glioblastoma: pump up the volume. Cell Cycle *19*, 2094–2104.

Ji, J., Moquin, A., Bertorelle, F., Ky Chang, P., Antoine, R., Luo, J., McKinney, R.A., and Maysinger, D. (2019). Organotypic and primary neural cultures as models to assess effects of different gold nanostructures on glia and neurons. Nanotoxicology *13*, 285–304.

Jin, Y., Jia, C., Huang, S.-W., O'Donnell, M., and Gao, X. (2010). Multifunctional nanoparticles as coupled contrast agents. Nature Communications *1*, 41.

Joh, D.Y., Sun, L., Stangl, M., Zaki, A.A., Murty, S., Santoiemma, P.P., Davis, J.J., Baumann, B.C., Alonso-Basanta, M., Bhang, D., et al. (2013). Selective Targeting of Brain Tumors with Gold Nanoparticle-Induced Radiosensitization. PLOS ONE *8*, e62425.

Kang, X., Chong, H., and Zhu, M. (2018). Au25(SR)18: the captain of the great nanocluster ship. Nanoscale *10*, 10758–10834.

Kansanen, E., Kivelä, A.M., and Levonen, A.-L. (2009). Regulation of Nrf2-dependent gene expression by 15-deoxy-Δ12,14-prostaglandin J2. Free Radical Biology and Medicine *47*, 1310–1317.

Kansanen, E., Kuosmanen, S.M., Leinonen, H., and Levonen, A.-L. (2013). The Keap1-Nrf2 pathway: Mechanisms of activation and dysregulation in cancer. Redox Biology *1*, 45–49.

Kim, S.-J., Kim, J.-S., Park, E.S., Lee, J.-S., Lin, Q., Langley, R.R., Maya, M., He, J., Kim, S.-W., Weihua, Z., et al. (2011). Astrocytes Upregulate Survival Genes in Tumor Cells and Induce Protection from Chemotherapy. Neoplasia *13*, 286–298.

Kizling, M., Dzwonek, M., Więckowska, A., and Bilewicz, R. (2018). Size Does Matter—Mediation of Electron Transfer by Gold Clusters in Bioelectrocatalysis. ChemCatChem *10*, 1988–1992.

Kumthekar, P., Rademaker, A., Ko, C., Dixit, K., Schwartz, M.A., Sonabend, A.M., Sharp, L., Lukas, R.V., Stupp, R., Horbinski, C., et al. (2019). A phase 0 first-in-human study using NU-0129: A gold base spherical nucleic acid (SNA) nanoconjugate targeting BCL2L12 in recurrent glioblastoma patients. JCO *37*, 3012–3012.

Lahiri, V., Hawkins, W.D., and Klionsky, D.J. (2019). Watch what you (self-) eat: Autophagic mechanisms that modulate metabolism. Cell Metab *29*, 803–826.

Lämmer, F., Delbridge, C., Würstle, S., Neff, F., Meyer, B., Schlegel, J., Kessel, K.A., Schmid, T.E., Schilling, D., and Combs, S.E. (2019). Cytosolic Hsp70 as a biomarker to predict clinical outcome in patients with glioblastoma. PLOS ONE *14*, e0221502.

Lange, S.S., and Vasquez, K.M. (2009). HMGB1: The jack-of-all-trades protein is a master DNA repair mechanic. Molecular Carcinogenesis *48*, 571–580.

Lasagna-Reeves, C., Gonzalez-Romero, D., Barria, M.A., Olmedo, I., Clos, A., Sadagopa Ramanujam, V.M., Urayama, A., Vergara, L., Kogan, M.J., and Soto, C. (2010). Bioaccumulation and toxicity of gold nanoparticles after repeated administration in mice. Biochemical and Biophysical Research Communications *393*, 649–655.

Le Guével, X., Perez Perrino, M., Fernández, T.D., Palomares, F., Torres, M.-J., Blanca, M., Rojo, J., and Mayorga, C. (2015). Multivalent Glycosylation of Fluorescent Gold Nanoclusters Promotes Increased Human Dendritic Cell Targeting via Multiple Endocytic Pathways. ACS Appl. Mater. Interfaces *7*, 20945–20956.

Lee, S.Y. (2016). Temozolomide resistance in glioblastoma multiforme. Genes & Diseases *3*, 198–210.

Lee, S., Ringstrand, B.S., Stone, D.A., and Firestone, M.A. (2012). Electrochemical Activity of Glucose Oxidase on a Poly(ionic liquid)–Au Nanoparticle Composite. ACS Appl. Mater. Interfaces *4*, 2311–2317.

Li, X., Spelat, R., Bartolini, A., Cesselli, D., Ius, T., Skrap, M., Caponnetto, F., Manini, I., Yang, Y., and Torre, V. (2020). Mechanisms of malignancy in glioblastoma cells are linked to mitochondrial Ca2+ uniporter upregulation and higher intracellular Ca2+ levels. J Cell Sci *133*.

Li, Y., Kröger, M., and Liu, W.K. (2015). Shape effect in cellular uptake of PEGylated nanoparticles: comparison between sphere, rod, cube and disk. Nanoscale *7*, 16631–16646.

Liu, L.Y., Ji, M.S., Nguyen, N.T., Chow, F.E., Molaie, D.M., Pianka, S.T., Green, R.M., Liau, L.M., Ellingson, B.M., Nghiemphu, P.L., et al. (2019). Patterns of long-term survivorship following bevacizumab treatment for recurrent glioma: a case series. CNS Oncology *8*, CNS35.

Lundqvist, M., Stigler, J., Elia, G., Lynch, I., Cedervall, T., and Dawson, K.A. (2008). Nanoparticle size and surface properties determine the protein corona with possible implications for biological impacts. PNAS *105*, 14265–14270.

Lyon, K.A., and Huang, J.H. (2018). Bevacizumab as an adjuvant therapy for glioblastoma in elderly patients: the facts. Translational Cancer Research *1*, S802-S805–S805.

Malel, E., and Mandler, D. (2019). Direct Electron Transfer between Glucose Oxidase and Gold Nanoparticles; When Size Matters. ChemElectroChem *6*, 147–154.

Martina, J.A., Chen, Y., Gucek, M., and Puertollano, R. (2012). MTORC1 functions as a transcriptional regulator of autophagy by preventing nuclear transport of TFEB. Autophagy *8*, 903–914.

Matias, D., Balça-Silva, J., da Graça, G.C., Wanjiru, C.M., Macharia, L.W., Nascimento, C.P., Roque, N.R., Coelho-Aguiar, J.M., Pereira, C.M., Dos Santos, M.F., et al. (2018). Microglia/Astrocytes–Glioblastoma Crosstalk: Crucial Molecular Mechanisms and Microenvironmental Factors. Front. Cell. Neurosci. *12*.

Medina, D.L., Di Paola, S., Peluso, I., Armani, A., De Stefani, D., Venditti, R., Montefusco, S., Scotto-Rosato, A., Prezioso, C., Forrester, A., et al. (2015). Lysosomal calcium signalling regulates autophagy through calcineurin and TFEB. Nature Cell Biology *17*, 288–299.

Miranda-Gonçalves, V., Cardoso-Carneiro, D., Valbom, I., Cury, F.P., Silva, V.A., Granja, S., Reis, R.M., Baltazar, F., and Martinho, O. (2017). Metabolic alterations underlying Bevacizumab therapy in glioblastoma cells. Oncotarget *8*, 103657–103670.

Mitrakas, A.G., Kalamida, D., Giatromanolaki, A., Pouliliou, S., Tsolou, A., Kyranas, R., and Koukourakis, M.I. (2018). Autophagic flux response and glioblastoma sensitivity to radiation. Cancer Biol Med *15*, 260–274.

Muraca, F., Boselli, L., Castagnola, V., and Dawson, K.A. (2020). Ultrasmall Gold Nanoparticle Cellular Uptake: Influence of Transient Bionano Interactions. ACS Appl. Bio Mater. *3*, 3800–3808.

Nakada, M., Kita, D., Watanabe, T., Hayashi, Y., Teng, L., Pyko, I.V., and Hamada, J.-I. (2011). Aberrant Signaling Pathways in Glioma. Cancers *3*, 3242–3278.

Nakajima, H., Nakajima-Takagi, Y., Tsujita, T., Akiyama, S.-I., Wakasa, T., Mukaigasa, K., Kaneko, H., Tamaru, Y., Yamamoto, M., and Kobayashi, M. (2011). Tissue-Restricted Expression of Nrf2 and Its Target Genes in Zebrafish with Gene-Specific Variations in the Induction Profiles. PLoS One *6*.

Napolitano, G., and Ballabio, A. (2016). TFEB at a glance. J Cell Sci *129*, 2475–2481.

Norouzi, M. (2020). Gold Nanoparticles in Glioma Theranostics. Pharmacological Research *156*, 104753.

Pandey, P., Saleh, A., Nakazawa, A., Kumar, S., Srinivasula, S.M., Kumar, V., Weichselbaum, R., Nalin, C., Alnemri, E.S., Kufe, D., et al. (2000). Negative regulation of cytochrome c-mediated oligomerization of Apaf-1 and activation of procaspase-9 by heat shock protein 90. The EMBO Journal *19*, 4310–4322.

Patel, S., Homaei, A., El-Seedi, H.R., and Akhtar, N. (2018). Cathepsins: Proteases that are vital for survival but can also be fatal. Biomedicine & Pharmacotherapy *105*, 526–532.

Paudel, Y.N., Shaikh, M.F., Chakraborti, A., Kumari, Y., Aledo-Serrano, Á., Aleksovska, K., Alvim, M.K.M., and Othman, I. (2018). HMGB1: A Common Biomarker and Potential Target for TBI, Neuroinflammation, Epilepsy, and Cognitive Dysfunction. Front. Neurosci. *12*.

Perera, R.M., Di Malta, C., and Ballabio, A. (2019). MiT/TFE Family of Transcription Factors, Lysosomes, and Cancer. Annu. Rev. Cancer Biol. *3*, 203–222.

Persson, A., and Englund, E. (2012). Phagocytic properties in tumor astrocytes. Neuropathology *32*, 252–260.

Piao, Y., Liang, J., Holmes, L., Henry, V., Sulman, E., and Groot, J.F. de (2013). Acquired Resistance to Anti-VEGF Therapy in Glioblastoma Is Associated with a Mesenchymal Transition. Clin Cancer Res *19*, 4392–4403.

Rahman, R., Hempfling, K., Norden, A.D., Reardon, D.A., Nayak, L., Rinne, M.L., Beroukhim, R., Doherty, L., Ruland, S., Rai, A., et al. (2014). Retrospective study of carmustine or lomustine with bevacizumab in recurrent glioblastoma patients who have failed prior bevacizumab. Neuro Oncol *16*, 1523–1529.

Rajaratnam, V., Islam, M.M., Yang, M., Slaby, R., Ramirez, H.M., and Mirza, S.P. (2020). Glioblastoma: Pathogenesis and Current Status of Chemotherapy and Other Novel Treatments. Cancers *12*, 937.

Roczniak-Ferguson, A., Petit, C.S., Froehlich, F., Qian, S., Ky, J., Angarola, B., Walther, T.C., and Ferguson, S.M. (2012). The Transcription Factor TFEB Links mTORC1 Signaling to Transcriptional Control of Lysosome Homeostasis. Sci. Signal. *5*, ra42–ra42.

Rosciszewski, G., Cadena, V., Auzmendi, J., Cieri, M.B., Lukin, J., Rossi, A.R., Murta, V., Villarreal, A., Reinés, A., Gomes, F.C.A., et al. (2019). Detrimental Effects of HMGB-1 Require Microglial-Astroglial Interaction: Implications for the Status Epilepticus -Induced Neuroinflammation. Front. Cell. Neurosci. *13*.

Sato, S., Fujita, N., and Tsuruo, T. (2000). Modulation of Akt kinase activity by binding to Hsp90. PNAS *97*, 10832–10837.

Savjani, K.T., Gajjar, A.K., and Savjani, J.K. (2012). Drug Solubility: Importance and Enhancement Techniques (Hindawi).

Schiffer, D., Annovazzi, L., Casalone, C., Corona, C., and Mellai, M. (2019). Glioblastoma: Microenvironment and Niche Concept. Cancers *11*, 5.

Schulte, T.W., Blagosklonny, M.V., Ingui, C., and Neckers, L. (1995). Disruption of the Raf-1-Hsp90 Molecular Complex Results in Destabilization of Raf-1 and Loss of Raf-1-Ras Association. J. Biol. Chem. *270*, 24585–24588.

Seidu, R.A., Wu, M., Su, Z., and Xu, H. (2017). Paradoxical role of high mobility group box 1 in glioma: a suppressor or a promoter? Oncology Reviews *11*.

Seydoux, E., Rothen-Rutishauser, B., Nita, I.M., Balog, S., Gazdhar, A., Stumbles, P.A., Petri-Fink, A., Blank, F., and von Garnier, C. (2014). Size-dependent accumulation of particles in lysosomes modulates dendritic cell function through impaired antigen degradation. Int J Nanomedicine *9*, 3885–3902.

Shi, J., Kantoff, P.W., Wooster, R., and Farokhzad, O.C. (2017). Cancer nanomedicine: progress, challenges and opportunities. Nature Reviews Cancer *17*, 20–37.

Sofroniew, M.V., and Vinters, H.V. (2010). Astrocytes: biology and pathology. Acta Neuropathol *119*, 7–35.

Sohaebuddin, S.K., Thevenot, P.T., Baker, D., Eaton, J.W., and Tang, L. (2010). Nanomaterial cytotoxicity is composition, size, and cell type dependent. Particle and Fibre Toxicology *7*, 22.

Stern, S.T., Adiseshaiah, P.P., and Crist, R.M. (2012). Autophagy and lysosomal dysfunction as emerging mechanisms of nanomaterial toxicity. Particle and Fibre Toxicology *9*, 20.

Strickland, M., and Stoll, E.A. (2017). Metabolic Reprogramming in Glioma. Front. Cell Dev. Biol. *5*.

Taïb, B., Aboussalah, A.M., Moniruzzaman, M., Chen, S., Haughey, N.J., Kim, S.F., and Ahima, R.S. (2019). Lipid accumulation and oxidation in glioblastoma multiforme. Scientific Reports *9*, 19593.

Teleanu, R.I., Chircov, C., Grumezescu, A.M., Volceanov, A., and Teleanu, D.M. (2019). Antioxidant Therapies for Neuroprotection—A Review. Journal of Clinical Medicine *8*, 1659.

Thiruppathi, R., Mishra, S., Ganapathy, M., Padmanabhan, P., and Gulyás, B. (2017). Nanoparticle Functionalization and Its Potentials for Molecular Imaging. Advanced Science *4*, 1600279.

Tietjen, G.T., and Saltzman, W.M. (2015). Nanomedicine gets personal. Science Translational Medicine *7*, 314fs47-314fs47.

Vankayala, R., Kuo, C.-L., Nuthalapati, K., Chiang, C.-S., and Hwang, K.C. (2015). Cancer Therapy: Nucleus-Targeting Gold Nanoclusters for Simultaneous In Vivo Fluorescence Imaging, Gene Delivery, and NIR-Light Activated Photodynamic Therapy (Adv. Funct. Mater. 37/2015). Advanced Functional Materials *25*, 5933–5933.

Vidyasagar, A., Wilson, N.A., and Djamali, A. (2012). Heat shock protein 27 (HSP27): biomarker of disease and therapeutic target. Fibrogenesis & Tissue Repair *5*, 7.

Visalakshan, R.M., García, L.E.G., Benzigar, M.R., Ghazaryan, A., Simon, J., Mierczynska-Vasilev, A., Michl, T.D., Vinu, A., Mailänder, V., Morsbach, S., et al. (2020). The Influence of Nanoparticle Shape on Protein Corona Formation. Small *16*, 2000285.

Wang, W., Sedykh, A., Sun, H., Zhao, L., Russo, D.P., Zhou, H., Yan, B., and Zhu, H. (2017). Predicting Nano–Bio Interactions by Integrating Nanoparticle Libraries and Quantitative Nanostructure Activity Relationship Modeling. ACS Nano *11*, 12641–12649.

Westermann, B. (2010). Mitochondrial fusion and fission in cell life and death. Nature Reviews Molecular Cell Biology *11*, 872–884.

Wick, W., Platten, M., and Weller, M. (2009). New (alternative) temozolomide regimens for the treatment of glioma. Neuro Oncol *11*, 69–79.

Wu, M., Guo, H., Liu, L., Liu, Y., and Xie, L. (2019). Size-dependent cellular uptake and localization profiles of silver nanoparticles. Int J Nanomedicine *14*, 4247–4259.

Wu, X., Geng, F., Cheng, X., Guo, Q., Zhong, Y., Cloughesy, T.F., Yong, W.H., Chakravarti, A., and Guo, D. (2020). Lipid Droplets Maintain Energy Homeostasis and Glioblastoma Growth via Autophagic Release of Stored Fatty Acids. IScience *23*.

Xie, X., Liao, J., Shao, X., Li, Q., and Lin, Y. (2017). The Effect of shape on Cellular Uptake of Gold Nanoparticles in the forms of Stars, Rods, and Triangles. Scientific Reports *7*, 3827.

Xu, H., and Ren, D. (2015). Lysosomal Physiology. Annu. Rev. Physiol. *77*, 57–80.

Xu, J., Yu, M., Peng, C., Carter, P., Tian, J., Ning, X., Zhou, Q., Tu, Q., Zhang, G., Dao, A., et al. (2018). Dose Dependencies and Biocompatibility of Renal Clearable Gold Nanoparticles: From Mice to Non-human Primates. Angewandte Chemie International Edition *57*, 266–271.

Yang, L., Kuang, H., Zhang, W., Aguilar, Z.P., Wei, H., and Xu, H. (2017). Comparisons of the biodistribution and toxicological examinations after repeated intravenous administration of silver and gold nanoparticles in mice. Sci Rep *7*.

Yu, M., Xu, J., and Zheng, J. (2019). Renal Clearable Luminescent Gold Nanoparticles: From the Bench to the Clinic. Angew Chem Int Ed Engl *58*, 4112–4128.

Zhang, S., Gao, H., and Bao, G. (2015). Physical Principles of Nanoparticle Cellular Endocytosis. ACS Nano *9*, 8655–8671.

Zhang, Y., Li, S., Liu, H., Long, W., and Zhang, X.-D. (2020). Enzyme-Like Properties of Gold Clusters for Biomedical Application. Front. Chem. *8*.

Zhao, B., Dierichs, L., Gu, J.-N., Trajkovic-Arsic, M., Axel Hilger, R., Savvatakis, K., Vega-Rubin-de-Celis, S., Liffers, S.-T., Peña-Llopis, S., Behrens, D., et al. (2020). TFEB-mediated lysosomal biogenesis and lysosomal drug sequestration confer resistance to MEK inhibition in pancreatic cancer. Cell Death Discovery *6*, 1–13.

Zhitomirsky, B., and Assaraf, Y.G. (2017). Lysosomal accumulation of anticancer drugs triggers lysosomal exocytosis. Oncotarget *8*, 45117–45132.

Zhu, J., Wang, H., Fan, Y., Lin, Y., Zhang, L., Ji, X., and Zhou, M. (2014). Targeting the NF-E2-related factor 2 pathway: A novel strategy for glioblastoma (Review). Oncology Reports *32*, 443–450.

Zolkiewski, M., Zhang, T., and Nagy, M. (2012). Aggregate reactivation mediated by the Hsp100 chaperones. Archives of Biochemistry and Biophysics *520*, 1–6.

Appendix

The Company of Biologists Ltd. - License Terms and Conditions

This is a License Agreement between McGill University ("You") and The Company of Biologists Ltd. ("Publisher") provided by Copyright Clearance Center ("CCC"). The license consists of your order details, the terms and conditions provided by The Company of Biologists Ltd., and the CCC terms and conditions.

All payments must be made in full to CCC.

Order Date	28-Oct-2020	**Type of Use**	Republish in a thesis/dissertation
Order license ID	1073518-1		
ISSN	1477-9137	**Publisher**	COMPANY OF BIOLOGISTS LTD.
		Portion	Chart/graph/table/figure

LICENSED CONTENT

Publication Title	Journal of cell science	**Country**	United Kingdom of Great Britain and Northern Ireland
Author/Editor	Company of Biologists.		
Date	01/01/1966	**Rightsholder**	The Company of Biologists Ltd.
Language	English	**Publication Type**	e-Journal
		URL	http://jcs.biologists.org/

REQUEST DETAILS

Portion Type	Chart/graph/table/figure	**Distribution**	Worldwide
Number of charts / graphs / tables / figures requested	1	**Translation**	Original language of publication
		Copies for the disabled?	No
Format (select all that apply)	Electronic	**Minor editing privileges?**	Yes
		Incidental promotional use?	No
Who will republish the content?	Academic institution		
		Currency	CAD
Duration of Use	Life of current and all future editions		
Lifetime Unit Quantity	Up to 499		
Rights Requested	Main product		

NEW WORK DETAILS

Title	Gold nanocluster modulation of organelles and cellular stress responses in malignant and non-malignant human astrocytes	**Institution name**	McGill University
		Expected presentation date	2020-11-01
Instructor name	Dusica Maysinger		

ADDITIONAL DETAILS

Order reference number	N/A	**The requesting person / organization to appear on the license**	McGill University

REUSE CONTENT DETAILS

Title, description or numeric reference of the portion(s)	Figure 2. Diversity of LD functions.	**Title of the article/chapter the portion is from**	Lipid droplet–membrane contact sites – from protein binding to function
Editor of portion(s)	N/A	**Author of portion(s)**	Company of Biologists.
Volume of serial or monograph	vol. 132 no. 12, jcs230169	**Issue, if republishing an article from a serial**	N/A
Page or page range of portion	4	**Publication date of portion**	2019-06-17

PUBLISHER TERMS AND CONDITIONS

The acknowledgement should state "Reproduced / adapted with permission" and give the source journal name. The acknowledgement should either provide full citation details or refer to the relevant citation in the article reference list. The full citation details should include authors, journal, year, volume, issue and page citation. Where appearing online or in other electronic media, a link should be provided to the original article (e.g. via DOI): Development: dev.biologists.org Disease Models & Mechanisms: dmm.biologists.org Journal of Cell Science: jcs.biologists.org The Journal of Experimental Biology: jeb.biologists.org

CCC Republication Terms and Conditions

1. Description of Service; Defined Terms. This Republication License enables the User to obtain licenses for republication of one or more copyrighted works as described in detail on the relevant Order Confirmation (the "Work(s)"). Copyright Clearance Center, Inc. ("CCC") grants licenses through the Service on behalf of the rightsholder identified on the Order Confirmation (the "Rightsholder"). "Republication", as used herein, generally means the inclusion of a Work, in whole or in part, in a new work or works, also as described on the Order Confirmation. "User", as used herein, means the person or entity making such republication.

2. The terms set forth in the relevant Order Confirmation, and any terms set by the Rightsholder with respect to a particular Work, govern the terms of use of Works in connection with the Service. By using the Service, the person transacting for a republication license on behalf of the User represents and warrants that he/she/it (a) has been duly authorized by the User to accept, and hereby does accept, all such terms and conditions on behalf of User, and (b) shall inform User of all such terms and conditions. In the event such person is a "freelancer" or other third party independent of User and CCC, such party shall be deemed jointly a "User" for purposes of these terms and conditions. In any event, User shall be deemed to have accepted and agreed to all such terms and conditions if User republishes the Work in any fashion.

3. Scope of License; Limitations and Obligations.

    3.1. All Works and all rights therein, including copyright rights, remain the sole and exclusive property of the Rightsholder. The license created by the exchange of an Order Confirmation (and/or any invoice) and payment by User of the full amount set forth on that document includes only those rights expressly set forth in the Order Confirmation and in these terms and conditions, and conveys no other rights in the Work(s) to User. All rights not expressly granted are hereby reserved.

    3.2. General Payment Terms: You may pay by credit card or through an account with us payable at the end of the month. If you and we agree that you may establish a standing account with CCC, then the following

terms apply: Remit Payment to: Copyright Clearance Center, 29118 Network Place, Chicago, IL 60673-1291. Payments Due: Invoices are payable upon their delivery to you (or upon our notice to you that they are available to you for downloading). After 30 days, outstanding amounts will be subject to a service charge of 1-1/2% per month or, if less, the maximum rate allowed by applicable law. Unless otherwise specifically set forth in the Order Confirmation or in a separate written agreement signed by CCC, invoices are due and payable on "net 30" terms. While User may exercise the rights licensed immediately upon issuance of the Order Confirmation, the license is automatically revoked and is null and void, as if it had never been issued, if complete payment for the license is not received on a timely basis either from User directly or through a payment agent, such as a credit card company.

3.3. Unless otherwise provided in the Order Confirmation, any grant of rights to User (i) is "one-time" (including the editions and product family specified in the license), (ii) is non-exclusive and non-transferable and (iii) is subject to any and all limitations and restrictions (such as, but not limited to, limitations on duration of use or circulation) included in the Order Confirmation or invoice and/or in these terms and conditions. Upon completion of the licensed use, User shall either secure a new permission for further use of the Work(s) or immediately cease any new use of the Work(s) and shall render inaccessible (such as by deleting or by removing or severing links or other locators) any further copies of the Work (except for copies printed on paper in accordance with this license and still in User's stock at the end of such period).

3.4. In the event that the material for which a republication license is sought includes third party materials (such as photographs, illustrations, graphs, inserts and similar materials) which are identified in such material as having been used by permission, User is responsible for identifying, and seeking separate licenses (under this Service or otherwise) for, any of such third party materials; without a separate license, such third party materials may not be used.

3.5. Use of proper copyright notice for a Work is required as a condition of any license granted under the Service. Unless otherwise provided in the Order Confirmation, a proper copyright notice will read substantially as follows: "Republished with permission of [Rightsholder's name], from [Work's title, author, volume, edition number and year of copyright]; permission conveyed through Copyright Clearance Center, Inc. " Such notice must be provided in a reasonably legible font size and must be placed either immediately adjacent to the Work as used (for example, as part of a by-line or footnote but not as a separate electronic link) or in the place where substantially all other credits or notices for the new work containing the republished Work are located. Failure to include the required notice results in loss to the Rightsholder and CCC, and the User shall be liable to pay liquidated damages for each such failure equal to twice the use fee specified in the Order Confirmation, in addition to the use fee itself and any other fees and charges specified.

3.6. User may only make alterations to the Work if and as expressly set forth in the Order Confirmation. No Work may be used in any way that is defamatory, violates the rights of third parties (including such third parties' rights of copyright, privacy, publicity, or other tangible or intangible property), or is otherwise illegal, sexually explicit or obscene. In addition, User may not conjoin a Work with any other material that may result in damage to the reputation of the Rightsholder. User agrees to inform CCC if it becomes aware of any infringement of any rights in a Work and to cooperate with any reasonable request of CCC or the Rightsholder in connection therewith.

4. Indemnity. User hereby indemnifies and agrees to defend the Rightsholder and CCC, and their respective employees and directors, against all claims, liability, damages, costs and expenses, including legal fees and expenses, arising out of any use of a Work beyond the scope of the rights granted herein, or any use of a Work which has been altered in any unauthorized way by User, including claims of defamation or infringement of rights of copyright, publicity, privacy or other tangible or intangible property.

5. Limitation of Liability. UNDER NO CIRCUMSTANCES WILL CCC OR THE RIGHTSHOLDER BE LIABLE FOR ANY DIRECT, INDIRECT, CONSEQUENTIAL OR INCIDENTAL DAMAGES (INCLUDING WITHOUT LIMITATION DAMAGES FOR LOSS OF BUSINESS PROFITS OR INFORMATION, OR FOR BUSINESS INTERRUPTION) ARISING OUT OF THE USE OR INABILITY TO USE A WORK, EVEN IF ONE OF THEM HAS BEEN ADVISED OF THE POSSIBILITY OF SUCH DAMAGES. In any event, the total liability of the Rightsholder and CCC (including their respective employees and directors) shall not exceed

the total amount actually paid by User for this license. User assumes full liability for the actions and omissions of its principals, employees, agents, affiliates, successors and assigns.

6. Limited Warranties. THE WORK(S) AND RIGHT(S) ARE PROVIDED "AS IS". CCC HAS THE RIGHT TO GRANT TO USER THE RIGHTS GRANTED IN THE ORDER CONFIRMATION DOCUMENT. CCC AND THE RIGHTSHOLDER DISCLAIM ALL OTHER WARRANTIES RELATING TO THE WORK(S) AND RIGHT(S), EITHER EXPRESS OR IMPLIED, INCLUDING WITHOUT LIMITATION IMPLIED WARRANTIES OF MERCHANTABILITY OR FITNESS FOR A PARTICULAR PURPOSE. ADDITIONAL RIGHTS MAY BE REQUIRED TO USE ILLUSTRATIONS, GRAPHS, PHOTOGRAPHS, ABSTRACTS, INSERTS OR OTHER PORTIONS OF THE WORK (AS OPPOSED TO THE ENTIRE WORK) IN A MANNER CONTEMPLATED BY USER; USER UNDERSTANDS AND AGREES THAT NEITHER CCC NOR THE RIGHTSHOLDER MAY HAVE SUCH ADDITIONAL RIGHTS TO GRANT.

7. Effect of Breach. Any failure by User to pay any amount when due, or any use by User of a Work beyond the scope of the license set forth in the Order Confirmation and/or these terms and conditions, shall be a material breach of the license created by the Order Confirmation and these terms and conditions. Any breach not cured within 30 days of written notice thereof shall result in immediate termination of such license without further notice. Any unauthorized (but licensable) use of a Work that is terminated immediately upon notice thereof may be liquidated by payment of the Rightsholder's ordinary license price therefor; any unauthorized (and unlicensable) use that is not terminated immediately for any reason (including, for example, because materials containing the Work cannot reasonably be recalled) will be subject to all remedies available at law or in equity, but in no event to a payment of less than three times the Rightsholder's ordinary license price for the most closely analogous licensable use plus Rightsholder's and/or CCC's costs and expenses incurred in collecting such payment.

8. Miscellaneous.

    8.1. User acknowledges that CCC may, from time to time, make changes or additions to the Service or to these terms and conditions, and CCC reserves the right to send notice to the User by electronic mail or otherwise for the purposes of notifying User of such changes or additions; provided that any such changes or additions shall not apply to permissions already secured and paid for.

    8.2. Use of User-related information collected through the Service is governed by CCC's privacy policy, available online here:https://marketplace.copyright.com/rs-ui-web/mp/privacy-policy

    8.3. The licensing transaction described in the Order Confirmation is personal to User. Therefore, User may not assign or transfer to any other person (whether a natural person or an organization of any kind) the license created by the Order Confirmation and these terms and conditions or any rights granted hereunder; provided, however, that User may assign such license in its entirety on written notice to CCC in the event of a transfer of all or substantially all of User's rights in the new material which includes the Work(s) licensed under this Service.

    8.4. No amendment or waiver of any terms is binding unless set forth in writing and signed by the parties. The Rightsholder and CCC hereby object to any terms contained in any writing prepared by the User or its principals, employees, agents or affiliates and purporting to govern or otherwise relate to the licensing transaction described in the Order Confirmation, which terms are in any way inconsistent with any terms set forth in the Order Confirmation and/or in these terms and conditions or CCC's standard operating procedures, whether such writing is prepared prior to, simultaneously with or subsequent to the Order Confirmation, and whether such writing appears on a copy of the Order Confirmation or in a separate instrument.

    8.5. The licensing transaction described in the Order Confirmation document shall be governed by and construed under the law of the State of New York, USA, without regard to the principles thereof of conflicts of law. Any case, controversy, suit, action, or proceeding arising out of, in connection with, or related to such licensing transaction shall be brought, at CCC's sole discretion, in any federal or state court located in the County of New York, State of New York, USA, or in any federal or state court whose geographical jurisdiction covers the location of the Rightsholder set forth in the Order Confirmation. The parties expressly submit to the personal jurisdiction and venue of each such federal or state court.If you have any